Astronomy & Astrophysics manuscript no. aa37216-19
February 1, 2022
©ESO 2022

arXiv:2003.12155v1 [astro-ph.SR] 26 Mar 2020

Discovery of new members of the nearby young stellar association in Cepheus ⋆,⋆⋆

A. Klutsch[1,2,4], A. Frasca[2], P. Guillout[3], D. Montes[4], F.-X. Pineau[3], N. Grosso[5] and B. Stelzer[1,6]

[1] Institut für Astronomie und Astrophysik, Eberhard Karls Universität, Sand 1, D-72076 Tübingen, Germany
[2] INAF-Osservatorio Astrofisico di Catania, via S. Sofia 78, I-95123 Catania, Italy
[3] Observatoire Astronomique, Université de Strasbourg & CNRS, UMR 7550, 11 rue de l'Université, F-67000 Strasbourg, France
[4] Departamento de Física de la Tierra y Astrofísica and IPARCOS-UCM (Instituto de Física de Partículas y del Cosmos de la UCM), Facultad de Ciencias Físicas, Universidad Complutense de Madrid, E-28040 Madrid, Spain
[5] Aix Marseille Univ, CNRS, CNES, LAM, Marseille, France
[6] INAF–Osservatorio Astronomico di Palermo, Piazza del Parlamento 1, I-90134 Palermo, Italy

Received 29 November 2019 / Accepted 07 March 2020

ABSTRACT

Context. Young field stars are hardly distinguishable from older ones because their space motion rapidly mixes them with the stellar population of the Galactic plane. Nevertheless, a careful target selection allows for young stars to be spotted throughout the sky.
Aims. We aim to identify additional sources associated with the four young comoving stars that we discovered towards the CO Cepheus void and to provide a comprehensive view of the Cepheus association.
Methods. Based on multivariate analysis methods, we have built an extended sample of 193 young star candidates, which are the optical and infrared counterparts of ROSAT All-Sky Survey and XMM-Newton X-ray sources. From optical spectroscopic observations, we measured their radial velocity with the cross-correlation technique. We derived their atmospheric parameters and projected rotational velocity with the code ROTFIT. We applied the subtraction of inactive templates to measure the lithium equivalent width, from which we infer their lithium abundance and age. Finally, we studied their kinematics using the second *Gaia* data release.
Results. Our sample is mainly composed of young or active stars and multiple systems. We identify two distinct populations of young stars that are spatially and kinematically separated. Those with an age between 100 and 300 Myr are mostly projected towards the Galactic plane. In contrast, 23 of the 37 sources younger than 30 Myr are located in the CO Cepheus void, and 21 of them belong to the stellar kinematic group that we previously reported in this sky area. We report a total of 32 bona fide members and nine candidates for this nearby (distance = 157 ± 10 pc) young (age = 10–20 Myr) stellar association. According to the spatial distribution of its members, the original cluster is already dispersed and partially mixed with the local population of the Galactic plane.

Key words. Stars: pre-main sequence – Stars: fundamental parameters – Stars: kinematics and dynamics – X-rays: stars

1. Introduction

The "natural" birth sites of stars are young open clusters and star-forming regions (SFRs) which are often tightly associated with emission nebulae and molecular clouds (e.g., Piskunov et al. 2008; Zinnecker 2008). However young stars are also found in wide regions around SFRs and also in the field, apparently unrelated to any of the known star-forming sites. Such populations of young stars are composed of both classical T Tauri stars (CTTSs) and weak-line T Tauri stars (WTTSs). There is evidence of different space distributions for CTTSs and WTTSs, the former located near the cloud cores while the latter are spread all around the SFR (e.g., Alcala et al. 1997). Moreover, WTTSs are on average older than CTTSs and have already dissipated their accretion disks (Bertout et al. 2007). These young stars may form substructures that can be located up to tens of parsecs away from the SFR's core (e.g., Mapelli et al. 2015).

In the 1990s, various scenarios for explaining the presence of dispersed young stars were proposed. For those located in the outskirts of SFRs or in the space surrounding them, the simplest explanation was that they had drifted by thermal velocity dispersion of gas within star-forming sites. On the other hand, those far away from any conventional SFRs should have formed locally from cloudlets in turbulent giant molecular clouds (Feigelson 1996). However neither of these theories could explain the presence of T Tauri stars (TTSs) with high space velocity, the so-called "runaway" TTSs (Sterzik et al. 1995). Their ejection could have occurred during the dynamical evolution of young multiple systems and come from close encounters with other members of their parent cloud (Sterzik & Durisen 1995, 1998; Gorti & Bhatt 1996).

The picture of star formation in our Galaxy is still not well-defined and new important details are being added by the recent

Send offprint requests to: A. Klutsch
e-mail: klutsch@astro.uni-tuebingen.de

⋆ Based on observations collected at the Isaac Newton Telescope (INT) operated on the island of La Palma by the Isaac Newton Group in the Spanish Observatorio del Roque de Los Muchachos of the Instituto de Astrofísica de Canarias, the 2.2-m telescope of the German-Spanish Astronomical Centre, Calar Alto (Almería, Spain), operated by the Max-Planck-Institute for Astronomy, Heidelberg, jointly with the Spanish National Commission for Astronomy, and the SOPHIE spectrograph on the 1.93-m telescope at Observatoire de Haute-Provence (CNRS), France (program 09A.PNPS.GUIL).
⋆⋆ Tables 1 and 3–5 are available at the CDS via anonymous FTP to cdsarc.u-strasbg.fr (130.79.128.5) or via http://cdsweb.u-strasbg.fr/cgi-bin/qcat?J/A+A/.

large spectroscopic surveys and astrometric space missions, such as *Gaia*. One of the most relevant results of the *Gaia*-ESO survey (Gilmore et al. 2012; Randich et al. 2013) is the discovery of two kinematically distinct populations (A and B) in the field of both the Gamma Velorum (Jeffries et al. 2014) and NGC 2547 (Sacco et al. 2015) clusters. The properties of sources belonging to Gamma Velorum B and NGC 2547 B are fairly similar in terms of age and kinematics. Since these two clusters are close to each other ($\approx 6^\circ$ on the sky corresponding to about 40 pc at their distance) and both are in the field of the Vela OB2 association, the B populations of these two clusters might form an extended low-mass population in the Vela OB2 association.

Over the past two decades, several nearby (30–150 pc) young (5–70 Myr) associations were identified, mostly in the southern hemisphere (Zuckerman & Song 2004). Torres et al. (2006, 2008) found many of them and their members during the SACY survey. The use of a Bayesian analysis and, subsequently, the BANYAN Σ multivariate Bayesian algorithm contributed significantly to the continued identification of new members, mainly low-mass stars and brown dwarfs (Malo et al. 2013; Gagné et al. 2014, 2015a,b, 2018a). The first release of the *Gaia* mission (Gaia Collaboration et al. 2016) improved the astrometric accuracy for the *Tycho* sources. This has made it possible to search for new comoving stars (Oh et al. 2017), as well as stellar kinematic groups and clusters (Faherty et al. 2018; Gagné et al. 2018b). Based on the very accurate astrometry from the second data release of the *Gaia* mission (*Gaia* DR2, Gaia Collaboration et al. 2018), Gagné & Faherty (2018) discovered a considerable number of likely new members in these young associations.

However, it remains difficult to recognize the young stars without a circumstellar disk in the field among the Galactic plane stellar population. Neither their global photometric properties nor the presence of nearby gas differentiates them from older stars. An efficient methodology for identifying the young stars is through the use of large X-ray surveys because the stellar X-ray sources in the ROSAT catalog are mainly stars younger than 1 Gyr (e.g., Motch et al. 1997a). Guillout et al. (1998a) showed that this stellar population can be used as a tracer of young local structures, like the late-type stellar population in the Gould Belt (Guillout et al. 1998b). To this end, Guillout et al. (1999) cross-correlated the ROSAT All-Sky Survey (RASS) with the *Tycho* catalog building the first large dataset ($\approx 14,000$ objects) of late-type stellar X-ray sources, the so-called *RasTyc* sample.

Spectroscopic surveys of northern *RasTyc* sources were performed by Guillout et al. (2009, Paper I) and Frasca et al. (2018, Paper III). In Paper I, we identified five young field stars in the optically bright ($V < 9.5$ mag) sample. Afterwards, BD+44 3670 and BD+45 598 were recognized as members of the Columba association (∼30 Myr; Zuckerman et al. 2011) and of the β Pic moving group (∼12 Myr; Moór et al. 2011), respectively. Klutsch (2008) noticed that an almost uniform spatial density of young stars in the optically bright *RasTyc* sample. At the same time, the spatial density in the northern hemisphere (Paper I) is about one order of magnitude lower, on average, than that in the southern hemisphere (the SACY survey). This is consistent with the significant asymmetry in the all-sky *RasTyc* map with respect to the Galactic plane, as reported by Guillout et al. (1998a), and is likely related to the structure of the Gould Belt. A higher fraction of young stars was found in the optically faint sample (Paper III). This may be due to the larger distances involved, on average, in the faint survey, which facilitated the detection of many more intrinsically brighter X-ray (more active and younger) sources when compared to the bright sample. A larger contribution from the Gould Belt, which is more distant in the northern hemisphere, can also explain these differences.

Klutsch (2008) analyzed the early spectroscopic observations of optically faint *RasTyc* sources. This led to the discovery of an over-density of stellar X-ray sources near the Cepheus-Cassiopeia complex. We refer the reader to the reviews on SFRs in the Cassiopeia and Cepheus constellations of Kun (2008) and Kun et al. (2008), respectively. Although this sky area is rich in CO molecular regions (Dame et al. 2001) and dark clouds (Dobashi et al. 2005; Kiss et al. 2006), Guillout et al. (2010, Paper II) identified four comoving TTSs towards a region devoid of interstellar matter that is denoted as the fourth void in the Cepheus Flare region by Kiss et al. (2006). Moreover, Tachihara et al. (2005) had already reported the discovery of 16 WTTSs in this region. In Paper III, we found four other likely members of this group based on their spectral characteristics, position in the HR diagram, and kinematic properties. The group 38 in Oh et al. (2017) and Faherty et al. (2018) is composed of seven stars all belonging to the young association analyzed in the present paper and formerly discovered by our group (Klutsch 2008; Paper II), which already included four of their seven stars; here, we extend the census of this young association.

The main aim of the present work is to identify other young stars surrounding the four comoving TTSs in Cepheus reported in Paper II, and to characterize their physical and kinematic properties, including the WTTSs provided by Tachihara et al. (2005). In Sect. 2 we detail our procedure to build a sample of "young star candidates", based on the data available in 2009, when it was created. We also describe our campaign of optical spectroscopic observations. Section 3 presents our analytical methods and results thereof. In Sect. 4 we mainly focus the discussion on the properties of the selected sources, on the spatial distribution and kinematics of the young stars belonging to the young association towards the CO Cepheus void, and on its reliability. Finally, we outline our conclusions and perspectives in Sect. 5. We present the extraction of spectra with a double Gaussian profile in Appendix A. We also provide further information on multiple systems (Appendix B), low-mass stars (Appendix C), and a few specific targets (Appendix D).

2. Sample and observations

2.1. Sample selection

The greatest difficulty in finding young stars in the field is the selection of a suitable sample of candidates. The best manner for identifying such a population is to excavate into an extensive and comprehensive sample of stellar X-ray sources, such as the *RasTyc* sample (Guillout et al. 1999, Papers I and III).

To this end, we picked out all counterparts of the X-ray sources by cross-matching the RASS catalog (Voges et al. 1999, 2000) with the Two Micron All-Sky Survey catalog (2MASS, Skrutskie et al. 2006) using a likelihood ratio approach and an original way to estimate the rate of spurious associations (Pineau et al. 2008a,b, 2011; Pineau 2009). We discarded all the matches having an angular separation larger than 15″ and a probability of identification less than 0.7. We then correlated the remaining sources with the Guide Star Catalog II (GSC II, Lasker et al. 2008). We kept all the optical sources at an angular distance not exceeding 5″ from 2MASS sources and 15″ from RASS ones.

We proceeded in a similar way for the XMM-Newton X-ray sources of the 2XMMi catalog (Watson et al. 2009). This turned

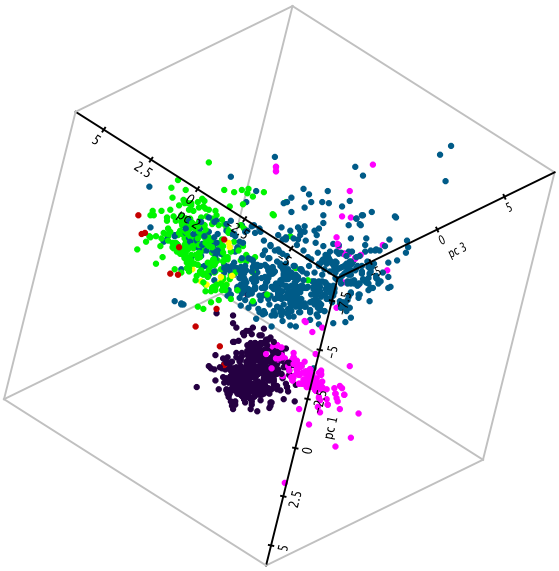


Fig. 1. Result of the principal component analysis applied to RASS X-ray sources. The 3D scatter plot displays the three first components, adopting different colors for quasars (green dots), galaxies (blue dots), and stars (other dots). Such a method optimizes the disentangling of various classes of X-ray emitters. The pink dots denote the locus of a priori young stars selected using our learning sample (see text).

out to be quite inconclusive because we only selected three stars. However, we note that the source 1RXS 184257 (= [KP93] 2−43 in Kun & Prusti 1993), which is a well-known young visual binary, is part of the selection. That makes us confident in the effectiveness of our approach, even for optically faint sources.

We then applied a multivariate analysis on these two X-ray selected datasets. A principal component analysis, which takes measurements errors (Pineau et al. 2008b) on 19 parameters into account, was used to build up linear combinations of flux ratios from X-ray to near-infrared (NIR) wavelength domain, X-ray hardness ratios, and color indexes. Applying a mean shift procedure on the three first principal components, we were able to disentangle the stellar population from the extragalactic component (galaxies and quasars) that also emits X-rays (Fig. 1). We followed the guidelines of Pineau et al. (2011) to identify the local maximum of the population of well-known young stars in this three-dimensional space. We therefore built a reliable learning sample composed of sources whose object type is either "young stellar object", "T Tau-type star", or "pre-main-sequence star" in the Simbad database. We finally labeled all the likely stellar X-ray sources located in the latter region as our young star candidates. The objects are distributed all over the sky.

This work is focused on the identification of young stars towards the CO Cepheus void and its surroundings. Therefore, we selected all the young stars located in a 30°-wide region encompassing the four comoving TTSs discovered in Paper II in that region and we then restricted our sample to the population of late-type (B–V > 0.5 mag) and faint (V > 9 mag) stars. Relying on the photometric distance estimate of the group (Paper II), we retain all the candidates within 170 pc of the Sun and with X-ray luminosity $L_X \geqslant 10^{29}$ erg s^{-1} (Guillout et al. 1998b). This X-ray emission threshold picks the majority of 1 Myr-old stars with spectral type G and K (Preibisch et al. 2005). The choice of these selection criteria and of this vast sky area allows us *i)* to look for additional bona fide members both in a restricted region around the Cepheus void and far away (i.e., to search for any runaway WTTSs), and *ii)* to characterize the population of stellar X-ray sources in an under-researched sky area. The 162 strongest stellar X-ray sources, which are also a priori the youngest stars selected, form our list of prime targets.

The low-resolution spectroscopic survey by Tachihara et al. (2005) includes 14 sources common to our sample, as well as one analyzed in Paper II (i.e., TYC 4500-1478-1). We decided to add the remaining 31 stars from Tachihara et al. (2005) to our sample, which leads to a total of 193 candidates. Table 1 lists their basic data, together with that of the eight young stars reported in Papers II and III (labeled as G1–G4 and F1–F4, respectively).

2.2. Photometric and astrometric data

The selection of young star candidates to be observed spectroscopically was performed before the launch of *Gaia*. At that time, only two of the 193 pre-selected candidates had reliable *Hipparcos* parallaxes, while 102 sources, which are included in the *Tycho* catalog (ESA 1997), had unreliable parallaxes and proper motions with a fair accuracy. We therefore needed multiband photometric data (from optical to infrared wavelengths) to select the young star candidates with the multivariate analysis described in Sect. 2.1. However, meanwhile, the *Gaia* DR2 catalog reports very accurate parallaxes and proper motions for nearly all the sources investigated in the present paper, which allows us to study their kinematics and evolutionary status.

Since we only selected stellar X-ray sources with a 2MASS counterpart, their photometry in the NIR wavelength domain is homogeneous. The J, H, and K_s magnitudes of the targets are in the range 7–12 mag and have generally a high level of accuracy (in more than 96 % of cases). For seven sources, at least one of NIR magnitudes is an upper limit or a poor-quality value in the final release of 2MASS data.

We encountered difficulties with the homogenization of photometry in optical bands. Indeed, when we started our target selection, no catalog provided Johnson B and V magnitudes up to V = 14.5 mag. The completeness of the *Tycho*-2 catalog (Høg et al. 2000) is to about 90 % for sources brighter than $V \sim$11.5 mag, although it also contains fainter stars. For the non-*Tycho* sources fainter than V = 12 mag, only the photographic magnitudes were available and reliable. For the 102 sources with an entry in the *Tycho*-2 catalog, the V_T magnitude ranges from 9 to 13 mag (Fig. 2). We converted the B_T and V_T magnitudes into Johnson B and V magnitudes following the transformation given in the introduction of the *Tycho*-2 catalog: $B = B_T - 0.24(B_T - V_T)$ and $V = V_T - 0.09(B_T - V_T)$.

For 79 of the remaining sources with both B_J and R_F photographic magnitudes in the USNO-B1.0 catalog (Monet et al. 2003), we estimated the V magnitude using the formula proposed by Lépine & Shara (2005): $V = B_J - 0.46(B_J - R_F)$. We used the B_J and R_F magnitudes extracted from the second Palomar Observatory Sky Survey (POSS) scans in the IIIa-J and IIIa-F passbands, respectively. All these sources are fainter than V = 11 mag. Additional magnitudes in the Johnson B band were retrieved either from the GSC II catalog or from the unpublished Yellow-Blue 6 catalog (YB6 − USNO). The latter is available through the NOMAD catalog (Zacharias et al. 2004).

In Table 1, we mainly list the B and V magnitudes in the Johnson-Cousins system (∼88 % and ∼94 % of sources). If one of these values are not available, we substitute them by the B_J or V photographic passbands taken from GSC II (Fig. 2).

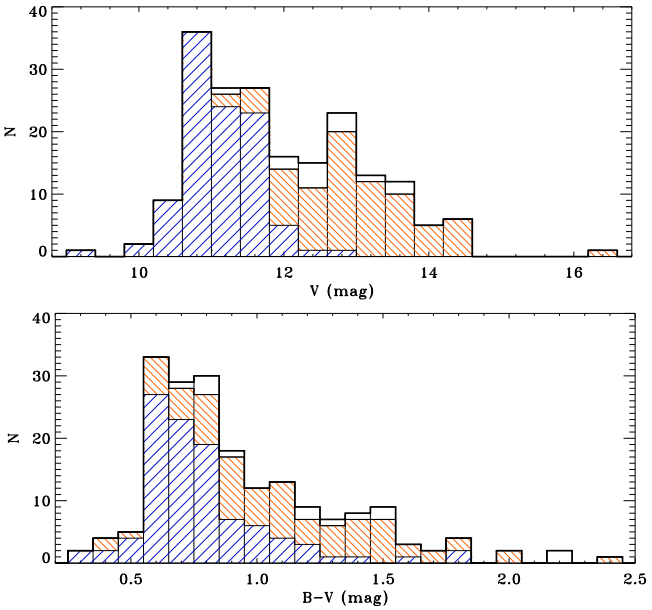


Fig. 2. Distributions of V magnitude *(upper panel)* and B–V color index *(lower panel)* for our targets. The blue and red stripes correspond to the *Tycho* and USNO-B1.0 magnitudes converted into the Johnson V magnitudes based on the relations of Høg et al. (2000) and Lépine & Shara (2005), respectively (see text for details). The white areas mark the V photographic (GSC II or YB6) ones.

However, for the analysis of the spectral energy distribution (Sect. 3.3) we have updated the magnitudes with more accurate values of B and V retrieved from the AAVSO Photometric All Sky Survey (APASS, Henden et al. 2015) catalog. The V magnitudes are also available in the TASS Mark IV patches photometric catalog (Droege et al. 2006). For most sources we retrieved the I_C magnitudes from the TASS catalog or, if not available, from the catalog of Gorbikov & Brosch (2014). In this way, the dataset of the magnitudes is homogeneous and avoids a mixture of photometric and photographic estimates. We found 177 (plus three whose V magnitude is not provided) and 166 sources in common with the APASS and TASS catalogs, respectively. The different datasets are consistent with the V magnitudes in Table 1, with a Pearson's correlation coefficient (PCC) of ∼0.967. We also note that the V magnitudes in APASS and TASS catalogs are fully consistent with each other (PCC ∼ 0.992). In the case of the bright sources ($V \leqslant 13$ mag), we obtained a good agreement between the various magnitudes and the spread increases towards the faintest objects, as expected in such a comparison. Regarding the faint objects ($V > 13$ mag), the V magnitudes in Table 1 tend to be overestimated by 0.5 mag. This corresponds to the typical accuracy of the Lépine & Shara (2005) relation at this brightness, which might be subject to systematic errors and other effects.

The photometric standard errors of the *Tycho* sources with $9 < V_T < 12$ are typically 0.15 and 0.1 mag in B and V passbands, respectively, while they are ∼0.25 mag in both bands for the faintest sources. The tabulated errors of the GCS II sources are ∼0.3 mag for the V magnitudes and ∼0.4 mag for both the B and B_J magnitudes. The error on the optical magnitudes for the sources fainter than $V = 12$ mag is considered to be at least of 0.5 mag. For our targets, the typical error for the APASS photometry is instead 0.05 mag.

Table 2. Instrumental setup summary.

Telescope	Inst.	Spectra	Spectral region	$\lambda/\Delta\lambda$
INT 2.5-m	IDS	1D	5800–7200 Å	9,200
CAHA 2.2-m	FOCES	échelle	3800–10000 Å	28,000
OHP 1.93-m	SOPHIE	échelle	3872–6943 Å	39,000

Five of the six sources with a B–V color index below our threshold of 0.5 mag come from the inclusion of the Tachihara et al. (2005) sample. The use of APASS magnitudes leads to the same statement for sources #176 and #178 only. Regarding the remaining source (#102), its color index of 0.546 ± 0.276 mag in the APASS catalog fulfills our initial selection criterion.

2.3. Observations and data reduction

To study the physical and kinematic properties of all these young star candidates, we conducted observing campaigns using three spectrographs (Table 2). We acquired both intermediate- and high-resolution optical spectra, sharing our candidates in an optimized way, depending on their brightness.

We observed the brightest ($V \leqslant 12$ mag) targets with two instrumental setups. From 26 to 27 September 2009, we used the cross-dispersed échelle SOPHIE[1] spectrograph (Perruchot et al. 2008; Bouchy et al. 2009) mounted on the 1.93-m telescope of the Observatoire de Haute Provence (OHP, France). The EEV-4482 detector is a thinned, back-illuminated, anti-reflection coated 4k×2k 15-μm-pixel CCD cooled at −100°C, with fast-readout mode. We chose the high-efficiency mode equipped with a double-fiber scrambler to homogenize and stabilize the illumination of the spectrograph entrance. This allowed us to record the 39 spectral orders covering effectively the wavelength range 3872–6943 Å, with a resolution of about 39,000 at 5500 Å. The data were treated using the automatic data-reduction pipeline, adapted from the HARPS software.[2]

From 2 to 5 October 2009 and on 12 December 2009, we completed our survey of the bright targets. The échelle spectra were taken with the fibre optics Cassegrain échelle spectrograph (FOCES, Pfeiffer et al. 1998) at the 2.2-m telescope of the German-Spanish Calar Alto Observatory (CAHA, Sierra de Los Filabres, Spain). We adopted the unique-fiber mode and chose the Site#1d detector, a 2048×2048 24 μm-pixel CCD. We used the configuration with the 400 μm-slit width, leading to a resolution of about 28,000 and covering the wavelength range from 3800 to 10000 Å, in a total of 100 orders. Using tasks of the ECHELLE package within the IRAF environment, we reduced the data following the standard steps of background subtraction, division by a flat-field spectrum given by a halogen lamp, wavelength calibration using the emission lines of the Th-Ar arc lamp, and normalization to the continuum through a polynomial fit.

The optically faint candidates ($12 < V < 14.5$ mag) were observed with the Intermediate Dispersion Spectrograph (IDS)[3] at the 2.5-m Isaac Newton Telescope (INT) of the Observatorio del Roque de los Muchachos (La Palma, Canary Islands, Spain). We acquired long-slit spectra during several observing runs that took place in 4–10 September 2009, 23–28 November 2010, 24–27 October 2012, 27 March to 2 April 2013, 16–20 November 2013,

[1] http://www.obs-hp.fr/guide/sophie/sophie-eng.shtml
[2] http://www.eso.org/sci/facilities/lasilla/instruments/harps/
[3] http://www.ing.iac.es/Astronomy/instruments/ids/

and 18–20 February 2014. During the observing night of 12 to 13 December 2009, some of our targets were also observed in queue mode. We used a slit width of 0.″95 and the H1800V dispersion grating with the 235 mm Camera (2148×4200 EEV10a CCD detector until 2010 and 2*k*×4*k* RED+2 CCD detector since 2012) and with slow-readout mode. We chose the central wavelength of 6500 Å. As the outer regions of the dispersed light beam are severely vignetted by the camera optics, only 2070 of the pixels (roughly from pixel number 1000 to 3070 in the direction of the dispersion) are clear and unvignetted regarding the H1800V grating. This allows for efficient coverage of the wavelength range 6200–6800 Å, with a resolving power of about 9200. For most of our targets and standard stars, we set the slit position angle to the current parallactic angle. Using the typical `IRAF` tasks, all spectra were de-biased, flat-fielded, distortion-corrected, wavelength calibrated (using the emission lines of the Cu-Ar and Cu-Ne lamps), and finally normalized to the continuum. When a source was already reported as a visual binary in the literature or was identified as such during our observing runs (i.e., with a small angular separation), we aligned the slit on its position angle to simultaneously acquire the spectra of both sources. In this way we made sure to observe the optical counterpart(s) of the unresolved X-ray source. We subsequently examined whether or not the two stars form a physical binary system. When their seeing profiles are partially overlapped on the CCD, we extracted the two spectra by means of a `IDL` code similar to that of Frasca et al. (1997), rather than the `IRAF` task `APALL` (see Appendix A for details). The use of a double Gaussian profile optimizes the spectrum extraction of the fainter source, which may be heavily contaminated by the brighter one.

We removed the telluric water vapor lines only in the spectral region around the Hα line of every spectrum, in all instrumental setups. We applied a method similar to that described by Frasca et al. (2000) using telluric templates taken with the same instrumentation as the targets. We show a few results for the case of SOPHIE spectra (Fig. E.1) to illustrate its effectiveness.

Owing to bad weather conditions during our IDS observing runs, we were unable to obtain a spectrum for 35 of our targets. All the unobserved targets have a lower priority because their Galactic latitude is higher than 25° or they were not classified as WTTSs by Tachihara et al. (2005). Figure E.2 shows the spectra acquired in the region around the Li I λ6707.8 lines.

3. Analysis and results

3.1. Radial velocity and multiplicity

We measured the heliocentric radial velocities (*RV*s) using the cross-correlation technique. We distinguished spectroscopic systems from single stars (or single-lined binaries) based on the number of peaks visible in the cross-correlation function (CCF).

Regarding the IDS data, we cross-correlated each long-slit spectrum of our targets with that of RV-standard stars observed during the same night. For this purpose, we have upgraded the `IDL` procedure described in Klutsch (2008) and Paper I. We masked the spectral range around the Hα line because of its strong wings and the possible chromospheric emission in the core that can considerably broaden and distort the CCF peak. For the same reason we discarded the spectral regions strongly affected by telluric absorption lines. When only one CCF peak was detected, the code performs an additional analysis to report any asymmetry of the CCF profile, possibly interpreted as an SB2 system observed near the conjunction. Such a procedure is only relevant when the masses of the two stars differ significantly. We computed the errors of the pixel shift from the center of the Gaussian function fitting the CCF. We computed the *RV* errors as a function of the fitted peak height and the antisymmetric noise through the *R* factor, as described in Tonry & Davis (1979).

For the FOCES data we derived the *RV* values with the `IRAF` task `FXCOR`, by cross-correlating each échelle order of the target spectra with the corresponding one of the most similar RV-standard star, which was acquired during the same run. We discarded the orders heavily contaminated by telluric lines or those including very broad lines and activity indicators, such as the Ca II H & K lines, the Balmer series (Hα and Hβ), and the Ca II IR triplet lines. We fitted the entire CCF peak with a Gaussian to measure more precisely the *RV* values, which were obtained as the weighted average of all the individual *RV* measurements computed by `FXCOR` per each échelle order. The resulting *RV* uncertainty is the standard error of the weighted mean, σ_{RV}.

The *RV* measurements derived from the target spectra acquired with the SOPHIE spectrograph were performed with the cross-correlation analysis that is included in the automatic data-reduction pipeline developed by the OHP staff. We used the most appropriate mask depending on the *B*–*V* color index (or spectral type) of the target, among the five available ones. This procedure failed for some of the multiple systems and fast rotators. From a first guess of their spectral type (Sect. 3.2), we selected the most appropriate synthetic spectrum from the POLLUX database (Palacios et al. 2010) to be used as template for computing the CCF, which was automatically fitted by a procedure similar to that used for IDS data. Taking advantage of the high resolution of these spectra, we improved the code to detect and fit the CCF peak of a companion even having a much lower brightness in a stellar binary system, that is, with a low mass-ratio. This requires careful analysis of the CCF residues after subtracting the best fit, especially when the two peaks are severely blended (i.e., one CCF peak with an asymmetric shape).

Table 3 contains all our *RV* measurements and associated errors, with one entry for each acquired spectrum and, in case of multiple systems, for each component.

Since our `IDL` procedure and the task `FXCOR` use the RV-standard stars as templates, we need an accurate *RV* value for them. So we used the *RV* measurements available from the Élodie archive,[4] which were derived from high-resolution spectra. Table E.1 lists all these values that agree with those in Nidever et al. (2002) or other compilations of *RV* measurements (e.g., Gontcharov 2006; Kharchenko et al. 2007).

For multiple systems, we adopted an independent Gaussian fit for each CCF peak whenever they are not blended (i.e., far from the conjunctions). We used instead a multiple-Gaussian fit algorithm when the spectral lines are partially blended. Moreover, we automatically looked for any significant peaks in the CCF and fitted them with single, double, or multiple functions (i.e., up to four Gaussian profiles), using our `IDL` code that computes the CCF and treats the errors as `FXCOR` does. We refer the reader to Paper I for details on this code and its performances.

Among the 47 sources observed at multiple epochs, eleven sources display a large variation in radial velocity (Table 3). We classified those with *RV* change significantly larger than the *RV* errors as single-lined binaries (`SB1`) and those with smaller *RV* variation as possible SB1 systems (`SB1?`). We discovered that

[4] http://atlas.obs-hp.fr/elodie/

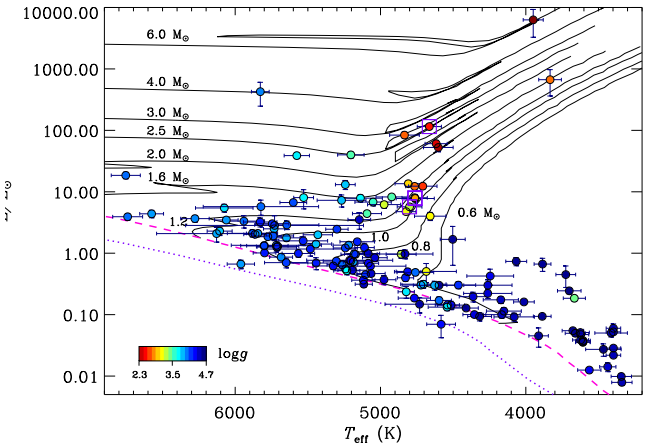


Fig. 3. HR diagram of targets with known APs and parallaxes. The symbols are color coded by $\log g$ derived from spectra (Sect. 3.2). The four lithium-rich sub-giant or giant stars are enclosed in open squares (Sect. 3.4). The evolutionary tracks from the ZAMS of Girardi et al. (2000) are shown as solid lines with the labels representing their masses. The dashed and dotted lines display the ZAMS with solar metallicity ($Z = 0.019$) and $Z = 0.001$ by the same authors, respectively.

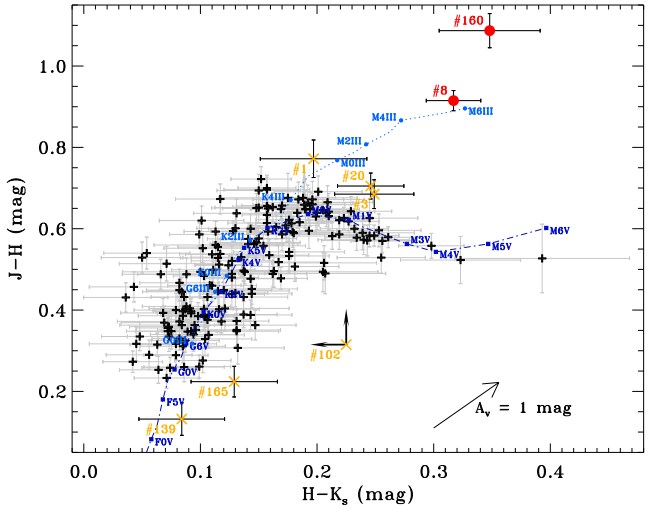


Fig. 4. (H–K_s, J–H) color-color diagram of our targets. We also display the intrinsic color tracks of main-sequence (MS; dash-dotted line) and giant (dotted line) stars from Bessell & Brett (1988), which we converted into the 2MASS photometric system using the Carpenter (2001) relation. Eight sources lie outside the locus of MS stars: two sources likely suffering from extinction (red circles) and six sources with possibly small extinction or poor-quality infrared magnitudes (orange crosses). We also overplot their error bars, except for source #102 because its J and K_s magnitudes are upper limits in 2MASS. The arrow indicates the reddening vector for $A_V = 1$ mag. For a better readability, the source #120 with H–$K_s = -0.152 \pm 0.045$ mag does not appear.

44 of the surveyed sources are multiple spectroscopic systems, which are distributed as follow: nine SB1 (4.8 %), 28 double-lined (SB2) plus four likely SB2 (17.2 %), and three triple (SB3; 1.6 %) systems (see Table B.2). This corresponds to 20 % of the overall sample (i.e., our targets, plus the 20 sources listed in Table B.1 and the eight sources from Papers II and III) and to 24 % of the sources with new observations presented here, as listed in Table 3. For the 17 sources classified as possible spectroscopic systems (Table B.2), additional observations are needed to draw firm conclusions on their multiplicity.

3.2. Spectral classification and projected rotational velocity

We applied the IDL code ROTFIT (Frasca et al. 2006) to perform the physical characterization of SB1 systems and single stars, that is, those with only one peak in the CCF profile. This code searches for the best combination of parameters by comparing the target spectrum with reference star spectra that are rotationally broadened until a minimum χ^2 was reached. As in our previous works (Papers I and III), we determined the spectral type (SpT), effective temperature ($T_{\rm eff}$), gravity ($\log g$), and metallicity ([Fe/H]) using as templates a library of 270 high-resolution spectra of low-activity and slowly rotating stars retrieved from the Élodie archive (Moultaka et al. 2004). For these stars we took the atmospheric parameters (APs) from the PASTEL catalog (Soubiran et al. 2010). We report these results in Table 3 in which any source observed at several epochs[5] has multiple entries. The typical accuracy on the spectral type is about one subclass. We refer the reader to Appendix C for a description of our procedures dedicated to the analysis of the M-type stars.

To minimize possible effects on projected rotational velocities ($v \sin i$) due to different resolutions and instrumental setups between the target spectra (acquired with both IDS and FOCES) and the Élodie ones we also used a smaller library of template spectra taken with these spectrographs during our observing runs. Table E.1 lists them as well as all their relevant information. Analogous to the treatment of the full library of Élodie templates, the rotation velocity of each template is progressively increased by convolving its spectrum with a rotational profile of a given $v \sin i$. The best match of the template spectrum with the target spectrum, found by χ^2 minimization, gives us the value of $v \sin i$. We note that most $v \sin i$ values derived with the Élodie templates are slightly underestimated compared to those obtained when the spectra are taken with the same instrumental setup. This is probably caused by the resampling of the Élodie spectra on the points of the IDS or FOCES ones. We thus adopted the $v \sin i$ values obtained with the template acquired with the same spectrograph as the target (Table 3). At the IDS, FOCES, and SOPHIE resolutions, any $v \sin i$ determination is reliable only if the $v \sin i$ value is larger than 15 km s^{-1}, 5 km s^{-1}, and 2 km s^{-1}, respectively. We determined these lower limits with simulations similar to those made by Frasca et al. (2015).

3.3. Stellar luminosity and extinction

We analyzed the spectral energy distribution (SED) of our targets with the aim of checking the spectroscopic atmospheric parameters, of estimating the extinction, A_V, and of deriving the stellar luminosities. The $BVI_C JHK_s$ SEDs were constructed using the optical and NIR photometric data described in Sect. 2.2. We completed them with mid-infrared photometry provided by the WISE All-Sky survey (Wright et al. 2010; Cutri et al. 2012).

Figure 3 shows the Hertzsprung-Russell (HR) diagram for the targets with accurate parallaxes (Table 4) and APs derived in the present study (Table 3). For 187 of our targets we made use of the *Gaia* DR2 parallax, while we adopted the values of

[5] whether with different instruments (usually for the bright sources) or with the same instrumental setting (in case of the faint ones).

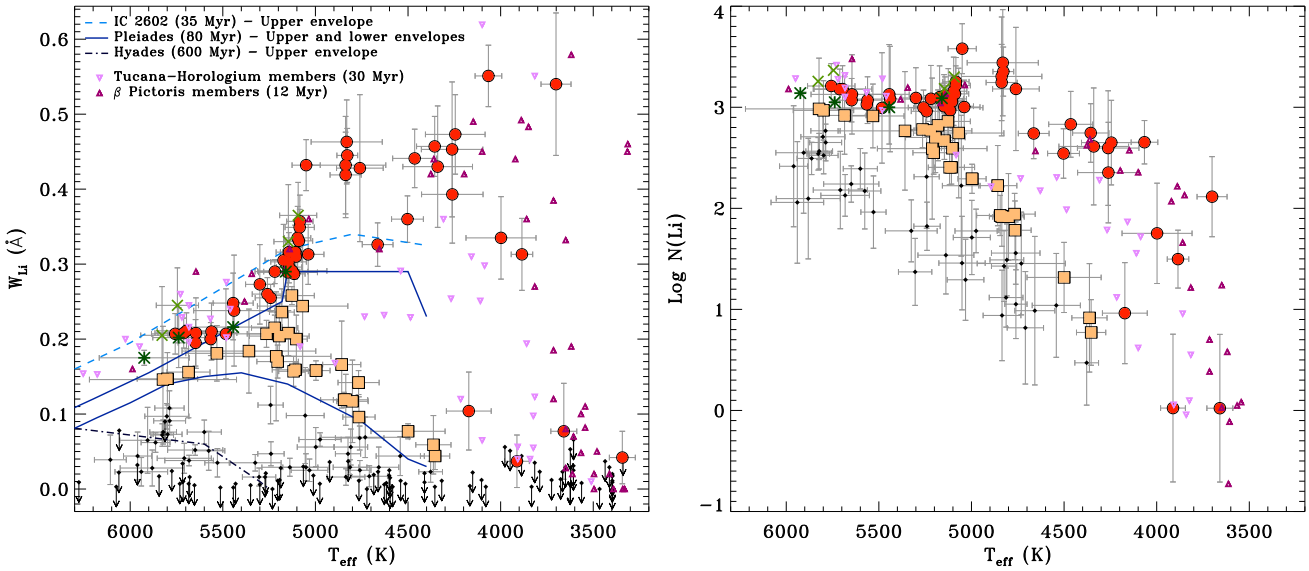


Fig. 5. *Left panel*: Li I λ6707.8 equivalent widths as a function of effective temperatures for our targets. Since each symbol results from the analysis of a unique spectrum (Table 3), any source observed at multiple epochs is marked several times. The arrow symbols indicate the upper limits on lithium equivalent width. The lines of different color and style mark the boundaries for three young clusters. *Right panel*: lithium abundances versus effective temperatures. We disregard the upper limits. In both panels, we display the PMS-like (big filled circles), Pleiades-like (filled squares), and older (filled diamonds) stars (see Sect. 3.4 for details). The four comoving TTSs towards the CO Cepheus void (Paper II) and the additional members (Paper III) are highlighted with asterisks and crosses, respectively. For comparison, we also overplot the locus of the sources belonging to two young (age = 12–30 Myr) associations listed by da Silva et al. (2009) with different small triangles.

18.4 ± 2.7 mas and 36.0 ± 6.9 mas for the sources #15 and #101, respectively, as quoted in the URAT Parallax Catalog (Zacharias et al. 2015; Finch & Zacharias 2016). No parallax is available for the remaining four targets. Evidently, the values of $\log g$ found by our spectroscopic analysis are fully consistent with the evolutionary status in the HR diagram, demonstrating the reliability of APs derived by ROTFIT (Sect. 3.2). Most targets are located close to (or slightly above) the zero-age main sequence (ZAMS) and show $\log g$>3.5. These are good young star candidates. As for the 16 sub-giant or giant stars, the X-ray emission can be related to their evolutionary status or to the presence of an unseen companion, which forces the evolved star into fast rotation.

We adopted the grid of NextGen low-resolution synthetic spectra, with $\log g$ in the range 3.5–5.0 and solar metallicity by Hauschildt et al. (1999), to fit the optical-NIR portion (from B to H band) of the SEDs, in the same way as in Paper III. We fixed $T_{\rm eff}$ and $\log g$ of each target to the values found with ROTFIT (Table 3) and let the angular stellar diameter and the extinction A_V vary until a minimum χ^2 was reached. For the stars with a known distance, this also provides us with a measure of the stellar radius and luminosity that was obtained by integrating the best-fit model spectrum. As listed in Table 4, we found low extinction values (A_V < 0.5 mag), with the exception of the more distant targets, which are mostly sub-giant or giant stars.

In line with our selection criteria, most of our targets are consistent with late-type stars near the main sequence (Fig. 3), with no or low reddening (Table 4). These results fully agree with the distribution of our targets in the infrared color-color diagram (Fig. 4). We found nine sources that lie outside the locus of main-sequence (MS) stars. For a better readability the source #120 with H–$K_{\rm s}$ = −0.152 ± 0.045 mag is not shown. Sources #8 and #160 likely suffer from extinction, as they lie at the upper right corner in the color-color diagram (J–H > 0.9 mag and H–$K_{\rm s}$ > 0.3 mag). These color excesses E(J–H) and E(H–$K_{\rm s}$) allow us to estimate their extinction A_V by means of the mid-infrared extinction law of Wang & Chen (2019) and the standard optical one $R_{\rm V}$ = 3.1. We classified the source #8 as a K5 giant star with a temperature $T_{\rm eff}$ = 3833 ± 78 K and a surface gravity $\log g$ = 2.84 ± 0.44, while its infrared colors place it near the position of an M6 giant star, implying an extinction of ∼2 mag. Moreover, this source is at least 2 mag fainter than giants having a similar J–$K_{\rm s}$ color index in the LSPM-North catalog (Lépine & Shara 2005). This is consistent with a high reddening, as also indicated by the SED analysis. Source #160 is a known member of the L1251 cloud (Kun & Prusti 1993) and classified as a WTTS with spectral type K5 (Kun et al. 2009), implying an extinction of ∼3 mag. The other sources outside the locus of MS stars include two visual binary candidates (#102 and #120, see Table 5), one spectroscopic system (#20), and four possible single stars (#1, #3, #139, and #165). We note that the entire photometry of the source #139 could be affected by the extended halo of light of the nearby B5 binary V447 Cep (see Appendix D).

3.4. Lithium content and age

Lithium is a fragile element that is progressively depleted in the deep convective envelopes of late-type stars where it is brought at temperatures of about 3×10^6 K. Therefore, the strength of the Li I λ6707.8 Å line can be used as an age proxy for dwarfs with spectral type later than mid-G; for these stars, a high lithium abundance is a clear sign of youth (e.g., Soderblom et al. 1998).

In all instrumental setups used in this study, the lithium line and the nearby Fe I λ6707.4 Å line are blended, at least partly. However, when applying the spectral subtraction technique (see, e.g., Herbig 1985; Barden 1985; Frasca & Catalano 1994; Montes et al. 1995), this contamination is automatically

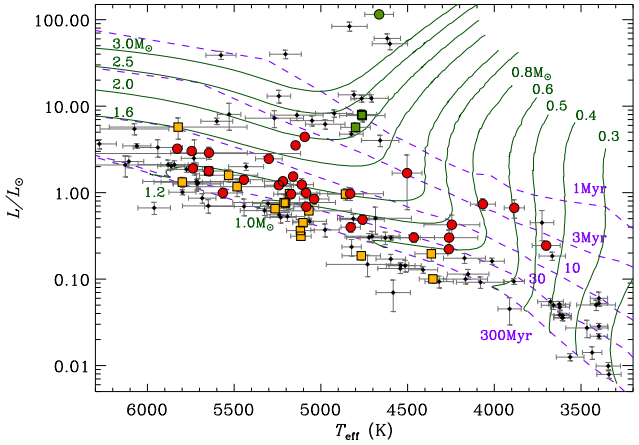


Fig. 6. HR diagram of our targets with known APs and parallaxes. We display the young stars selected as PMS-like (red circles) and Pleiades-like (orange squares) sources, along with the lithium-rich sub-giant or giant stars (green symbols) and older (black diamonds) sources. The pre-main-sequence evolutionary tracks of Siess et al. (2000) are shown as solid lines with the labels representing their masses. The dashed lines denote the isochrones at ages of 1, 3, 10, 30, and 300 Myr.

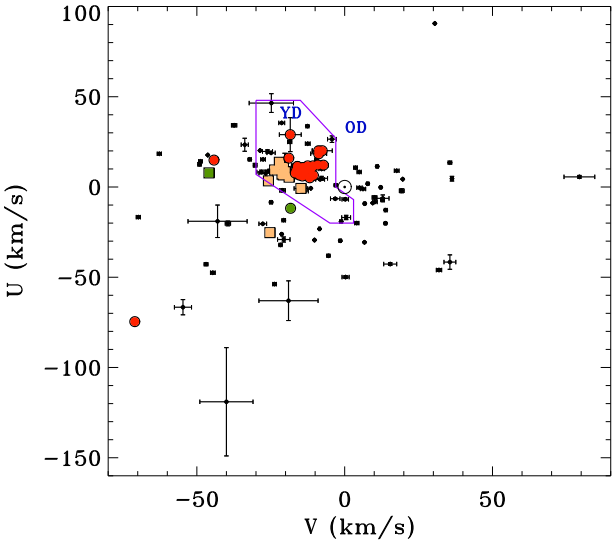


Fig. 7. (U, V) plane of targets with astrometry and RV value (Table 4). The solid line marks the separation between the young- (YD; age < 2 Gyr) and old-disk (OD) populations in the solar neighborhood, according to Eggen (1996). We use the same symbols as in Fig. 6.

corrected because the best-fitted lithium-poor template, which is rotationally broadened by ROTFIT to the $v \sin i$ of the target, faithfully reproduces the spectral behavior around the lithium line (Fig. E.2). We measured the Li I equivalent width, $W_{\rm Li}$, for the whole sample of single stars and SB1 systems (Table 3). We then derived the lithium abundance, $\log N$(Li), based on the Pavlenko & Magazzu (1996) calculations.

Following the classification of Papers I and III, we defined as Pleiades-like the stars lying between the lower and upper envelopes of the Pleiades cluster in the $T_{\rm eff}$–$W_{\rm Li}$ diagram (filled squares in Fig. 5). Since the lower envelope of the Pleiades nearly coincides with the upper envelope of the 300-Myr-old UMa cluster (Soderblom et al. 1993b), the age of Pleiades-like objects should range between 100 and 300 Myr. Analogously, we have considered as PMS-like the stars lying above the Pleiades upper envelope (filled circles in Fig. 5).

In the literature, a significant scattering of $\log N$(Li) was found for stars belonging to the same cluster. This can be due to a real age spread within the cluster or to further parameters affecting the lithium depletion, such as stellar rotation (e.g., Jeffries 2017; Bouvier et al. 2018, and references therein). For a field star, this prevents any direct conversion of $\log N$(Li) into age.

However, a relative age estimate can be obtained by comparing the position in the $T_{\rm eff}$–$\log N$(Li) diagram with that of stars with a well-defined age and similar APs. We therefore overplot the envelopes of clusters IC 2602, Pleiades, and Hyades (see, e.g., Soderblom et al. 1993a,b; Jeffries 2000), along with the locus of known members of the β Pictoris and Tucana-Horologium associations whose quoted ages are about 12 and 30 Myr, respectively (da Silva et al. 2009). As a result, most PMS-like stars are distributed similarly to the β Pictoris members and slightly above those of the Tucana-Horologium association (Fig. 5).

We got an alternative estimate of the ages of our targets by comparing their position in the HR diagram with pre-main-sequence isochrones from Siess et al. (2000), as shown in Fig. 6. Most PMS-like stars are located between the isochrones at 10 and 30 Myr, while six sources (#6 c2, #189, #191 c1 & c2, F3, F4) are found between the isochrones at 1 and 10 Myr (Fig. 6). This agrees with the young age assumed in Paper II. In contrast, the Pleiades-like stars are mostly below the isochrone at 30 Myr. We are finally able to confirm that all the PMS-like and Pleiades-like sources are likely young stars, with the exception of four sources (#109, #133, #159, #185 c1), which are likely lithium-rich sub-giant or giant stars (Figs. 3 and 6).

3.5. Calculation of spatial-kinematic coordinates

To study the kinematics of our targets in the $XYZUVW$ space, we combined the average radial velocities derived in Sect. 3.1 with the sky positions, proper motions, and parallaxes reported in *Gaia* DR2. For sources #15 and #101, we actually derived their kinematics by making use of the sky positions from the 2MASS catalog and the astrometry from the URAT Parallax Catalog. We then computed the Galactic positions (X,Y,Z) and heliocentric space-velocity components (U,V,W) in the left-handed coordinate system.[6] All these values are listed in Table 4.

As shown in Fig. 7, the (U,V) plane of targets with astrometry and RV measurement (Table 4) shows that most PMS-like and Pleiades-like stars are located in the young-disk (YD) population in the solar neighborhood, according to Eggen (1996). However we found three PMS-like (#35, #146, #185c1) and two Pleiades-like (#46, #109) in the region populated by old-disk stars. While the sources #109 and #185c1 are Li-rich giant stars, additional observations are needed to confirm any possible variation in radial velocities for the others. Our observations reveal that the sources #35, #46, #109 are possible SB2 systems due to a double-peaked Hα profile or their CCF shape (i.e., slightly asymmetric or with a possible small peak below our detection limit; Table 3). Regarding source #179, we do not exclude a problem in the wavelength calibration. From our RV value of -147.8 ± 0.8 km s^{-1}, this source might be located in the old-disk

[6] X and U are pointing towards the Galactic anti-center; Y and V in the Galactic rotation direction; Z and W towards the North Galactic pole.

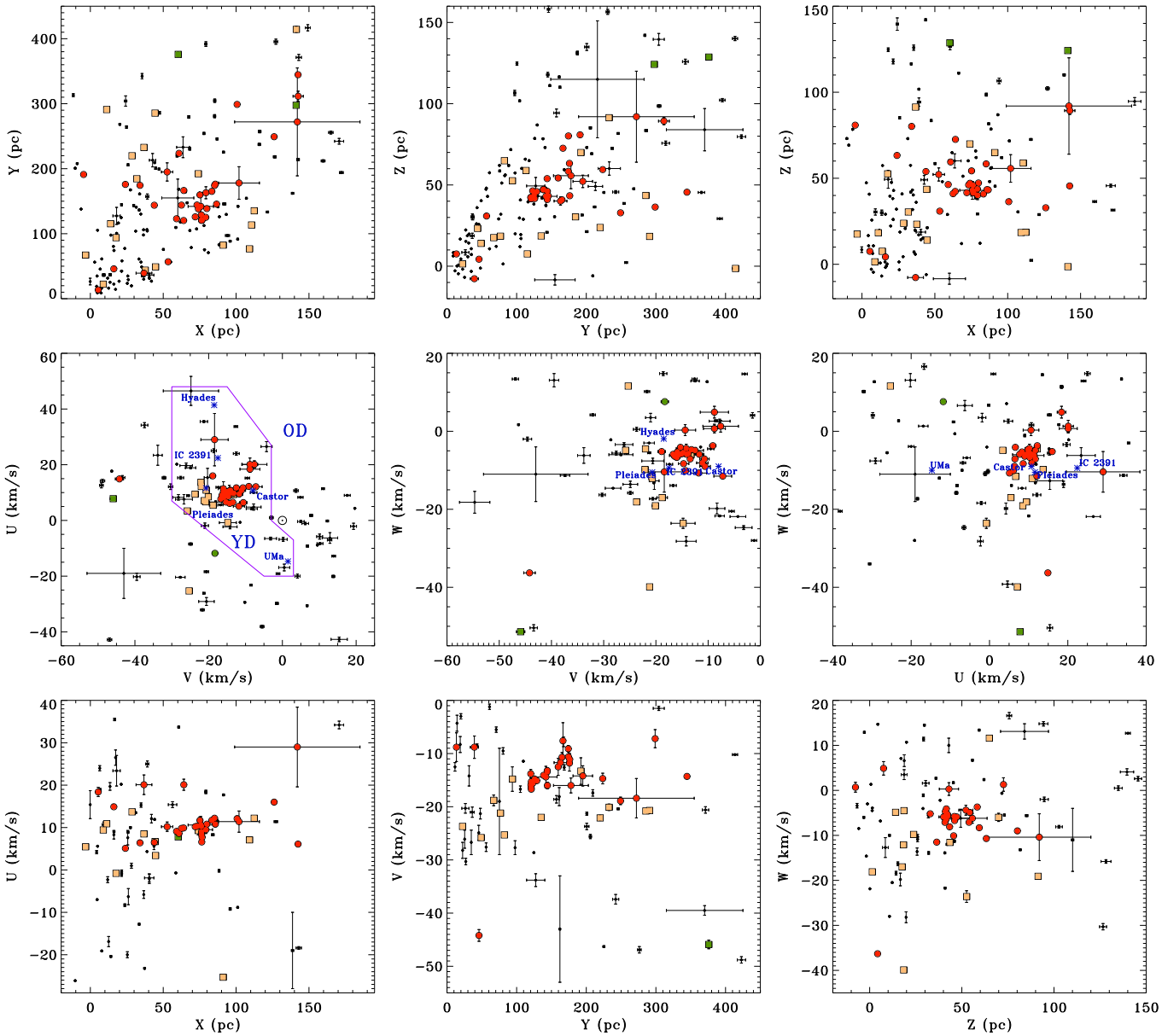


Fig. 8. Distribution of our targets in Galactic coordinates (*upper panels*) and space-velocity components (*middle panels*), along with the diagram of position versus velocity pointing in a given direction (*lower panels*). We restricted the parameter ranges on all diagrams to better see the distribution of the youngest sources. We use the same symbols as in Fig. 6. In the middle panels, we also display the mean position of the IC 2391 (∼50 Myr) and Hyades (∼600 Myr) superclusters, Pleiades (∼100 Myr) and Castor (∼200 Myr) moving groups, and Ursa Major (UMa) group (∼300 Myr). In the (U, V) plane, the solid line delimits the area of young- and old-disk populations in the solar neighborhood (Eggen 1996).

(OD) area. Thus this *RV* value must be used with care, especially because this source is not a high-proper-motion star and its *RV* value in *Gaia* DR2 is of -9.74 ± 2.88 km s^{-1}, which we use afterwards (Table 4). Finally, we note that the signal-to-noise of the spectrum acquired for source #146 is not high enough to obtain an accurate $W_{\rm Li}$ value.

Figure 8 shows the distribution of our targets in various 2D planes of the *XYZUVW* space restricting the parameter ranges to the locus of the young sources. We used the probabilistic approach described in Klutsch et al. (2014) to assess their membership to the five young stellar kinematic groups denoted in Fig. 8. Their ages are adopted from Table 1 of Montes et al. (2001). In the kinematic velocity space, the populations of PMS-like and Pleiades-like stars are located in well-distinguishable regions. On the one hand, the heliocentric space-velocity components of a compact group of PMS-like stars are marginally consistent with those of the Castor moving group. Nevertheless, such a link is hardly compatible because of the age difference between these two groups of young stars, but above all because the PMS-like stars are only weakly dispersed in the *XYZUVW* space. On the other hand, 75 % of the 12 Pleiades-like single stars with an *RV* value in Table 4 have membership probability to the Pleiades moving group larger than 40 %. These nine sources are #16, #22, #102, #112, #123, #125, #129, #151, and #179. Our procedure disregarded two sources (#31c2, #86) in the YD area due to a space-velocity component W lower than -23 km s^{-1}, along with source #46 located in the OD area (Fig. 7). These three sources probably exhibit some variation in radial velocity.

4. Discussion

4.1. Properties of the sample

Our study confirms that the multivariate analysis allows for the optimization of the disentangling of the stellar population from X-ray emitting extragalactic components. In fact, only one (#99) of the 162 sources is wrongly classified as a star due to a rather singular spatial configuration of the different sources (Fig. D.3) and the photometric properties of this galaxy that are similar to late M-type stars (Appendix D). The main stellar populations in our sample are young objects, multiple systems (Appendix B), and low-mass stars (Appendix C). This latter group includes 36 M-type dwarfs (i.e., from M0 to M4.5; see Table C.1).

We selected young stars more efficiently than in our previous works. This may be linked to a sampling of more distant sources in comparison to previous studies, as explained by the Gould Disk scenario (Guillout et al. 1998b). It could also be related to the sky region considered here in which stars younger than 30 Myr are found at three different distance scales: the visual binary V368 Cep and its comoving companion NLTT 56725 (~20 pc; Makarov et al. 2007), the Cepheus association (Table 6), and the Cepheus Flare region (Kun 2008; Kun et al. 2008).

We identified 59 lithium-rich sources. Most of them prove to be young but four sub-giant or giant stars also display a strong lithium line in absorption (Sect. 3.4). This is consistent with the discovery of several lithium-rich giants from our previous studies of the stellar X-ray population (Papers I and III). We classified 18 targets as Pleiades-like sources (age = 100–300 Myr) and 37 as PMS stars (age = 10–30 Myr). These two distinct stellar populations are found in different sky areas (Fig. 9). While the former are mainly located towards the Galactic plane, the latter are mostly projected in front of the CO Cepheus void, in the Cepheus Flare region.

During our survey of 186 sources, we identified 44 (24 %) spectroscopic multiple systems. This fraction is 30 % lower with respect to Papers I and III. Nine and six of them also display a strong and very strong lithium line (Table B.2), respectively. Using *Gaia* DR2 data, we found that 40 of our targets and six of eight young stars in Papers II and III have comoving companions with an angular separation ranging from a few arcsecond to a few arcmin (Table 5). Five of these visual binaries (#6, #18, #119, #131, G4) also have one component classified as an SB2 system. They are, therefore, likely hierarchical triple systems.

4.2. Young stars towards the CO Cepheus void

The possible detection of a new young association in Cepheus (age = 10–20 Myr; Paper II) is supported by our identification of 20 PMS stars (plus three small-separation companions observed during our spectroscopic campaigns) in the same region (Fig. 10) and our discovery of their eight comoving companions (Table 5). These are overplotted on the visible extinction $A_{V,RQ}$ map of Planck Collaboration et al. (2016),[7] derived from the thermal dust emission modeling presented by Draine & Li (2007). The PMS stars are highly clumped near the Galactic coordinates (X, Y, Z) = (76, 130, 43) pc (Fig. 8). To better see their distribution, we zoomed in this smaller region (Fig. 11).

[7] The map results from the renormalization of the visible extinction one based on the analysis of quasi-stellar objects observed in the Sloan Digital Sky Survey. This $A_{V,RQ}$ map is available from the *Planck* Legacy Archive (http://pla.esac.esa.int/pla/#home) and corresponds to the file: COM_CompMap_Dust-DL07-AvMaps_2048_R2.00.fits[AV_RQ].

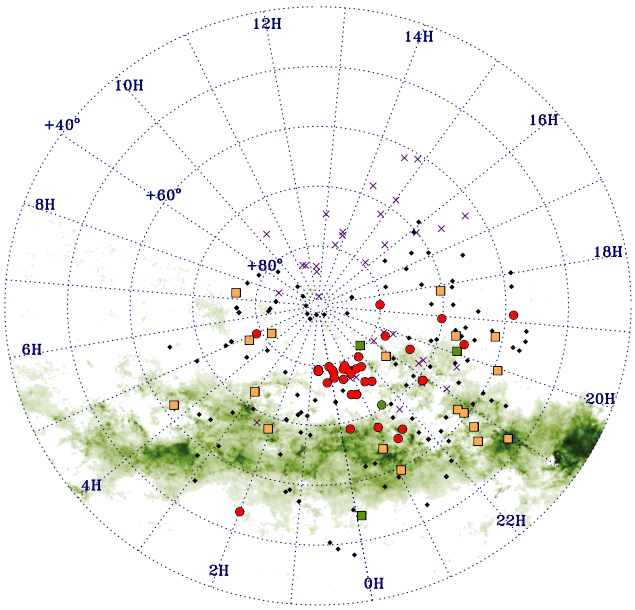


Fig. 9. Spatial distribution of our targets, overplotted on the extinction (A_v) map of Dobashi et al. (2005). In addition to the symbols defined in Fig. 6, we denote the unobserved sources with crosses.

Table 6. Properties of the three groups of PMS stars in Cepheus. We give for each group the number of targets and their multiplicity.

Parameter	Unit	Cep I	Cep II	Cep III
$\langle l \rangle$	[°]	122.31 ± 0.04	120.7 ± 2.0	118.7 ± 2.8
$\langle b \rangle$	[°]	16.31 ± 0.14	16.37 ± 0.33	15.7 ± 1.7
$\langle \mu_\alpha \cos\delta \rangle$	[mas yr^{-1}]	23.88 ± 0.29	22.63 ± 0.25	20.35 ± 0.34
$\langle \mu_\delta \rangle$	[mas yr^{-1}]	−3.11 ± 0.25	−0.31 ± 0.51	1.98 ± 0.49
$\langle RV \rangle$	[km s^{-1}]	−9.05 ± 0.24	−8.98 ± 0.3	−8.30 ± 0.43
$\langle \pi \rangle$	[mas]	6.713 ± 0.016	6.439 ± 0.054	6.044 ± 0.094
⟨Trigo. distance⟩	[pc]	148.97 ± 0.36	155.7 ± 1.3	167.7 ± 2.9
$\langle X \rangle$	[pc]	76.43 ± 0.19	76.0 ± 0.5	75.9 ± 1.0
$\langle Y \rangle$	[pc]	120.86 ± 0.29	128.5 ± 1.4	141.7 ± 2.7
$\langle Z \rangle$	[pc]	41.75 ± 0.13	43.9 ± 0.4	45.1 ± 0.8
$\langle U_\odot \rangle$	[km s^{-1}]	7.90 ± 0.29	9.15 ± 0.28	9.99 ± 0.33
$\langle V_\odot \rangle$	[km s^{-1}]	−16.08 ± 0.26	−15.54 ± 0.24	−14.02 ± 0.44
$\langle W_\odot \rangle$	[km s^{-1}]	−5.43 ± 0.26	−5.70 ± 0.15	−5.42 ± 0.27
Age	[Myr]	15 ± 5	15 ± 5	15 ± 5
Number of targets [sources] ‡		3 [7]	8 [14]	18 [29]
Fraction of systems		100 %	75 %	61 %
Number of single stars		0	2	7
Number of SB1 systems		0	1	2
Number of visual binaries		1	3	7
Number of multiple systems		2	2	2

Note. ‡ We give for each group the number of targets listed in Table 1, while that of resolved sources in the *Gaia* DR2 catalog (Tables 4 and 5) is bracketed.

Almost all PMS stars towards the CO Cepheus void are related to the Cepheus association (Fig. 10), except for sources #160 and #189 that are located at larger distances (354 ± 9 and 320 ± 97 pc, respectively). The former is a known member of the molecular cloud L1251 (see Sect. 3.3), while the astrometry of the latter suffers from large uncertainties. According to the 6D phase-space data of the remaining PMS stars in this restricted area, we can divide them into three subgroups, as explained below. We summarize their properties in Table 6.

We first identified the highest density of PMS stars in the projection of the sky positions (Fig. 10) and in the various planes in Galactic coordinates (Fig. 11). Up to now, this group (henceforth

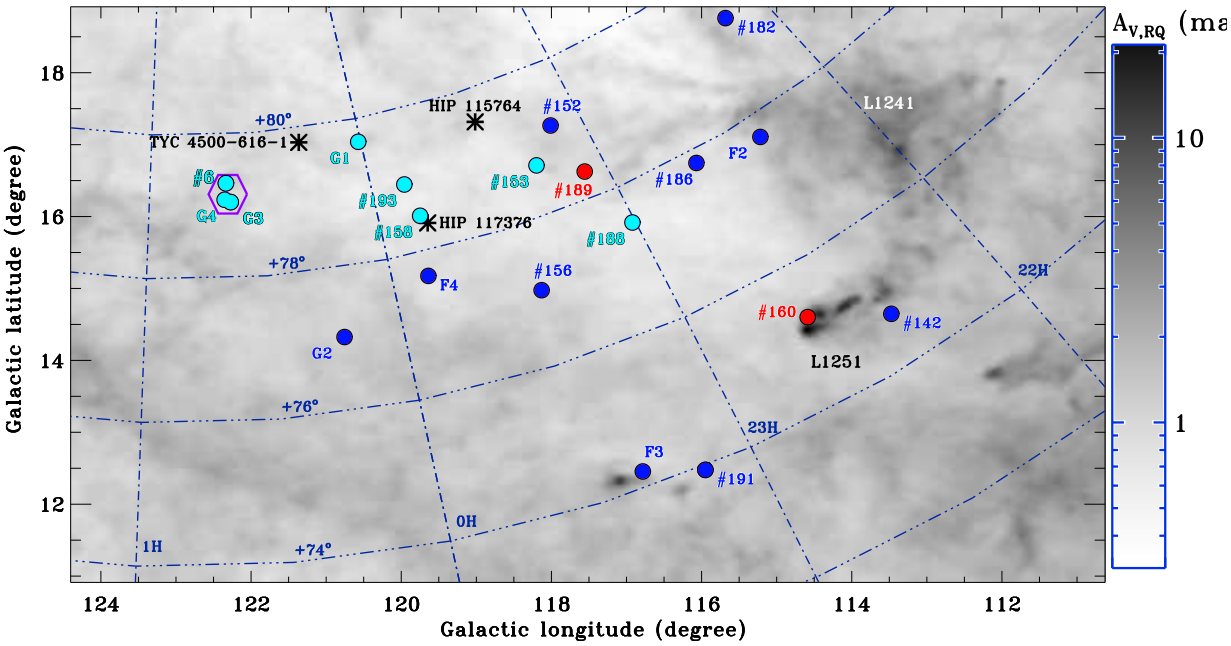


Fig. 10. Spatial distribution of the 20 PMS stars (circles) in the sky area towards the CO Cepheus void, overplotted on the visible extinction $A_{V,RQ}$ map of Planck Collaboration et al. (2016).[7] We display the Cep III members as blue circles and those still gravitationally bound (i.e., Cep II that is a subgroup of Cep III, see Sect. 4.2) as cyan circles, while the non-members are shown in red. The big hexagon encloses the Cep I members. The asterisks mark the locus of the three additional members reported in Oh et al. (2017) and Faherty et al. (2018), as described in Sect. 4.4.

Cep I) is composed of one visual binary (G3) and two triple hierarchical systems (#6 and G4). It is highlighted by a hexagon in Figs. 10 and 11. Moreover, source #6 has an additional wide-separation companion (Appendix B.2).

Five additional young sources with similar properties are located in a more extended area (henceforth Cep II; cyan circles in Figs. 10 and 11). In addition to the three Cep I members, this group includes two single stars (#158 and #193), one SB1 system (#153), and two visual binaries (#188 and G1).

Finally, the largest group (henceforth Cep III; blue circles in Figs. 10 and 11) is composed of five single stars (#142, #182, #186, F2, F4), one SB1 system (#156), four visual binaries (#152, #191, G2 and F3), and the Cep II members. The source F3 has also a wide-separation companion (Table 5).

4.3. Additional CO Cepheus void stars from Gaia

To see the extent of the association in Cepheus, we built a new sample that is hereinafter referred to as *Gaia*–2MASS. We selected all sources brighter than K_s = 12 mag from the PPMXL catalog (Roeser et al. 2010), using a cone search centered at (RA, DEC) = (0h, +77°) with a radius of 6°, which covers all the sky area devoid of interstellar matter. Subsequently we matched this dataset with *Gaia* DR2 (radius = 1″).

An asymmetry is clearly visible in the distribution of the proper motions in right ascension (middle panels of Fig. 12), in particular in the range of proper motions of the members of the Cepheus association (delimited by vertical lines). This results in an excess of sources with positive $\mu_\alpha \cos\delta$ values with respect to a normal symmetric distribution. The total number of the excess *Gaia*–2MASS sources is significantly larger than the number of young stars identified up to now in the CO Cepheus void. To search for a possible link between this excess of *Gaia*–2MASS stars and the Cepheus association, we performed a comparison with a simulation based on the Besançon model (Robin et al. 2012; Czekaj et al. 2014; Luri et al. 2014).

Due to the right ascension of the members of the Cepheus association ranging from 22h to 1h, we have to use a rectangular area covering Galactic longitude l ranging from 114° to 126° and Galactic latitude b from 8.°5 to 20.°5, together with the same cut in K_s magnitude that we had applied to build the *Gaia*–2MASS sample. This region slightly differs from the area covered by the selected *Gaia*–2MASS sources but both are consistent in terms of number of sources. The distributions of distance and proper motions are well reproduced by the simulation for both cases of the maximum distance threshold considered here (400 and 1000 pc; Fig. 12). Therefore, the asymmetry seen in the distribution of the $\mu_\alpha \cos\delta$ values is likely due to large-scale dynamical processes in the Galaxy rather than the result of the unknown supernova shock expected to be at the origin of the CO Cepheus void (Grenier et al. 1989). Thus, this excess alone cannot be used as a criterion to identify possible new members in this young association and a deeper analysis is required.

To this end, we compared the density map obtained from the *Gaia*-2MASS sources and the Besançon model (Fig. 13). While the (μ_δ, distance) diagram looks the same for the *Gaia*–2MASS distribution and the Besançon model, the ($\mu_\alpha \cos\delta$, distance) diagram reveals a clear over-density in the *Gaia*–2MASS sample (delimited by the polygonal shape). Coupled to the location of members of the Cepheus association on this density map (Fig. 14), it is indisputable that the excess *Gaia*–2MASS sources are attributable to the young stars in this region. These are the best member candidates to the Cepheus association to investigate with future observations.

4.4. Cepheus association and runaway stars

Klutsch (2008) discovered an excess of stellar X-ray sources in Cepheus where Tachihara et al. (2005), and Papers II and III had identified together 15 young stars belonging to the association.

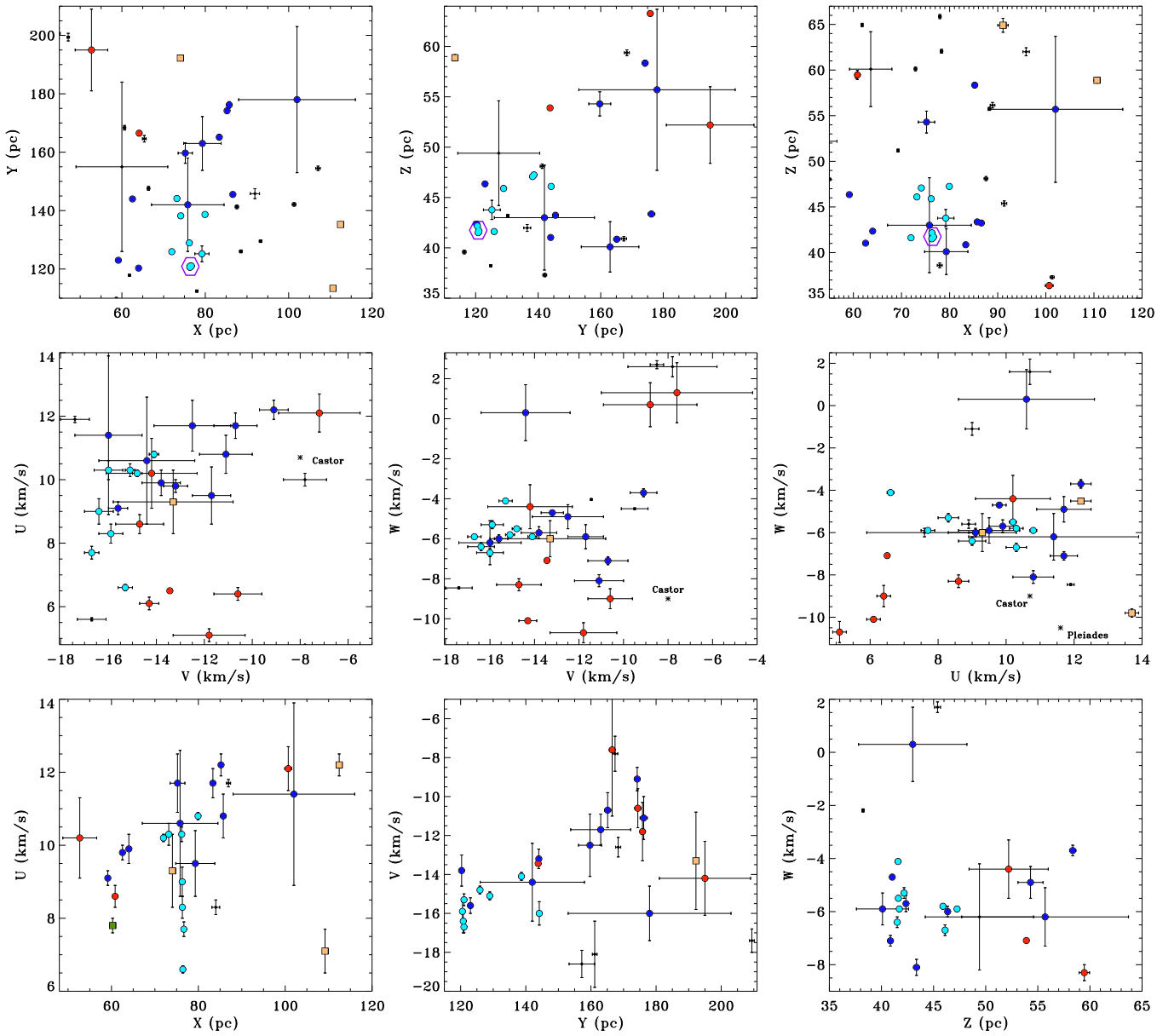


Fig. 11. Same diagrams as in Fig. 8 but covering only the region populated by the PMS-like stars towards the CO Cepheus void. In all the panels, we display the stars composing Cep III and its subgroup (i.e., Cep II) as blue and cyan circles, respectively. The red circles, the orange squares, and black diamonds correspond to the PMS-like that are non-members of Cep III, Pleiades-like stars, and older sources, respectively. In the upper panels, the big open hexagon marks the locus of the smaller concentration (i.e., Cep I).

The current study has added 14 new members (i.e., six PMS stars and eight comoving companions of these 21 young stars).

All but two PMS stars towards the CO Cepheus void have the same kinematic properties (Table 6) and therefore a common origin. We also found that eight of the young stars in Tachihara et al. (2005) belong to this association, confirming their assumption. The discovery of such a large number of young stars in this region is more easily explained by the in-situ model than by the runaway hypothesis. As mentioned by Tachihara et al. (2005) and Paper II, these sources are close to a faint, low density cloud that could be the remnant of the parent cloud already dissipated.

We see a decline in multiple systems and a shift from the mean Galactic position Y to positive values in the more scattered group (Cep III) with respect to the densest group (Cep I). This agrees with the dispersion of the cluster members driven by the rotation of the Galaxy. This also explains the gradient found in the ($\mu_\alpha \cos\delta$, distance) diagram (Fig. 14) because the members of the most extended stellar group tend to move further away from the others. Based on Table 6, the properties of the three stellar groups could be interpreted as follows: *i)* the strongest concentration of young stars (Cep I) could be the remnant of the past Cepheus cluster core, *ii)* the sources belonging to the group Cep II could correspond to the members that are still gravitationally bound, and *iii)* the most extended group (Cep III) denotes the original cluster. The latter corresponds to the Cepheus association reported in Paper II.

The group 38 of Oh et al. (2017) and Faherty et al. (2018) actually coincides with the Cepheus association analyzed here and lists three additional members (HIP 115764, HIP 117376,

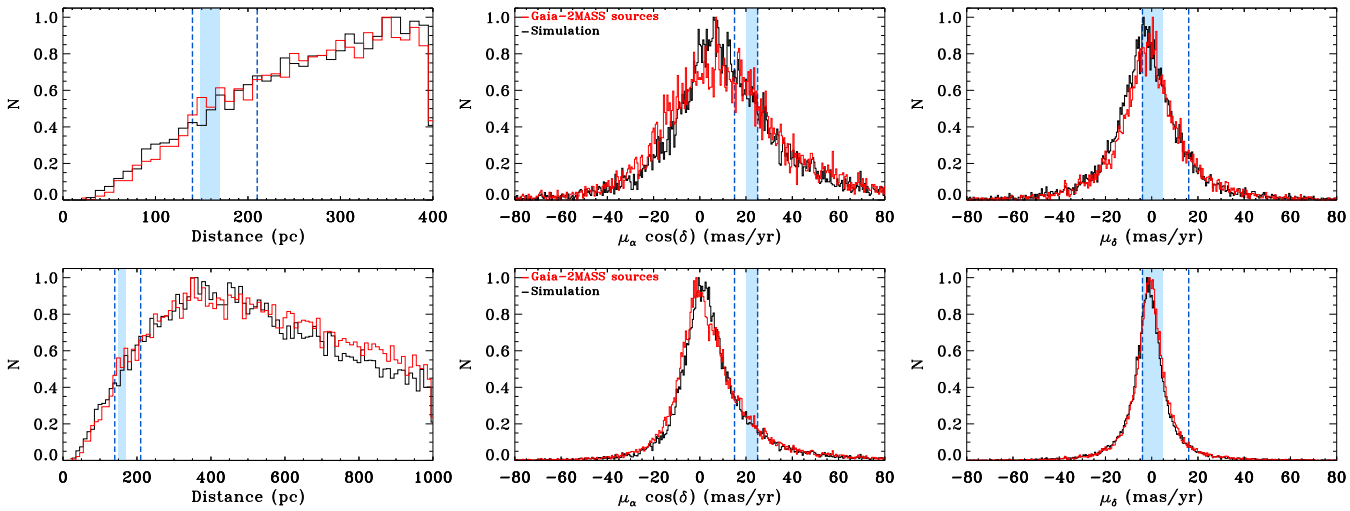


Fig. 12. Comparison of the distribution of distance (*left panels*), and proper motion in right ascension (*middle panels*) and in declination (*right panels*) between the *Gaia*-2MASS sources and the simulation with the Besançon model (Sect. 4.3). We normalized the number of stars in each bin, dividing by the maximum number of sources obtained for each histogram. For these plots, we only considered all the sources having a distance lower than 400 pc (*upper panels*) and 1000 pc (*lower panels*). In each panel, the blue-shaded area denotes the region populated by the likely members of Cep II, while the dashed lines correspond to those belonging to Cep III.

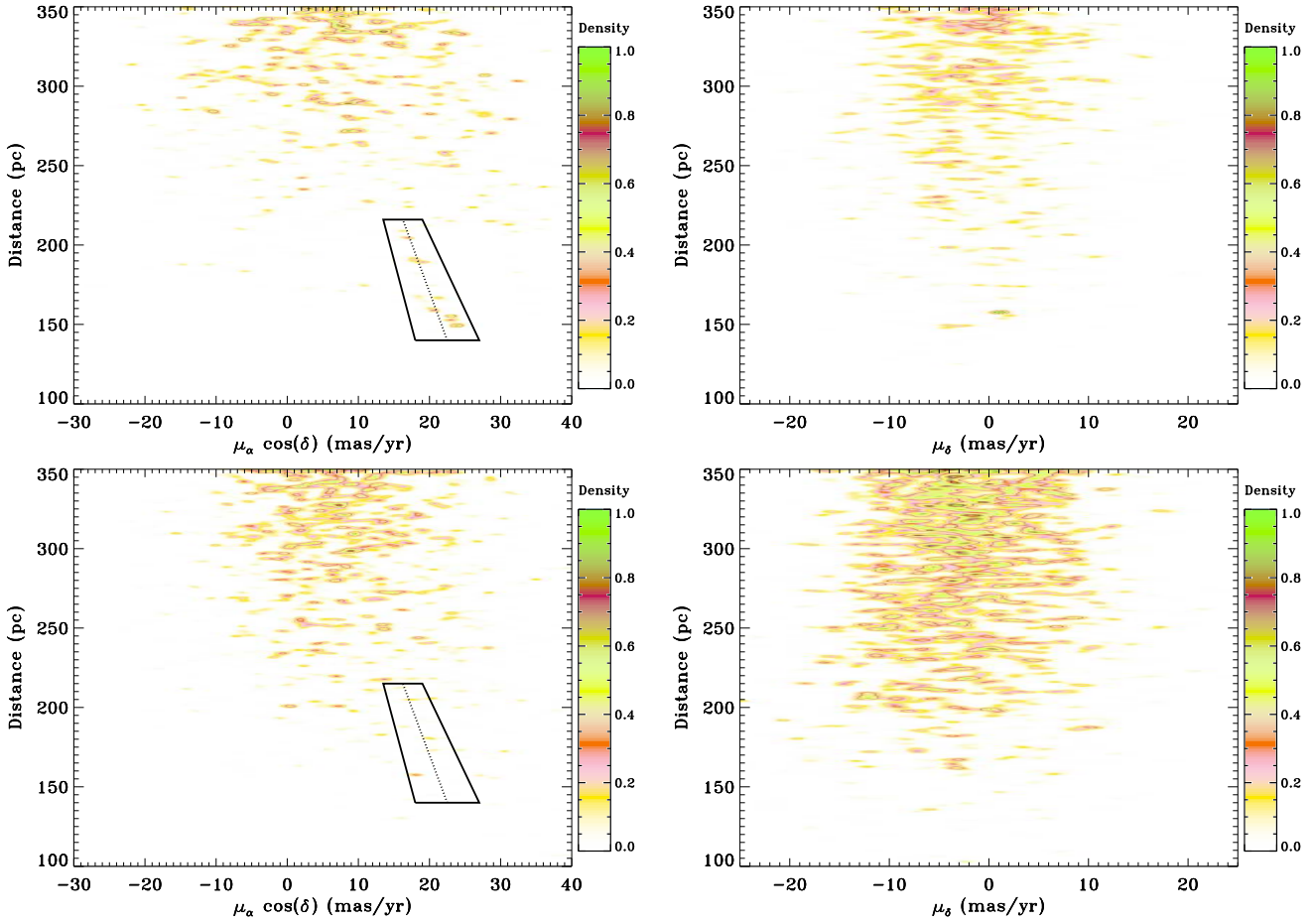


Fig. 13. Comparison of the density map obtained from the distribution of distance as a function of the proper motion in right ascension (*left panels*) and in declination (*right panels*), between the *Gaia*-2MASS sources (*upper panels*) and the simulation with the Besançon model (*lower panels*). In the left panels, the polygonal shape denotes the region populated by the PMS-like stars belonging to Cep III.

and TYC 4500-616-1). Their astrometries and the *RV* value of TYC 4500-616-1 in *Gaia* DR2 perfectly agree with those of the Cep II members (Fig. 14), while the *RV* value of HIP 117376 suggests a possible variation in radial velocity. The source

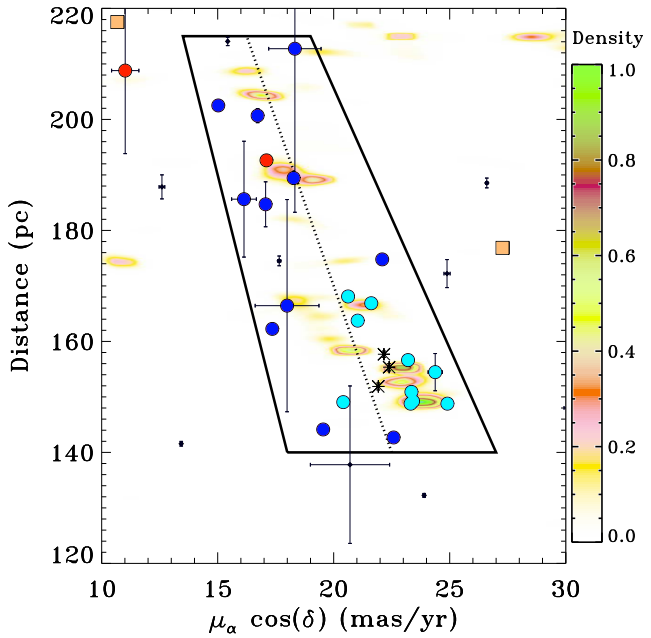


Fig. 14. ($\mu_\alpha \cos\delta$, distance) diagram of our young star candidates located in the region populated by the members of the Cepheus association, overplotted on the *Gaia*-2MASS density map (Fig. 13). We use the same symbols as in Fig. 11. The asterisks mark the locus of additional members reported by Oh et al. (2017) and Faherty et al. (2018): HIP 115764, HIP 117376, and TYC 4500-616-1 (from bottom to top).

HIP 115764 would be the warmest member of the association with an effective temperature of 8020^{+420}_{-140} K in *Gaia* DR2. We also note that the angular separation between HIP 117376 and our target #158 is about $8\farcs30 \pm 0.044$ mas. This brings the number of current bona fide members to 32.

We discovered six PMS stars outside the CO Cepheus void (#93, #106 c1, #115, #124, #150, and F1) with space-velocity components similar to the members of the Cepheus association. These correspond to the red circles in the (U, W) plane of Fig. 11. Their distances range from 160 to 240 pc, except for #150 (distance = 375 ± 3 pc). The five remaining sources (and their two comoving companions; Table 5) could be runaway stars. This list of sources includes one of the PMS stars from Paper III and one WTTS from Tachihara et al. (2005).

5. Conclusions

We present the results of a spectroscopic survey of optical counterparts of X-ray sources in the Cepheus region (near the North Celestial pole) aimed at discovering further young objects around the four comoving stars reported by us in Paper II. Based on multivariate analysis methods, we selected optical and infrared counterparts of ROSAT All-Sky Survey and XMM-Newton X-ray sources, which are young star candidates. The analysis of the spectra of these candidates allowed us to determine their atmospheric parameters, radial and rotational velocities, and atmospheric lithium content. These data, along with the parallaxes and proper motions from the *Gaia* DR2 catalog, were used to characterize our sample and identify new young stars in this region. The main stellar populations composing this sample are young or active stars and multiple systems. We identified two distinct populations of young stars that are spatially and kinematically separated. The 18 Pleiades-like objects with an age between 100 and 300 Myr are mostly projected towards the Galactic plane, while 23 of the 37 sources younger than 30 Myr are located in the sky area of 8 degree-diameter filling the CO Cepheus void. Among these, 21 PMS stars (including five spectroscopic binaries) and their eight comoving companions belong to the Cepheus association, which is the first nearby (distance = 157 ± 10 pc) young (age = 10–20 Myr) stellar association found northward of $\delta = +30°$.

We provide the first comprehensive view of the Cepheus association. All studies carried out so far in this sky region have found a total of 32 bona fide members and nine member candidates of this young association, to which 14 (44 %) members and six (67 %) candidates are new discoveries. The kinematics of its members reveals a substantial mixture of the original cluster within the local population of the Galactic plane. The runaway hypothesis is highly improbable for explaining the formation of this homogeneous stellar group because of their kinematic properties and the identification of several new members. This raises the question of the in-situ star-formation scenario in low-mass cloud environments (as in many other SFRs).

Coupled to the Cepheus association properties derived from the current analysis, our *Gaia*-2MASS sample should contribute to the identification of new candidates to be followed up in the future.

Acknowledgements. We thank the anonymous referee for useful suggestions. This work is supported by the Universidad Complutense de Madrid and Spanish *Ministerio de Ciencia e Innovación y Universidades* (MICINN) under grant AYA2016-79425-C3-1-P. A.K. and D.M. were also supported by AstroMadrid (CAM S2009/ESP-1496), and MICINN under grants AYA2008-00695 and AYA2008-06423-C03-03. Part of this study is also supported by the Italian *Ministero dell'Istruzione, Università e Ricerca* (MIUR), the French *Centre National d'Études spatiales* (CNES), and the *Région Alsace*. This research made use of the SIMBAD database, the VIZIER catalog access and the X-Match service, which are operated at the *Centre de Données astronomiques de Strasbourg* (CDS). This publication makes use of the data products from ROSAT and XMM-Newton X-ray observatories, the Two Micron All Sky Survey, and the European Space Agency (ESA) missions *Gaia* and *Planck*. The ROSAT All-Sky Survey catalogs were produced by the ROSAT Scientific Data Center at the Max-Planck-Institut für Extraterrestrische Physik (MPE), Garching (Germany). The 2XMMi-DR3 catalog is the fifth publicly released XMM-Newton X-ray source catalog produced by the XMM-Newton Survey Science Centre (SSC) consortium on behalf of ESA. The 2XMMi-DR3 is one of two incremental versions of the 2XMM catalog. The Two Micron All Sky Survey, which is a joint project of the University of Massachusetts and the Infrared Processing and Analysis Center/California Institute of Technology, was funded by the National Aeronautics and Space Administration and the National Science Foundation. The data from the ESA mission *Gaia* (`https://www.cosmos.esa.int/gaia`) was processed by the *Gaia* Data Processing and Analysis Consortium (DPAC, `https://www.cosmos.esa.int/web/gaia/dpac/consortium`). Funding for the DPAC has been provided by national institutions, in particular the institutions participating in the *Gaia* Multilateral Agreement. *Planck* (http://www.esa.int/Planck) is an ESA science mission with instruments and contributions directly funded by ESA Member States, NASA, and Canada. This publication used the POLLUX database (http://pollux.graal.univ-montp2.fr) operated at LUPM (*Laboratoire Univers et Particules de Montpellier*, Université Montpellier II – CNRS, France) with the support of the French *Programme National de Physique Stellaire* and *Institut national des sciences de l'Univers*.

References

Abt, H. A. 2008, ApJS, 176, 216
Abt, H. A. & Willmarth, D. 2006, ApJS, 162, 207
Alcala, J. M., Krautter, J., Covino, E., et al. 1997, A&A, 319, 184
Alonso-Floriano, F. J., Morales, J. C., Caballero, J. A., et al. 2015, A&A, 577, A128
Barden, S. C. 1985, ApJ, 295, 162
Bertout, C., Siess, L., & Cabrit, S. 2007, A&A, 473, L21
Bessell, M. S. & Brett, J. M. 1988, PASP, 100, 1134
Bouchy, F., Hébrard, G., Udry, S., et al. 2009, A&A, 505, 853
Bouvier, J., Barrado, D., Moraux, E., et al. 2018, A&A, 613, A63

Bruntt, H., Bedding, T. R., Quirion, P.-O., et al. 2010, MNRAS, 405, 1907
Caballero, J. A., Cortés-Contreras, M., Alonso-Floriano, F. J., et al. 2013, in Protostars and Planets VI Posters, 20
Carpenter, J. M. 2001, AJ, 121, 2851
Casagrande, L., Ramírez, I., Meléndez, J., Bessell, M., & Asplund, M. 2010, A&A, 512, A54
Casagrande, L., Schönrich, R., Asplund, M., et al. 2011, A&A, 530, A138
Cowley, A. P. & Bidelman, W. P. 1979, PASP, 91, 83
Cutri, R. M., Wright, E. L., Conrow, T., et al. 2012, Explanatory Supplement to the WISE All-Sky Data Release Products, Tech. rep.
Czekaj, M. A., Robin, A. C., Figueras, F., Luri, X., & Haywood, M. 2014, A&A, 564, A102
da Silva, L., Torres, C. A. O., de La Reza, R., et al. 2009, A&A, 508, 833
da Silva, R., Milone, A. C., & Reddy, B. E. 2011, A&A, 526, A71
Daemgen, S., Siegler, N., Reid, I. N., & Close, L. M. 2007, ApJ, 654, 558
Dame, T. M., Hartmann, D., & Thaddeus, P. 2001, ApJ, 547, 792
Delfosse, X., Forveille, T., Perrier, C., & Mayor, M. 1998, A&A, 331, 581
Dobashi, K., Uehara, H., Kandori, R., et al. 2005, PASJ, 57, 1
Draine, B. T. & Li, A. 2007, ApJ, 657, 810
Droege, T. F., Richmond, M. W., Sallman, M. P., & Creager, R. P. 2006, PASP, 118, 1666
Eggen, O. J. 1996, AJ, 112, 1595
ESA, ed. 1997, ESA Special Publication, Vol. 1200, The HIPPARCOS and TYCHO catalogues. Astrometric and photometric star catalogues derived from the ESA HIPPARCOS Space Astrometry Mission
Faherty, J. K., Bochanski, J. J., Gagné, J., et al. 2018, ApJ, 863, 91
Famaey, B., Jorissen, A., Luri, X., et al. 2005, A&A, 430, 165
Feigelson, E. D. 1996, ApJ, 468, 306
Finch, C. T. & Zacharias, N. 2016, VizieR Online Data Catalog, 1333
Fischer, D. A. & Valenti, J. 2005, ApJ, 622, 1102
Fleming, T. A., Liebert, J., Gioia, I. M., & Maccacaro, T. 1988, ApJ, 331, 958
Flesch, E. 2010, PASA, 27, 283 (VizieR Online Data Catalog: V/134)
Frasca, A., Biazzo, K., Lanzafame, A. C., et al. 2015, A&A, 575, A4
Frasca, A. & Catalano, S. 1994, A&A, 284, 883
Frasca, A., Catalano, S., & Mantovani, D. 1997, A&A, 320, 101
Frasca, A., Covino, E., Spezzi, L., et al. 2009, A&A, 508, 1313
Frasca, A., Freire Ferrero, R., Marilli, E., & Catalano, S. 2000, A&A, 364, 179
Frasca, A., Guillout, P., Klutsch, A., et al. 2018, A&A, 612, A96
Frasca, A., Guillout, P., Marilli, E., et al. 2006, A&A, 454, 301
Fuhrmann, K. 2008, MNRAS, 384, 173
Gagné, J. & Faherty, J. K. 2018, ApJ, 862, 138
Gagné, J., Faherty, J. K., Cruz, K. L., et al. 2015a, ApJS, 219, 33
Gagné, J., Lafrenière, D., Doyon, R., Malo, L., & Artigau, É. 2014, ApJ, 783, 121
Gagné, J., Lafrenière, D., Doyon, R., Malo, L., & Artigau, É. 2015b, ApJ, 798, 73
Gagné, J., Mamajek, E. E., Malo, L., et al. 2018a, ApJ, 856, 23
Gagné, J., Roy-Loubier, O., Faherty, J. K., Doyon, R., & Malo, L. 2018b, ApJ, 860, 43
Gaia Collaboration, Brown, A. G. A., Vallenari, A., et al. 2018, A&A, 616, A1
Gaia Collaboration, Prusti, T., de Bruijne, J. H. J., et al. 2016, A&A, 595, A1
Gigoyan, K. S. & Mickaelian, A. M. 2012, MNRAS, 419, 3346
Gilmore, G., Randich, S., Asplund, M., et al. 2012, The Messenger, 147, 25
Girardi, L., Bressan, A., Bertelli, G., & Chiosi, C. 2000, A&AS, 141, 371
Glebocki, R. & Gnacinski, P. 2005, VizieR Online Data Catalog: III/244
Gontcharov, G. A. 2006, Astronomy Letters, 32, 759
Gonzalez, G., Carlson, M. K., & Tobin, R. W. 2010, MNRAS, 403, 1368
Gorbikov, E. & Brosch, N. 2014, MNRAS, 443, 725
Gorti, U. & Bhatt, H. C. 1996, MNRAS, 278, 611
Gray, R. O., Corbally, C. J., Garrison, R. F., et al. 2006, AJ, 132, 161
Gray, R. O., Corbally, C. J., Garrison, R. F., McFadden, M. T., & Robinson, P. E. 2003, AJ, 126, 2048
Gray, R. O., Napier, M. G., & Winkler, L. I. 2001, AJ, 121, 2148
Grenier, I. A., Lebrun, F., Arnaud, M., Dame, T. M., & Thaddeus, P. 1989, ApJ, 347, 231
Guillout, P., Frasca, A., Klutsch, A., Marilli, E., & Montes, D. 2010, A&A, 520, A94
Guillout, P., Klutsch, A., Frasca, A., et al. 2009, A&A, 504, 829
Guillout, P., Schmitt, J. H. M. M., Egret, D., et al. 1999, A&A, 351, 1003
Guillout, P., Sterzik, M. F., Schmitt, J. H. M. M., et al. 1998a, A&A, 334, 540
Guillout, P., Sterzik, M. F., Schmitt, J. H. M. M., Motch, C., & Neuhaeuser, R. 1998b, A&A, 337, 113
Harlan, E. A. 1969, AJ, 74, 916
Hauschildt, P. H., Allard, F., & Baron, E. 1999, ApJ, 512, 377
Hekker, S. & Meléndez, J. 2007, A&A, 475, 1003
Henden, A. A., Levine, S., Terrell, D., & Welch, D. L. 2015, in American Astronomical Society Meeting Abstracts, Vol. 225, American Astronomical Society Meeting Abstracts #225, 336.16
Herbig, G. H. 1985, ApJ, 289, 269
Herrero, E., Ribas, I., Jordi, C., Guinan, E. F., & Engle, S. G. 2012, A&A, 537, A147
Høg, E., Fabricius, C., Makarov, V. V., et al. 2000, A&A, 355, L27
Houdebine, E. R. 2010, MNRAS, 407, 1657
Houdebine, E. R. 2011, MNRAS, 416, 2233
Janson, M., Hormuth, F., Bergfors, C., et al. 2012, ApJ, 754, 44
Jeffers, S. V., Schöfer, P., Lamert, A., et al. 2018, A&A, 614, A76
Jeffries, R. D. 2000, in Astronomical Society of the Pacific Conference Series, Vol. 198, Stellar Clusters and Associations: Convection, Rotation, and Dynamos, ed. R. Pallavicini, G. Micela, & S. Sciortino, 245
Jeffries, R. D. 2017, Mem. Soc. Astron. Italiana, 88, 637
Jeffries, R. D., Jackson, R. J., Cottaar, M., et al. 2014, A&A, 563, A94
Jenkins, J. S., Ramsey, L. W., Jones, H. R. A., et al. 2009, ApJ, 704, 975
Jiménez-Esteban, F. M., Caballero, J. A., Dorda, R., Miles-Páez, P. A., & Solano, E. 2012, A&A, 539, A86
Kharchenko, N. V., Scholz, R.-D., Piskunov, A. E., Röser, S., & Schilbach, E. 2007, Astronomische Nachrichten, 328, 889
Kiss, Z. T., Tóth, L. V., Krause, O., Kun, M., & Stickel, M. 2006, A&A, 453, 923
Klutsch, A. 2008, PhD thesis, Observatoire de Strasbourg, Universié Louis Pasteur
Klutsch, A., Alonso-Floriano, F. J., Caballero, J. A., et al. 2012, in SF2A-2012: Proceedings of the Annual meeting of the French Society of Astronomy and Astrophysics, ed. S. Boissier, P. de Laverny, N. Nardetto, R. Samadi, D. Valls-Gabaud, & H. Wozniak, 357–360
Klutsch, A., Frasca, A., Guillout, P., et al. 2008, A&A, 490, 737
Klutsch, A., Freire Ferrero, R., Guillout, P., et al. 2014, A&A, 567, A52
Kun, M. 2008, in Handbook of Star Forming Regions, Volume I, ed. Reipurth, B. (Astronomical Society of the Pacific Monograph Publications), 240
Kun, M., Balog, Z., Kenyon, S. J., Mamajek, E. E., & Gutermuth, R. A. 2009, ApJS, 185, 451
Kun, M., Kiss, Z. T., & Balog, Z. 2008, in Handbook of Star Forming Regions, Volume I, ed. Reipurth, B. (Astronomical Society of the Pacific Monograph Publications), 136
Kun, M. & Prusti, T. 1993, A&A, 272, 235
Lasker, B. M., Lattanzi, M. G., McLean, B. J., et al. 2008, AJ, 136, 735 (VizieR Online Data Catalog: I/305)
Lee, S.-G. 1984, AJ, 89, 702
Lépine, S., Hilton, E. J., Mann, A. W., et al. 2013, AJ, 145, 102
Lépine, S. & Shara, M. M. 2005, AJ, 129, 1483
Luri, X., Palmer, M., Arenou, F., et al. 2014, A&A, 566, A119
Makarov, V. V., Zacharias, N., Hennessy, G. S., Harris, H. C., & Monet, A. K. B. 2007, ApJ, 668, L155
Malo, L., Doyon, R., Lafrenière, D., et al. 2013, ApJ, 762, 88
Mapelli, M., Vallenari, A., Jeffries, R. D., et al. 2015, A&A, 578, A35
McCarthy, K. & Wilhelm, R. J. 2014, AJ, 148, 70
Meléndez, J., Asplund, M., Alves-Brito, A., et al. 2008, A&A, 484, L21
Mishenina, T. V., Soubiran, C., Bienaymé, O., et al. 2008, A&A, 489, 923
Monet, D. G., Levine, S. E., Canzian, B., et al. 2003, AJ, 125, 984
Montes, D., Fernandez-Figueroa, M. J., de Castro, E., & Cornide, M. 1995, A&AS, 109, 135
Montes, D., López-Santiago, J., Gálvez, M. C., et al. 2001, MNRAS, 328, 45
Moór, A., Pascucci, I., Kóspál, Á., et al. 2011, ApJS, 193, 4
Motch, C., Guillout, P., Haberl, F., et al. 1998, A&AS, 132, 341
Motch, C., Guillout, P., Haberl, F., et al. 1997a, A&AS, 122, 201
Motch, C., Haberl, F., Dennerl, K., Pakull, M., & Janot-Pacheco, E. 1997b, A&A, 323, 853
Moultaka, J., Ilovaisky, S. A., Prugniel, P., & Soubiran, C. 2004, PASP, 116, 693
Nidever, D. L., Marcy, G. W., Butler, R. P., Fischer, D. A., & Vogt, S. S. 2002, ApJS, 141, 503
Nissen, P. E. & Schuster, W. J. 2010, A&A, 511, L10
Oh, S., Price-Whelan, A. M., Hogg, D. W., Morton, T. D., & Spergel, D. N. 2017, AJ, 153, 257
Palacios, A., Gebran, M., Josselin, E., et al. 2010, A&A, 516, A13
Pavlenko, Y. V. & Magazzu, A. 1996, A&A, 311, 961
Perruchot, S., Kohler, D., Bouchy, F., et al. 2008, in Presented at the Society of Photo-Optical Instrumentation Engineers (SPIE) Conference, Vol. 7014, Society of Photo-Optical Instrumentation Engineers (SPIE) Conference Series
Pfeiffer, M. J., Frank, C., Baumueller, D., Fuhrmann, K., & Gehren, T. 1998, A&AS, 130, 381
Pineau, F.-X. 2009, PhD thesis, Observatoire de Strasbourg, Universié de Strasbourg
Pineau, F.-X., Derriere, S., Michel, L., & Motch, C. 2008a, in Astronomical Society of the Pacific Conference Series, Vol. 394, Astronomical Data Analysis Software and Systems XVII, ed. R. W. Argyle, P. S. Bunclark, & J. R. Lewis, 369
Pineau, F.-X., Derriere, S., Michel, L., & Motch, C. 2008b, in American Institute of Physics Conference Series, Vol. 1082, American Institute of Physics Conference Series, ed. C. A. L. Bailer-Jones, 15–21
Pineau, F.-X., Motch, C., Carrera, F., et al. 2011, A&A, 527, A126

Piskunov, A. E., Kharchenko, N. V., Schilbach, E., et al. 2008, A&A, 487, 557
Planck Collaboration, Ade, P. A. R., Aghanim, N., et al. 2016, A&A, 586, A132
Preibisch, T., Kim, Y.-C., Favata, F., et al. 2005, ApJS, 160, 401
Ramírez, I., Allende Prieto, C., & Lambert, D. L. 2007, A&A, 465, 271
Randich, S., Gilmore, G., & Gaia-ESO Consortium. 2013, The Messenger, 154, 47
Reddy, B. E. & Lambert, D. L. 2008, MNRAS, 391, 95
Robin, A. C., Luri, X., Reylé, C., et al. 2012, A&A, 543, A100
Roeser, S., Demleitner, M., & Schilbach, E. 2010, AJ, 139, 2440
Sacco, G. G., Jeffries, R. D., Randich, S., et al. 2015, A&A, 574, L7
Shkolnik, E., Liu, M. C., & Reid, I. N. 2009, ApJ, 699, 649
Shkolnik, E. L., Hebb, L., Liu, M. C., Reid, I. N., & Collier Cameron, A. 2010, ApJ, 716, 1522
Siess, L., Dufour, E., & Forestini, M. 2000, A&A, 358, 593
Simon, T. 2006, AJ, 131, 501
Simon, T. 2009, ApJ, 694, 425
Skiff, B. A. 2010, VizieR Online Data Catalog: B/mk/mktypes
Skrutskie, M. F., Cutri, R. M., Stiening, R., et al. 2006, AJ, 131, 1163 (VizieR Online Data Catalog: II/246)
Skrutskie, M. F., Cutri, R. M., Stiening, R., et al. 2003, VizieR Online Data Catalog: VII/233
Soderblom, D. R., Fedele, S. B., Jones, B. F., Stauffer, J. R., & Prosser, C. F. 1993a, AJ, 106, 1080
Soderblom, D. R., Jones, B. F., Balachandran, S., et al. 1993b, AJ, 106, 1059
Soderblom, D. R., King, J. R., & Henry, T. J. 1998, AJ, 116, 396
Soubiran, C., Jasniewicz, G., Chemin, L., et al. 2013, A&A, 552, A64
Soubiran, C., Jasniewicz, G., Chemin, L., et al. 2018, A&A, 616, A7
Soubiran, C., Katz, D., & Cayrel, R. 1998, A&AS, 133, 221
Soubiran, C., Le Campion, J.-F., Cayrel de Strobel, G., & Caillo, A. 2010, A&A, 515, A111 (VizieR Online Data Catalog: B/pastel/pastel)
Stassun, K. G., Oelkers, R. J., Pepper, J., et al. 2018, AJ, 156, 102
Stephenson, C. B. 1986, AJ, 91, 144
Sterzik, M. F., Alcala, J. M., Neuhaeuser, R., & Schmitt, J. H. M. M. 1995, A&A, 297, 418
Sterzik, M. F. & Durisen, R. H. 1995, A&A, 304, L9
Sterzik, M. F. & Durisen, R. H. 1998, A&A, 339, 95
Tachihara, K., Neuhäuser, R., Kun, M., & Fukui, Y. 2005, A&A, 437, 919
Tonry, J. & Davis, M. 1979, AJ, 84, 1511
Torres, C. A. O., Quast, G. R., da Silva, L., et al. 2006, A&A, 460, 695
Torres, C. A. O., Quast, G. R., Melo, C. H. F., & Sterzik, M. F. 2008, in Handbook of Star Forming Regions, Volume II, ed. Reipurth, B. (Astronomical Society of the Pacific Monograph Publications), 757
Valenti, J. A. & Fischer, D. A. 2005, ApJS, 159, 141
Voges, W., Aschenbach, B., Boller, T., et al. 1999, A&A, 349, 389 (VizieR Online Data Catalog: IX/10A)
Voges, W., Aschenbach, B., Boller, T., et al. 2000, IAU Circ., 7432, 3 (VizieR Online Data Catalog: IX/29)
Vyssotsky, A. N. 1956, AJ, 61, 201
Wang, S. & Chen, X. 2019, ApJ, 877, 116
Watson, M. G., Schröder, A. C., Fyfe, D., et al. 2009, A&A, 493, 339 (VizieR Online Data Catalog: IX/41)
West, A. A., Hawley, S. L., Bochanski, J. J., et al. 2008, AJ, 135, 785
Woolf, V. M. & Wallerstein, G. 2005, MNRAS, 356, 963
Wright, E. L., Eisenhardt, P. R. M., Mainzer, A. K., et al. 2010, AJ, 140, 1868
Zacharias, N., Finch, C., Subasavage, J., et al. 2015, AJ, 150, 101
Zacharias, N., Monet, D. G., Levine, S. E., et al. 2004, in Bulletin of the American Astronomical Society, Vol. 36, American Astronomical Society Meeting Abstracts, 1418
Zapatero Osorio, M. R., Béjar, V. J. S., Pavlenko, Y., et al. 2002, A&A, 384, 937
Zinnecker, H. 2008, in Workshop on Star Formation Across the Milky Way Galaxy (ESO)
Zuckerman, B., Rhee, J. H., Song, I., & Bessell, M. S. 2011, ApJ, 732, 61
Zuckerman, B. & Song, I. 2004, ARA&A, 42, 685

Appendix A: Extraction of spectra of binary-pair candidates with a double Gaussian profile

To benefit from the IDS instrumental setup, we sought to identify possible binary-pair candidates within our target list before starting our observing runs. However, during the observations themselves, we found additional likely visual binaries having a lower angular separation. We did not identify them previously because the resolution of public images is not enough to resolve such binaries with sufficient confidence, before the launch of *Gaia* observatory. In such cases, we oriented the slit with the position angle of the two components to simultaneously image them. Hereafter, we illustrate this work on the source #40 (= 1RXS J061946.4+771933) because the alignment of three sources allows us to validate our work process.

The source 2MASS J06194548+7719330 seems to have a weakly-elongated shape with respect to that of nearby stars (Fig. A.1), which is typical of unresolved binaries and sources with a low angular separation. During our observing runs because we actually saw two sources close to the coordinates of our candidate. These turn out to be comoving stars (Table 5). To position the slit on these two objects, we then set the slit position angle to about 114°. Based on the *Gaia* DR2 coordinates, this angle is rather similar to the position angle θ of 115.°13 ± 24.″35 between these two sources, and of 114.°44 ± 2.″95 between the source #40 and 2MASS J06195324+7719222. On the cuts perpendicular to the spectral direction, the aperture of the three components are clearly visible, regardless of the line used, even if the apertures C1 and C2 are partially blended (Fig. A.2).

We firstly used the procedure of extraction within the `IRAF` environment, `APALL`. As the spectrum obtained from the second aperture (C2) was contaminated by the light of the bright source (C1), we needed to perform an extraction by means of a double Gaussian profile in order to accurately fit each trace and thus substantially reduce such a contamination. In this context, we adapted the code of Frasca et al. (1997) to the IDS data. As the 235 mm camera optics severely vignettes the outer regions of the dispersed light beam, only 2070 of the CCD pixels are useful for the H1800V dispersion grating (Fig. A.3). We determined the shape of each aperture by fitting all the perpendicular cuts along the spectral direction of clear and unvignetted lines. We extracted the two spectra from the partially blended apertures C1 and C2 using a double Gaussian profile, while we fitted the third aperture (C3) with an additional simple Gaussian profile. The traces for the three sources are displayed on Fig. A.4.

Using the 2MASS, NOMAD, and WISE coordinates, we found a spatial scale of 0.42–0.43 arcsec/pixel. This agrees with the value of 0.44 arcsec/pixel tabulated for this detector. From the clear and unvignetted lines, we found an average gap of 5.8±0.1 and 65.0±0.1 pixels between the main aperture (C1) and the two others (C2 and C3, respectively). These correspond to an angular separation ρ of 2.″49 ± 0.″07 and 28.″0 ± 0.″4. These are consistent with the angular separation derived from the 2MASS coordinates ($\rho_{C_1-C_3}$ = 27.″707 ± 0.″079) and the *Gaia* DR2 ones ($\rho_{C_1-C_2}$ = 2.″52 ± 0.032 mas and $\rho_{C_1-C_3}$ = 28.″39 ± 0.040 mas).

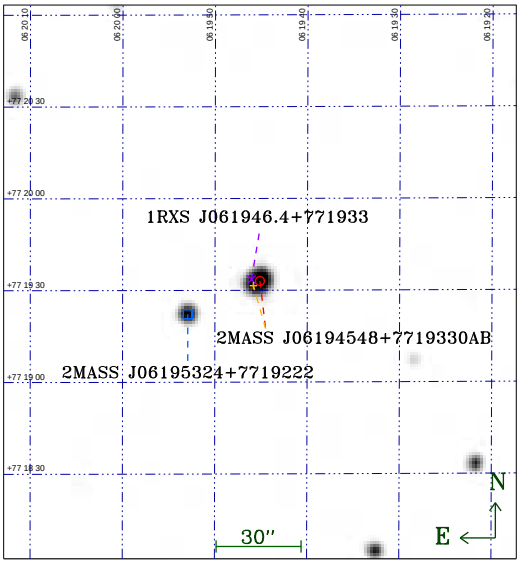


Fig. A.1. 2MASS K_s-band image (Epoch J1999.10), centered on the source 2MASS J06194548+7719330 (circle) and its nearest companion *Gaia* DR2 1116789735748819968 ("plus" symbol). We also show the positions of the X-ray source 1RXS J061946.4+771933 (cross) and the source 2MASS J06195324+7719222 (square).

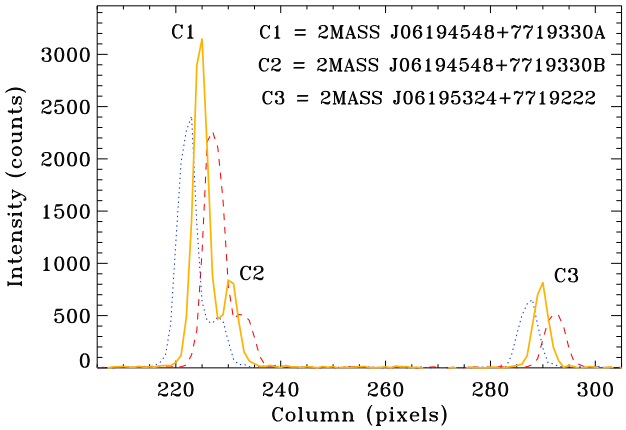


Fig. A.2. Plot of the line numbers 1300 (red dashed line), 2000 (orange solid line), and 2700 (blue dotted line), perpendicular to the spectral direction. The three apertures C1–C3 are clearly visible.

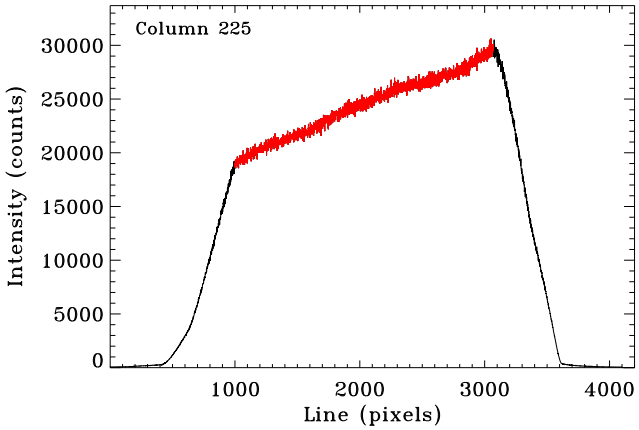


Fig. A.3. Plot of a lamp flat on the 235 mm camera with the 2k×4k RED+2 CCD detector mounted on IDS. The portion in red corresponds to the approximately 2070 CCD pixels that are clear and unvignetted.

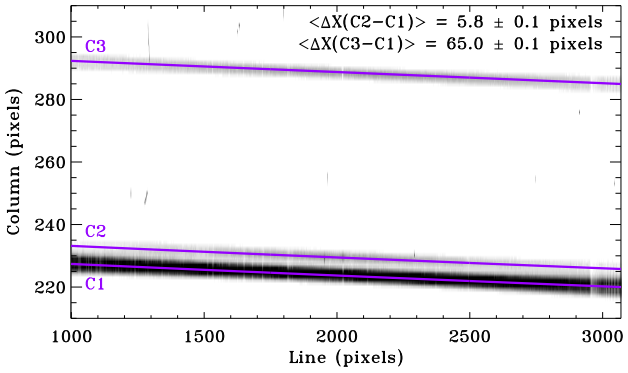


Fig. A.4. Zoom on the section of the image where the traces of the three sources can be used for a spectral analysis. This corresponds to all the clear and unvignetted lines (Fig. A.3) and columns from 205 to 305. We also overplotted the trace (solid lines) obtained for each of the three sources. On the right upper corner, we indicate the mean separation between the main aperture (C1) and the two others (C2 and C3).

Appendix B: Multiple systems

The main goal of this analysis is to identify all the members of the Cepheus association among our targets and to derive the maximum information about their physical and kinematic properties. This includes their multiplicity on both small (i.e., spectroscopic systems or visual binaries with small angular separation) and large (i.e., common proper-motion binaries) scales.

Appendix B.1: Binary-pair candidates

During our observing runs with the IDS spectrograph, it has happened that two sources are located at the coordinates of our targets. To be sure to observe the optical counterpart(s) of the unresolved X-ray source, we oriented the spectrograph slit with the position angle of such a binary-pair candidate to image them simultaneously. For the 18 targets listed in Table B.1 we acquired their long-slit spectra to characterize both of them. We subsequently determined if they are physically associated or if that is just a spurious association. We note that the sources #6 and #40 have two entries in this Table. Since the separation between the two apertures was large enough to avoid any contamination of the spectrum extracted from the second aperture by the light of the bright source (and for the sake of homogenization of data reduction), we used the procedure of extraction within the `IRAF` environment, `APALL`, with the exception of the source #40. Nevertheless, we applied the procedure detailed in Appendix A to estimate the average separation in pixels between the two apertures. We then converted it into an angular separation ρ according to the spatial scale indicated above.

Based on our estimate of the angular separation and the position angle value recorded in the header of the raw data, we were able to identify each of sources located near one of our targets by relying mainly on the *Gaia* DR2 catalog (Table B.1).

Appendix B.2: Comoving stars in Gaia *DR2*

To search for any common proper-motion companions to our targets, we made use of a search cone of a radius of 2′ around each of them in *Gaia* DR2. Taking advantage of the very accurate astrometry in this catalog, we found comoving stars for 46 of our targets (Table 5). In 90 % of cases, we identified one companion only. Nevertheless, the sources #123, #125, #192, and F3 have two comoving companions, while we are able to list three for source #149. These five targets have one close companion ($\rho < 10''$) and at least another more distant one ($\rho > 40''$).

For the closest systems ($\pi \geqslant 4$ mas), we also extended the radius of search cone up to 10′. We then found that *i)* the source #6 has another common proper-motion companion with a large angular separation (ρ = 3.′44 ± 0.185 mas) and *ii)* the sources G3 and G4 are separated by 4.′96 ± 0.033 mas.

Table B.1. Identification of the second source that we have imaged during the acquisition of the IDS spectrum of our target.

#	Source name
6 c1	TYC 4500-1549-1
6 c3	*Gaia* DR2 5647079733733134080
31 c1	*Gaia* DR2 4752514328201438 72
37 c2	TYC 4354-793-1
40 c2	*Gaia* DR2 1116789735748819968
40 c3	*Gaia* DR2 1116789667029342080
42 c2	*Gaia* DR2 1116535920362524928
44 c2	TYC 4618-329-1
81 c2	*Gaia* DR2 1723454381704389248
106 c2	*Gaia* DR2 2248508292487691008
138 c2	*Gaia* DR2 2203366330791767552
140 c2	*Gaia* DR2 2005807146670408704
163 c2	*Gaia* DR2 537608345003955840
168 c2	*Gaia* DR2 534835788997551488
169 c2	*Gaia* DR2 533784174844087168
174 c2	*Gaia* DR2 2291000598671699200
184 c2	*Gaia* DR2 2206637339215351936
185 c2	*Gaia* DR2 2226453257466755328
191 c2	*Gaia* DR2 2231866565525667712
G3 c2	*Gaia* DR2 5646984517893591 04

Appendix B.3: Spectroscopic systems

Table B.2 lists 44 spectroscopic systems found from our analysis of the CCF profiles (Sect. 3.1). We also include 17 possible spectroscopic systems for which the CCF profile is slightly asymmetric or the profile of the Hα line is double-peaked. In the latter case, the absence of a second peak in the CCF profile can be explained by a mass ratio of the two sources much different from 1, but that the activity of the fainter star is sufficiently strong so that its Hα line is visible in the spectrum obtained during the combined observation of the two sources.

Table B.2 also highlights the lithium-rich systems. Except for the SB1 systems, the determination of $W_{\rm Li}$ value for each component of the SB2 and SB3 systems goes beyond the scope of the work presented here (see Frasca et al. 2006 and Klutsch et al. 2008 for a detailed analysis of SB2 and SB3 systems, respectively). We therefore decided to characterize the profile of the multiple Li I λ6707.8 lines qualitatively. To this end, we compared their intensity with respect to that of the nearby Ca I λ6717.7 line. We selected any system with Li I lines deeper than about the half of the Ca I ones. We divided them into two groups by assuming that the Li I lines deeper than about the Ca I ones are very strong. The remaining sources are therefore listed as displaying a strong lithium line. Among the 44 spectroscopic systems, the lithium line is visible in the spectrum of 22 (50 %) sources. This includes nine (20 %) and six sources (14 %) with a strong and very strong lithium line, respectively.

Table B.2. Spectroscopic systems among our targets. Any source whose lithium line is visible in absorption is named in bold. With respect to the profile of the Ca I λ6717.7 line, we also highlight those for which the Li I λ6707.8 line is **strong** and **very strong** (see text for details).

SB1	**1RXS J043208.0+811627**, 1RXS J062558.2+822124, **1RXS J083407.4+791449**, **1RXS J093852.0+852625**, 1RXS J193958.2+851032, **1RXS J213749.2+803228**, **1RXS J231616.5+784156**, 1RXS J232209.7+575626, **1RXS J232647.5+770304**.
SB1?	1RXS J155547.5+684014, **1RXS J181048.9+701601**, **1RXS J222706.6+652127**.
SB2	**1RXS J000142.0+773057**, 1RXS J000806.3+475659, **1RXS J003904.2+791912c1**, **1RXS J003941.9+790526**, 1RXS J010929.0+683916, **1RXS J011415.5+715933**, **1RXS J011523.1+882923**, 1RXS J012927.4+744448, **1RXS J013925.5+701853c1**, 1RXS J023919.7+872828, 1RXS J024324.6+695320, 1RXS J025538.5+544706, 1RXS J030926.6+673238, **1RXS J040745.1+875030**, 1RXS J061946.4+771933c2, 1RXS J085353.7+870708, 1RXS J163747.2+723937, **1RXS J170526.8+743600**, **1RXS J171928.8+652227**, 1RXS J175910.1+584300, 1RXS J183627.4+715311, 1RXS J193141.7+641951, **1RXS J195758.2+664253**, 1RXS J203857.5+580452, **1RXS J212929.0+621859**, 1RXS J214719.8+611618, 1RXS J224917.6+522634, 1RXS 189583.
Likely SB2	1RXS J005300.8+682125, **1RXS J044912.7+773719**, **1RXS J071743.1+764416**, **1RXS J181610.9+585539**.
SB2?	**1RXS J000002.5+733942c1**, **1RXS J010117.1+713114**, **1RXS J045808.2+790813**, 1RXS J050642.4+745604c2, 1RXS J064241.4+880442, 1RXS J075427.0+780633, 1RXS J161939.9+765515, 1RXS J165315.4+701554, **1RXS J192127.4+611208**, **1RXS J195542.3+663207**, **1RXS J203549.9+594930**, **1RXS J230822.7+790829**, **1RXS J235502.1+541516**.
SB3	1RXS J050642.4+745604c1, **1RXS J185131.1+584258**, **1RXS J232346.4+620620**.
SB3?	**1RXS J211232.5+741227**.

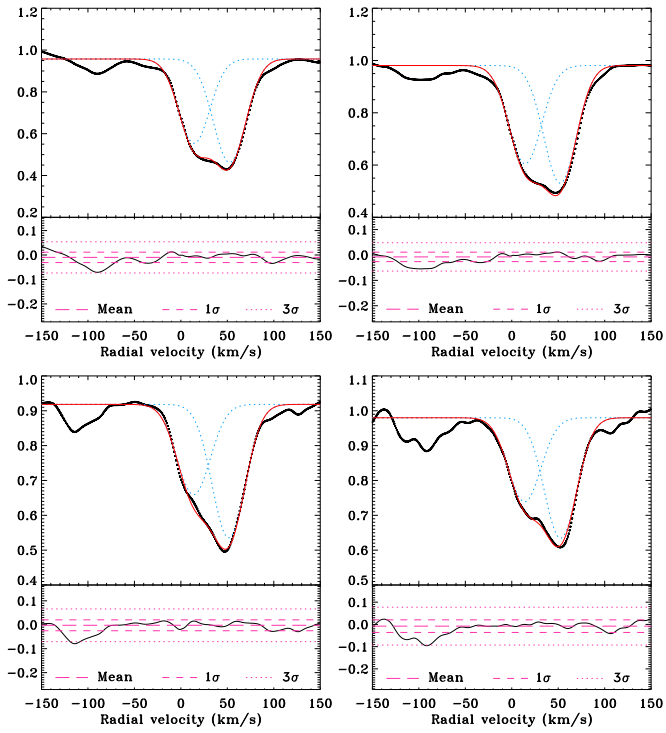


Fig. B.1. Cross-correlation function (asterisks) and Gaussian fitting (red solid line) for the source #10 obtained from different orders of the SOPHIE spectrum (*upper panel of each box*). We denote the Gaussian fitting of each individual peak with the blue dotted lines. We also display the CCF residuals (*lower panel of each box*).

Figure B.1 displays the complexity of some systems and the need to carefully analyze the CCF residues after subtracting the fitting, especially when the two peaks are severely blended (i.e., one peak with a clearly asymmetric shape) on several orders. We consider the source #10 as an SB2 system observed near the conjunction but we have also to point out the possible detection of an additional smaller peak in its CCF profile. However its amplitude remains below our threshold.

Appendix C: Low-mass stars

We used Eq. (12) from Lépine et al. (2013) to convert the $V–J$ color index listed in the Table 1 into spectral type. We found that 45 of our targets are likely M-type stars (Table C.1). For six of them (#20, #48, #54, #61, #62, #69), we were not able to acquire a spectrum to confirm this classification.

Due to their low luminosity and our observational strategy, the survey of low-mass stars could only be conducted with the IDS spectrograph. For these sources, we normalized the spectra in two different ways to perform their spectral typing.

First, we defined the pseudo-continuum as a smooth line passing through the heads of molecular bands (see, e.g., Zapatero Osorio et al. 2002). In this way, all the molecular bands are fully in absorption and only the band-heads reach the 1.0 level. Such a task is impossible to be performed automatically. Normalized spectra are obtained by dividing each target spectrum by its continuum. This optimizes the comparison of our spectra with the Élodie library of standard stars, within the code ROTFIT. We refer the reader to Frasca et al. (2015) for an application of this code to M-type stars. The results are listed in Table 3.

Secondly, we divided each target spectrum by the continuum level in the spectral region near the Hα line. This procedure allows us to perform the spectral typing of the M-type stars through a comparative analysis of the spectral shape of our targets with those of standard stars observed with the same instrumental setup (Table E.1). To this end, we discarded the wavelength ranges contaminated by strong telluric lines or by chromospheric activity (e.g., the Balmer series). We looked for the best matches by means of a least-square minimization technique similar to that used by Klutsch et al. (2012) for the M-type stars from the CARMENES Input Catalog (CARMENCITA, Caballero et al. 2013). Based on an internal comparison of the CARMENES results as well as with three independent works, Alonso-Floriano et al. (2015) highlighted the reliability of this approach. The spectral typing resulting from both our procedures are fully compatible with each other. Table C.1 compares the spectral-type classifications resulting from our analysis with those available in the literature, and shows that they agree with each other with an accuracy of about one subclass. We finally found that three of these low-mass stars are late-K stars rather than early-M ones. Figure C.1 shows the spectra of the 36 surveyed M-type stars, sorted by spectral type (from M0 to M4.5).

Table C.1. Comparison of the spectral type derived for low-mass stars with those listed in the literature.

#	Spectral type from:					
	This work	Lépine et al. (2013)	CARMENCITA [a]	SpT vs. V–J relation [b]	Other(s)	Refs.
2	M3.5V	M4V	…	M3.4	M3.5+M3.6, M4V	9, 11
3	M2.5V	…	M2.5V	M2.4	M2.4V	8
5	M4V	M4V	M4V+M	M3.6	M4.0+M4.5, M3.7V	7, 8
6c2	M1V	…	…	M0.4	M2V	6
9	M1V	M1.5V	…	M1.2	…	…
12	M2.5V	…	…	M0.9	…	…
14	M3.5V	…	…	M0.8	…	…
15	M0.5V	…	…	M3.1	…	…
20	…	…	…	M2.4	…	…
21	M3V	…	…	M3.6	M2e	5
23	M3.5V	…	…	M1.9	…	…
24	M1.5V	M2V	M1V	M2.7	M3	2
26	M0.5V	…	…	M2.5	…	…
29	M0V	…	…	M1.0	…	…
30	M4V	…	…	M3.7	…	…
34	M1V	…	…	M1.8	…	…
35	M0.5V	…	…	M1.3	…	…
38	M0V	…	…	K7.85	K5/M0	3
39	M3.5V	…	…	M3.8	…	…
48	…	M4V	M3.5V	M4.1	M4/5	10
54	…	…	…	M2.8	M3/4	10
61	…	…	…	M1.0	…	…
62	…	M4V	…	M4.1	…	…
69	…	…	…	M2.4	…	…
70	M3V	M2.5V	…	M1.7	…	…
73	M1V	…	…	M1.4	…	…
80	M1.5V	…	…	M1.9	…	…
81c1	M1V	…	…	…	…	…
81c2	M2.5V	…	…	…	…	…
85	M2V	…	…	M1.2	M2V	11
88	M4V	M4V	M3.5V	M3.6	M4Ve	4
107	M0V	…	…	M0.5	…	…
111	M1V	…	…	M1.4	…	…
113	M0V	M0V	…	M0.6	…	…
121	M3.5V	…	…	M4.6	…	…
124	K7V	…	…	M0.2	…	…
136	K6V	…	…	M0.2	…	…
143	M0V	…	…	M2.0	…	…
146	M0.5V	…	…	M2.6	…	…
151	M0V	M0.5V	M0V	M1.0	M0V, M0.3V	1, 8
154	M0.5V	…	…	M1.9	…	…
161	M1.5V	…	…	M2.6	…	…
189	K7V	…	…	M1.1	…	…
191c1	M0V	…	…	M1.2	K7V	6
191c2	M2V	…	…	…	M3V	6

Notes.
[a] CARMENCITA stands for "CARMENes Cool star Information and daTa Archive" and is a private database of the CARMENES consortium (http://carmenes.caha.es/), [b] We converted the V–J color index into spectral type by using Eq.(12) of Lépine et al. (2013).
References.
1 = Vyssotsky (1956); 2 = Lee (1984); 3 = Stephenson (1986); 4 = Fleming et al. (1988); 5 = Motch et al. (1998); 6 = Tachihara et al. (2005); 7 = Daemgen et al. (2007); 8 = Shkolnik et al. (2009); 9 = Shkolnik et al. (2010); 10 = Gigoyan & Mickaelian (2012); and 11 = Janson et al. (2012).

Appendix D: Information about some stars

– 1RXS J003904.2+791912 (Source #6): The infrared counterpart identified for this source corresponds to the faint companion of the source [TNK2005] 5 that is known as a WTTS in Cepheus (Tachihara et al. 2005). Our target was only detected in photometry and classified as an M2-type companion candidate by the aforementioned authors. During one of our observing nights, both components were positioned simultaneously on the slit. These display a deep lithium absorption and the brightest component is an SB2 system (Fig. D.1). Based on our analysis, this source therefore is a hierarchical triple system composed of a close inner binary plus a tertiary component in a long-period orbit. Moreover, we found an additional wide-separation companion (ρ = 3.″44 ± 0.185 mas; see Table 5). All these stars are associated to Cep I.

– 1RXS J010112.8+570839 (Source #8): While its intrinsic color agrees with a late-M giant (see Fig. 4, along with Fig. 2 of Jiménez-Esteban et al. 2012), we classified it as a K5 giant with a large uncertainty on its surface gravity ($\log g$ = 4.20 ± 0.95 dex). This is consistent with the extinction of $A_V \sim 0.94$ mag derived from our SED analysis (Sect. 3.3). Moreover, this source is more than 2 mag fainter compared to giants included in the LSPM-North catalog (Lépine & Shara 2005), with a similar J–K_s color index.

– 1RXS J174104.6+842458 (Source #81): This visual binary is composed of an M1 and an M2.5-type star, with a small angular separation (Table 5). These are the only M-type stars displaying the He I λ6678 Å line in emission (Fig. C.1).

– 1RXS J185131.1+584258 (Source #92): We observed this source thrice. At the first epoch, it appears as an SB3 system. We then re-observed this star during our IDS runs in

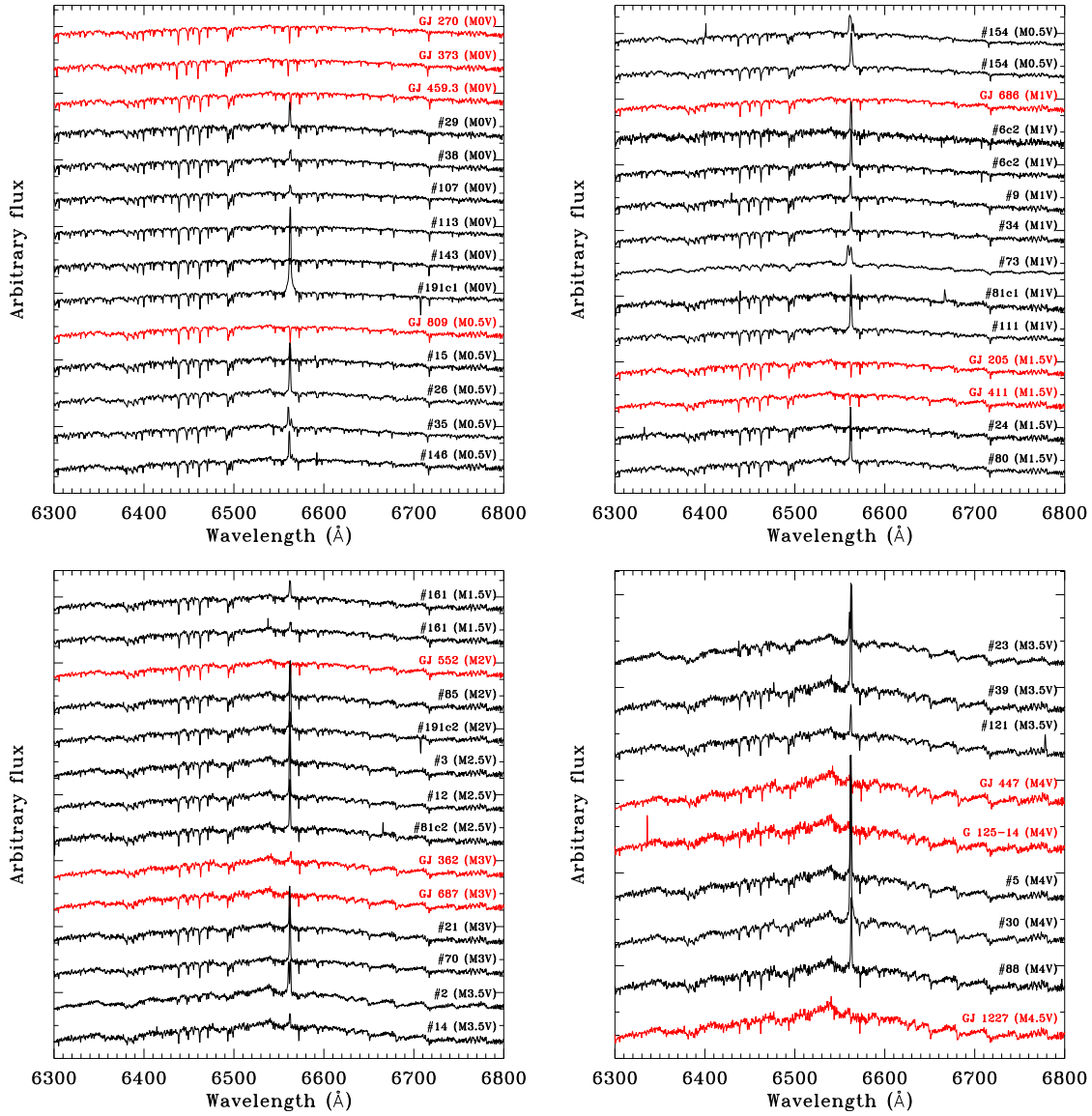


Fig. C.1. Sequential distribution of spectra for the M-type stars. Their coloring clearly distinguishes targets (black) from standards (red).

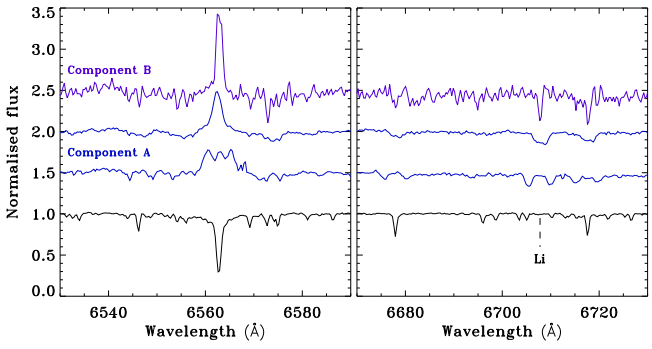


Fig. D.1. Hα and lithium spectra of TYC 4500-1549-1 (#6) found as a visual binary. Two of spectra for the bright component are also shown.

order to learn more about the temporal variation of this system. Since the source turned out to be an SB2 system, we repeated the observation. Within this time span of about one day its spectrum has drastically changed and a third peaks is clearly visible in the CCF profile (Fig. D.2). At this stage, it is complicated to put forward any hypothesis about the dynamics of this system, but the radial velocity of the three components seem to change quickly. This is in contrast with the three SB3 systems analyzed by Klutsch et al. (2008).

– 1RXS J192215.6+673918 (Source #99): We selected the source 2MASS J19221478+6739142 as its infrared counterpart. With an angular separation of ∼6.″42, this source fulfilled all our criteria. Its infrared colors suggest a late M-type star according to West et al. (2008). At this position, however, we observed a giant star ($T_{\rm eff}$ = 4835 ± 102 K, $\log g$ = 2.80 ± 0.23 dex, and spectral type = G9 III) with a small lithium absorption line: EW(Li) = 16 ± 11 mÅ, and log N(Li) ∼ 0.9 dex. Seeking to understand the inconsistency between the photometric and spectroscopic data, we found that 2MASX 19221485+6739143 from the catalog of the 2MASS extended sources (Skrutskie et al. 2003) has sim-

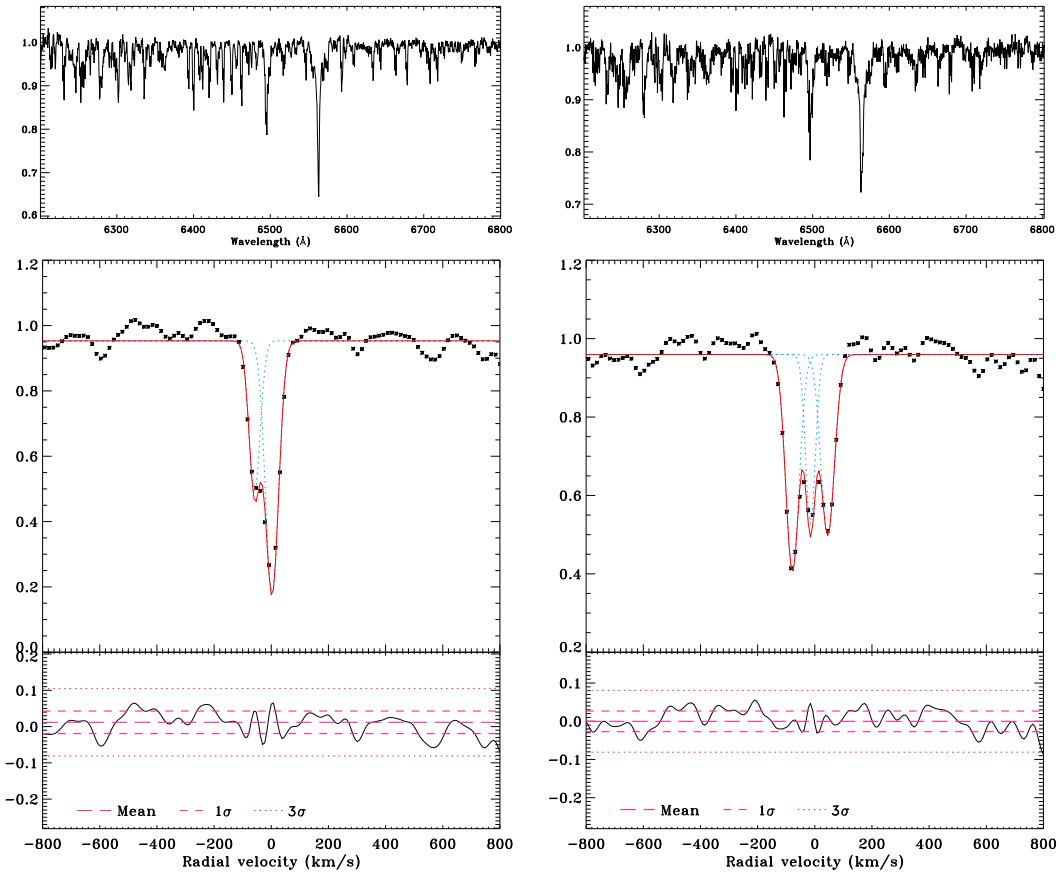


Fig. D.2. IDS spectra of the source #92 obtained in a time span of about 24 hours (*top panels*) and their associated CCF profiles (*bottom panels*).

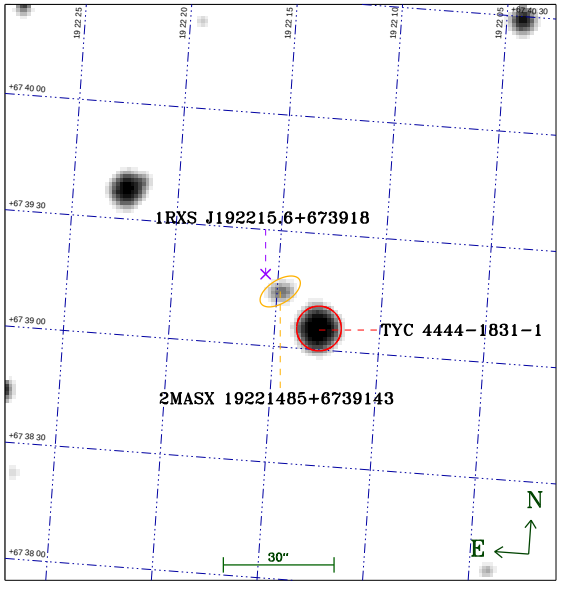


Fig. D.3. Photographic B_J-band image of the second Palomar Observatory Sky Survey (POSS-II, epoch J1992.57), centered on the 2MASS extended source 2MASX 19221485+6739143. We also show the positions of the X-ray source 1RXS J192215.6+673918 (#99) and the optical source TYC 4444-1831-1.

ilar coordinates. Therefore the infrared counterpart of this target is indeed the galaxy GALEX J192214.8+673914.

It appears that we observed the source TYC 4444-1831-1 (or 2MASS J19221289+6739053) that is somewhat more distant with a separation of ∼20.″42 to the X-ray source. We illustrated the space configuration of these three sources on Fig. D.3. Moreover, its photometry is consistent with a late-G or early-K star and its small proper motions are in agreement with the expectation for a giant star. The probabilities of Flesch (2010) are rather close that the radio/X-ray association is erroneous (51 %) and this X-ray source is a star (42 %), while the probability to be a galaxy is only of 7 %.

– 1RXS J221055.6+632339 (Source #139): As in Motch et al. (1997b), we consider the early-type star STF 2879 C (Fig. D.4) as being its optical counterpart due to its B–V color index of about 0.75 ± 0.44 mag from the GSC II photometric data. In contrast, the APASS catalog reported a more reliable color index (B–V = 0.320 ± 0.031 mag). This source has probably passed through the cracks because of its proximity to the B5 binary V447 Cep whose extended halo of light could affect the entire photometry of our target (Fig. D.5). Nevertheless, the particularity of this source is not limited to this aspect. Its magnitudes quoted in the final release of the WISE all-sky survey catalog are also atypical. With a $W1$ magnitude of 10.819 ± 0.023 mag and a $W1$–$W4$ of 4.691 ± 0.050 mag, this source falls in the area mainly populated by T Tauri stars displaying an infrared excess (Guillout, priv. com.).
– 1RXS 184257 (Source #160): This source (= [KP93] 2−43 in Kun & Prusti 1993) is too faint in optical to acquire a spectrum with the instruments at our disposal in a reasonable exposure time. It is known as a visual binary whose primary

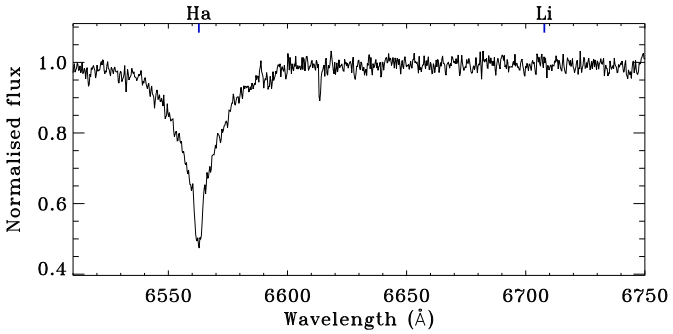


Fig. D.4. IDS spectrum of source #139.

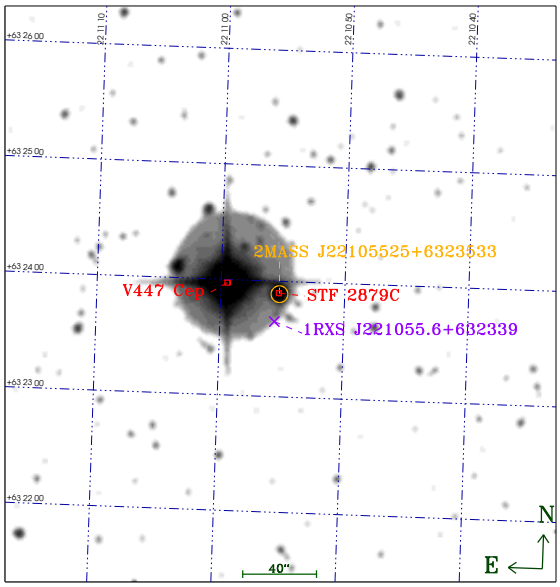


Fig. D.5. Photographic B_J-band image of the second Palomar Observatory Sky Survey (POSS-II), centered on the infrared source 2MASS J22105525+6323533. We mark the locus of the X-ray source 1RXS J221055.6+632339 (#139) and its possible optical counterpart STF 2879 C, which is the companion of the bright B5 binary V447 Cep.

component is a young star (1-Myr-old WTTS in Kun et al. 2009 or a CTTS in Simon 2009) and one of the strongest X-ray emitters during the XMM-Newton and Chandra observations of the L1251 cloud (Simon 2006, 2009).

– 1RXS J003941.9+790526 (Source G4): We followed a procedure similar to Frasca et al. (2006) to derive its orbital parameters. For this purpose we combined the radial velocities that we previously reported in Paper III with those obtained during the observing runs analyzed in the current paper. However it turns out that most measurements (HJD = 2455077–2455111) only cover half of the orbit of this system. From our preliminary analysis the period would be estimated at ∼70 days.

Appendix E: Additional materials online

All long online tables are available at the CDS. Table 1 summarizes the optical and infrared names of each X-ray source, along with those appearing in Simbad and some main parameters coming from the literature. The three additional online tables present

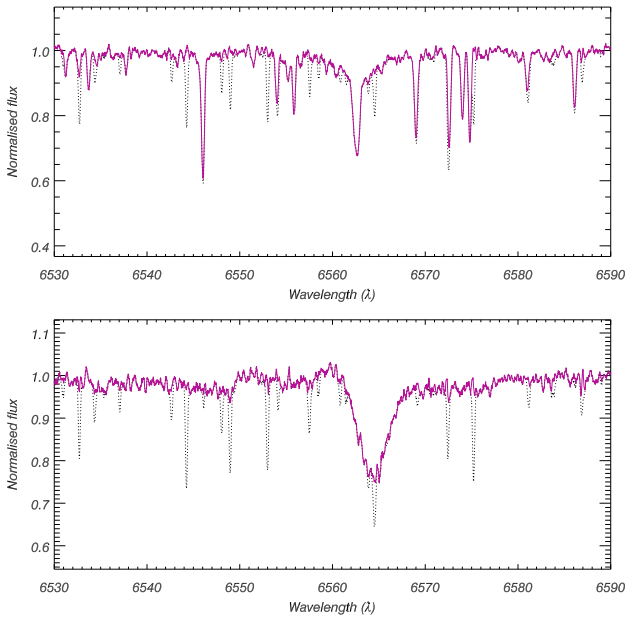


Fig. E.1. Results of our telluric line removal on SOPHIE spectra for a slow-rotating source (*top panel*) and a fast rotator (*bottom panel*). On each panel, the black dotted lines and purple solid lines show the spectra before and after the application of our procedure, respectively.

our results. Table 3 reports the radial velocity of all the stars, including the measurements for each component of a spectroscopic system, along with the rotational velocity, atmospheric parameters, and lithium equivalent widths derived for the targets identified as single stars or SB1 systems. Table 4 provides the astrometry in *Gaia* DR2, the Galactic positions, and the extinction estimate of our targets, as well as the space velocities of those identified as single stars. Table 5 lists all the sources that are comoving with one of our targets.

To derive the radial and rotational velocities of our targets and to perform their spectral typing, we made use of a smaller library of template spectra taken with FOCES and IDS during our observing runs. Their spectral type, atmospheric parameters, and radial and rotational velocities are given in Table E.1.

We show the efficiency of our procedure for removing telluric lines in the case of a few SOPHIE spectra (Fig. E.1). For each target observed during our survey, we display only one spectrum in the region around the Li I λ6707.8 line (Fig. E.2).

Table E.1. Basic parameters of reference stars observed during our runs. We adopted the spectral type, atmospheric parameters, and projected rotational velocities found in the literature (see references below). We also determined the mean RV values from those listed in the online Élodie archive, along with the number of observations used o_{RV}.

Star name	SpT [a]	Ref.	$T_{\rm eff}$ [b] (K)	$\log g$ [b] (cm^2 s^{-1})	[Fe/H] [b] (dex)	Ref.	$v \sin i$ [c] (km s^{-1})	Ref.	$\langle RV \rangle$ [d] (km s^{-1})	o_{RV}
HD 187691	F8 V	A3	6173	4.25	0.04	B15	3.6	C3	0.03	6
HD 19373	F9.5 V	A4	6008	4.33	0.15	B12	4.5	B11	49.4	1
HD 22879	G0 V	A3	5759	4.25	−0.85	B14	2.3	C3	120.31	4
HD 10307	G1 V	A4	5859	4.27	0.04	B15	2.3	C3	4.97	10
HD 159222	G1 V	A4	5851	4.41	0.16	B12	3.3	B11	−51.62	15
HD 196850	G1 V	A4	5838	4.37	−0.09	B16	2.0	B02	−21.07	9
HD 197076	G1 V	A4	5828	4.45	−0.10	B15	2.7	C7	−35.44	13
HD 19445	G2 V Fe-3	A4	5918	4.41	−1.89	B08	4.1	C2	−139.84	2
HD 193664	G3 V	A5	5886	4.48	−0.09	B02	1.3	B02	−4.51	28
HD 65583	G8 V	A1	5279	4.76	−0.69	B02	3.3	C8	14.89 [3]	20
HD 10700	G8.5 V	A6	5290	4.46	−0.48	B11	0.9	C3	−16.65	1
HD 10780	G9 V	A4	5309	4.56	0.00	B04	1.3	B01	2.72	33
HD 12051	G9 V	A4	5458	4.55	0.24	B07	0.5	B06	-35.22	4
HD 185144	G9 V	A4	5204	4.37	−0.26	B15	0.8	C3	26.61	1
HD 182488	G9+ V	A4	5393	4.55	0.22	B05	1.2	C3	−21.57	12
HD 3651	K0 V	A4	5218	4.52	0.20	B05	1.2	C2	−33.08	2
HD 38230	K0 V	A4	5174	4.53	−0.08	B02	0.9	C3	−29.22	33
HD 10476	K1 V	A6	5173	4.59	−0.08	B04	1.7	B01	−33.76	3
HD 4628	K2 V	A4	4905	4.60	−0.36	B07	1.5	B06	−10.35	1
HD 73667	K2 V	A4	4884	4.40	−0.58	B07	1.2	B01	−12.12	21
HD 166620	K2 V	A4	5007	4.62	−0.24	B04	0.6	C3	−19.59	3
HD 16160	K3 V	A6	4829	4.60	−0.16	B07	0.9	B06	25.73	1
HD 219134	K3 V	A4	4835	4.56	0.12	B02	1.8	B01	−18.69	4
HD 190007	K4 V	A4	4786	4.31	−0.02	B10	0.9	B10	−30.43	10
HD 201091	K5 V	A4	4236	4.50	−0.03	B07	3.8	B06	−65.51	5
HD 221503	K6 V	A6	4270	4.99	0.02	B13	2.5	C4	−0.96 [5]	6
HD 201092	K7 V	A4	4200	4.60	−0.63	B09	1.6	C3	−64.15	5
GJ 270	M0 V	A9	3856	4.69	...	B17	$\leqslant 3.0$	C9	−69.78 [4]	1
GJ 373	M0 V	A9	3820	4.68	...	B17	$\leqslant 2.0$	C9	15.13 [4]	4
GJ 459.3	M0 V	A9	3852	4.66	...	B17	$\leqslant 3.0$	C9	−0.64	1
GJ 809	M0.5 V	A9	3720	4.67	−0.13	B01	$\leqslant 2.0$	C9	−17.55	10
GJ 686	M1 V	A9	3611	4.84	−0.44	A8	$\leqslant 2.0$	C9	−9.87	11
GJ 205	M1.5 V	A9	3626	4.80	0.60	B09	$\leqslant 2.0$	C9	8.25	15
GJ 411	M1.5 V	A9	3671	4.89	...	B17	$\leqslant 2.0$	C9	−84.71 [4]	7
GJ 552	M2 V	A9	3574	4.79	...	B17	$\leqslant 2.0$	C9	7.36 [4]	2
GJ 362	M3 V	A9	3430	4.85	...	B17	$\leqslant 2.0$	C9	6.21	2
GJ 687	M3 V	A9	3340	4.82	0.15	B01	$\leqslant 2.5$	C9	−29.16	9
GJ 447	M4 V	A9	3192	5.07	...	B17	$\leqslant 2.0$	C9	−30.86 [4]	1
GJ 1227	M4.5 V	A8	3072	5.01	...	B17	$\leqslant 2.0$	C9	−14.04	6
HD 84737	G0 IV-V	A4	5934	4.16	0.16	B12	3.0	B11	4.79 [1]	25
HD 51000	G5 III	A2	5180	3.05	−0.04	B03	2.3	B03	−9.36	1
HD 62509	G9 III	A7	4955	3.07	0.16	B15	2.4	C3	3.24	2
HD 124897	K0 III	A4	4280	1.69	−0.52	B06	2.5	C3	−5.30	8
HD 12929	K1 III	A4	4546	2.40	−0.24	B04	1.6	C3	−14.64 [2]	170
HD 26162	K2 III	A2	4800	2.90	0.06	B03	4.0	B03	24.74	7
HD 29139	K5 III	A6	3891	1.20	−0.15	B06	2.6	C3	54.02	8

References.

[a] For the G- and K-type sources, we list the spectral type most often cited in the last release of the catalog of stellar spectral classification (Skiff 2010):
A1 = Harlan (1969), A2 = Cowley & Bidelman (1979), A3 = Gray et al. (2001), A4 = Gray et al. (2003), A5 = Abt & Willmarth (2006), A6 = Gray et al. (2006), A7 = Abt (2008), and A8 = Jenkins et al. (2009).
For the M-type stars, we usually adopt the spectral type from Alonso-Floriano et al. (2015), labeled A9.

[b] The atmospheric parameters come from: B01 = Woolf & Wallerstein (2005), B02 = Valenti & Fischer (2005), B03= Hekker & Meléndez (2007), B04 = Ramírez et al. (2007), B05 = Fuhrmann (2008), B06 = Meléndez et al. (2008), B07 = Mishenina et al. (2008), B08 = Reddy & Lambert (2008), B09 = Frasca et al. (2009), B10 = Guillout et al. (2009), B11 = Bruntt et al. (2010), B12 = Gonzalez et al. (2010), B13 = Casagrande et al. (2010), B14 = Nissen & Schuster (2010), B15 = da Silva et al. (2011), B16 = Casagrande et al. (2011), and B17 = Stassun et al. (2018). Most of them are available in the PASTEL catalog (Soubiran et al. 2010).

[c] $v \sin i$ values from: C1 = Delfosse et al. (1998), C2 = Fischer & Valenti (2005), C3 = the catalog of stellar rotational velocities of Glebocki & Gnacinski (2005), C4 = Torres et al. (2006), C5 = Houdebine (2010), C6 = Houdebine (2011), C7 = Herrero et al. (2012), C8 = McCarthy & Wilhelm (2014) , and C9 = Jeffers et al. (2018). Some of these publications contain also an AP determination.

[d] We also made use of the RV values from [1] Soubiran et al. (1998), [2] Famaey et al. (2005), [3] Soubiran et al. (2013), [4] Jeffers et al. (2018), and [5] Soubiran et al. (2018).

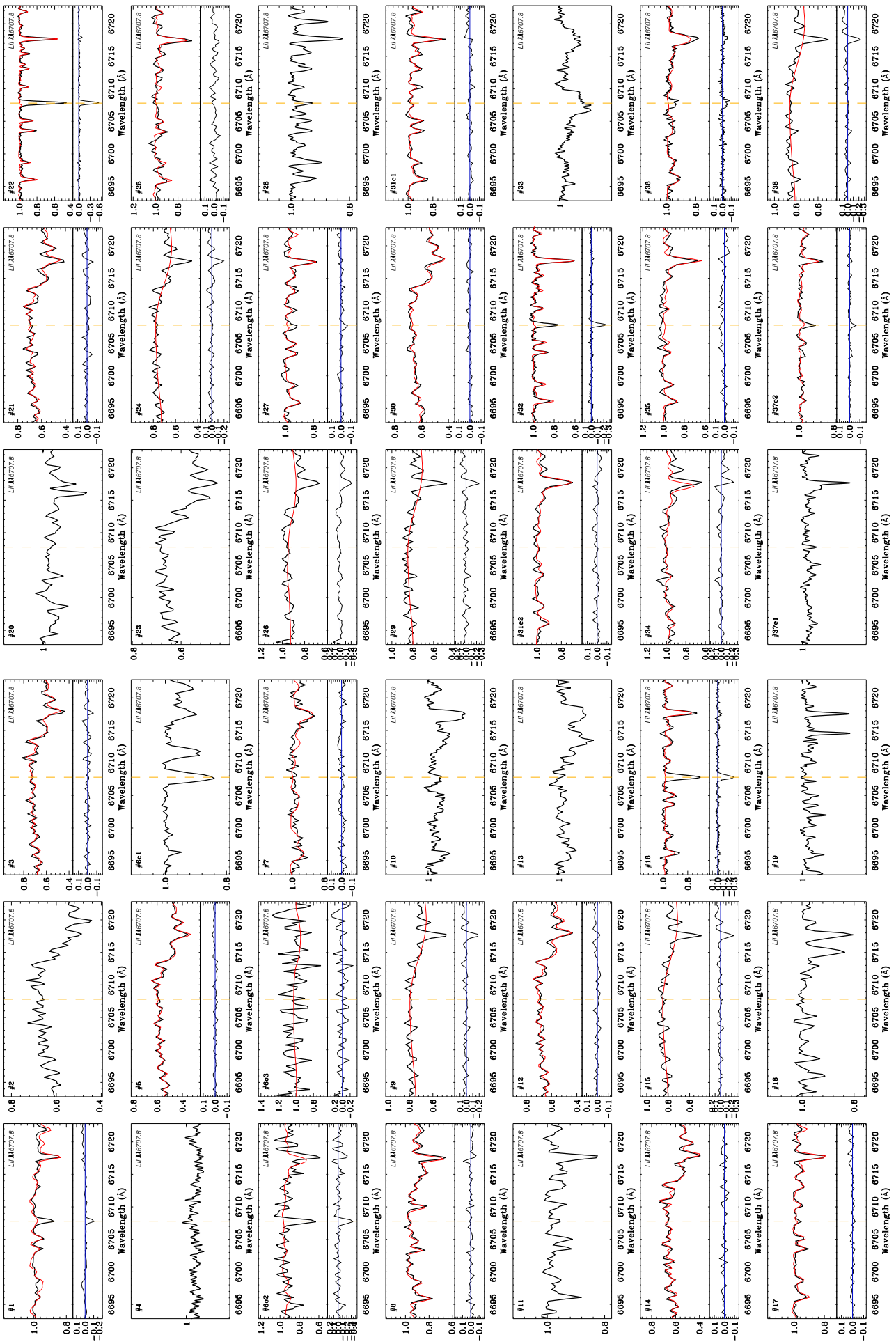


Fig. E.2. Target spectra (black line) around the lithium line (vertical dashed line). We display the best match rotationally broadened to the $v \sin i$ obtained with ROTFIT with the red line only for single stars and SB1 systems (*upper panel*), while the difference (target–template) spectrum shows their lithium content (*lower panel*). The number of the source appears in the upper left corner.

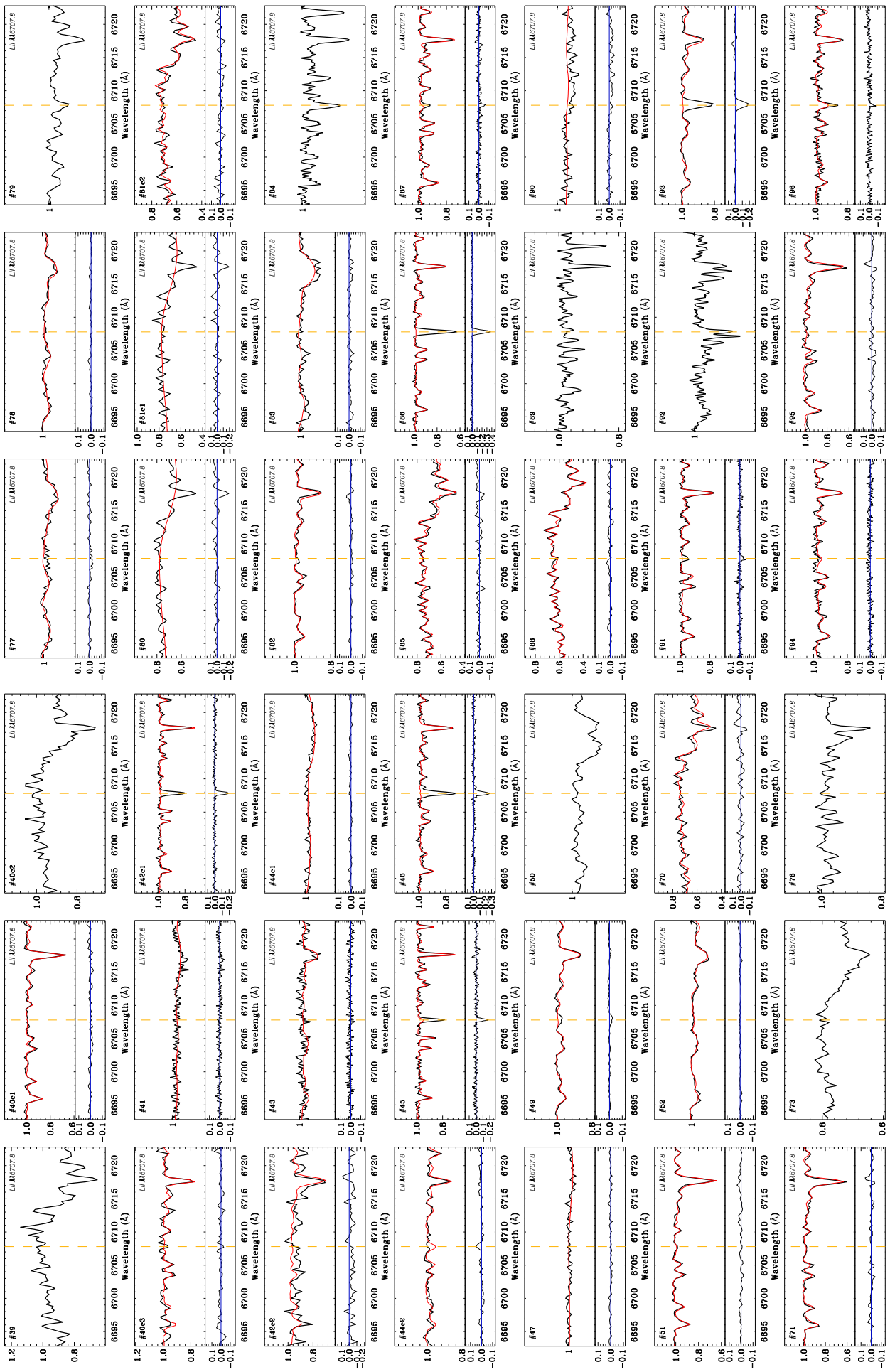


Fig. E.2. Continued

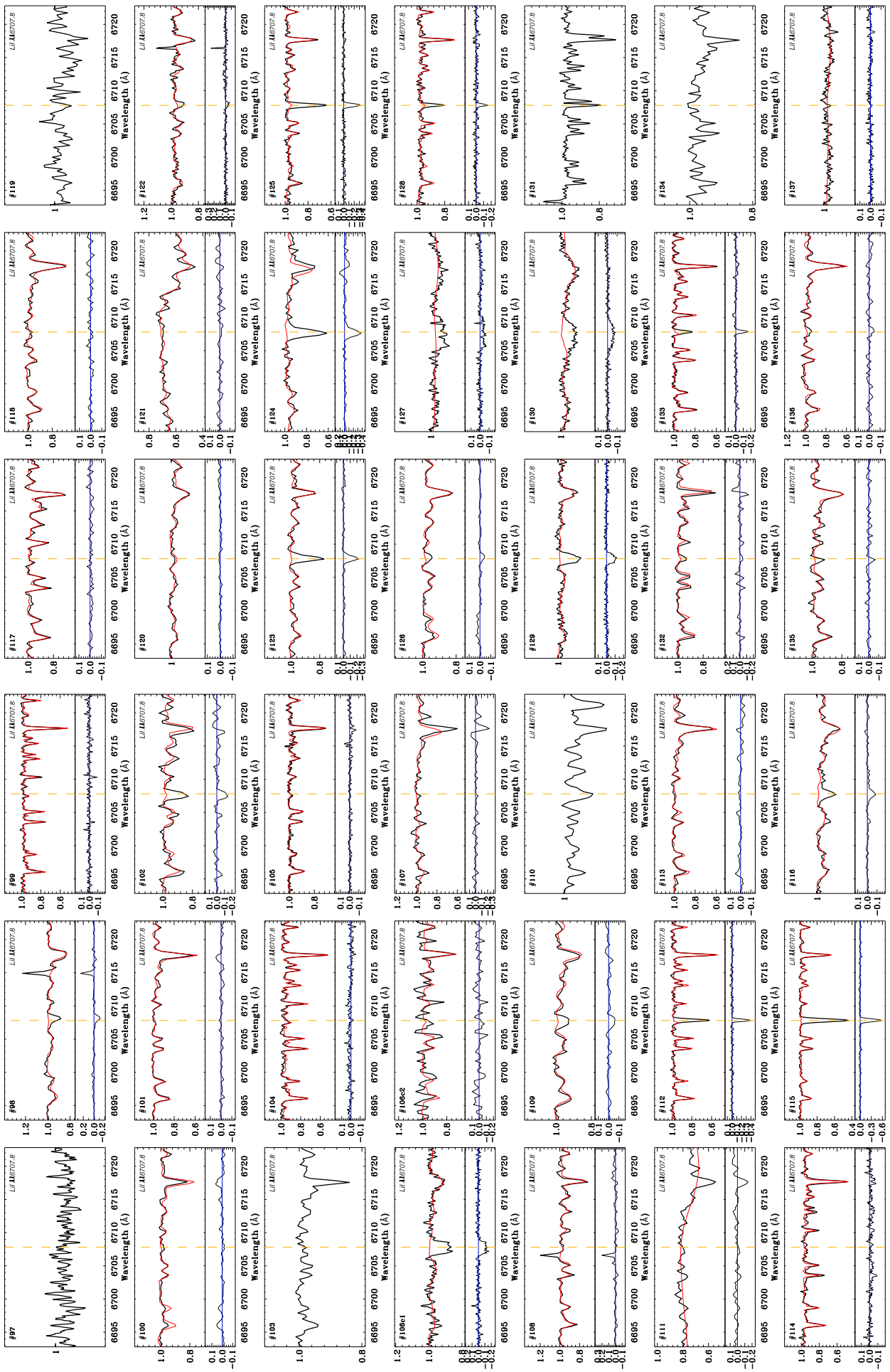


Fig. E.2. Continued

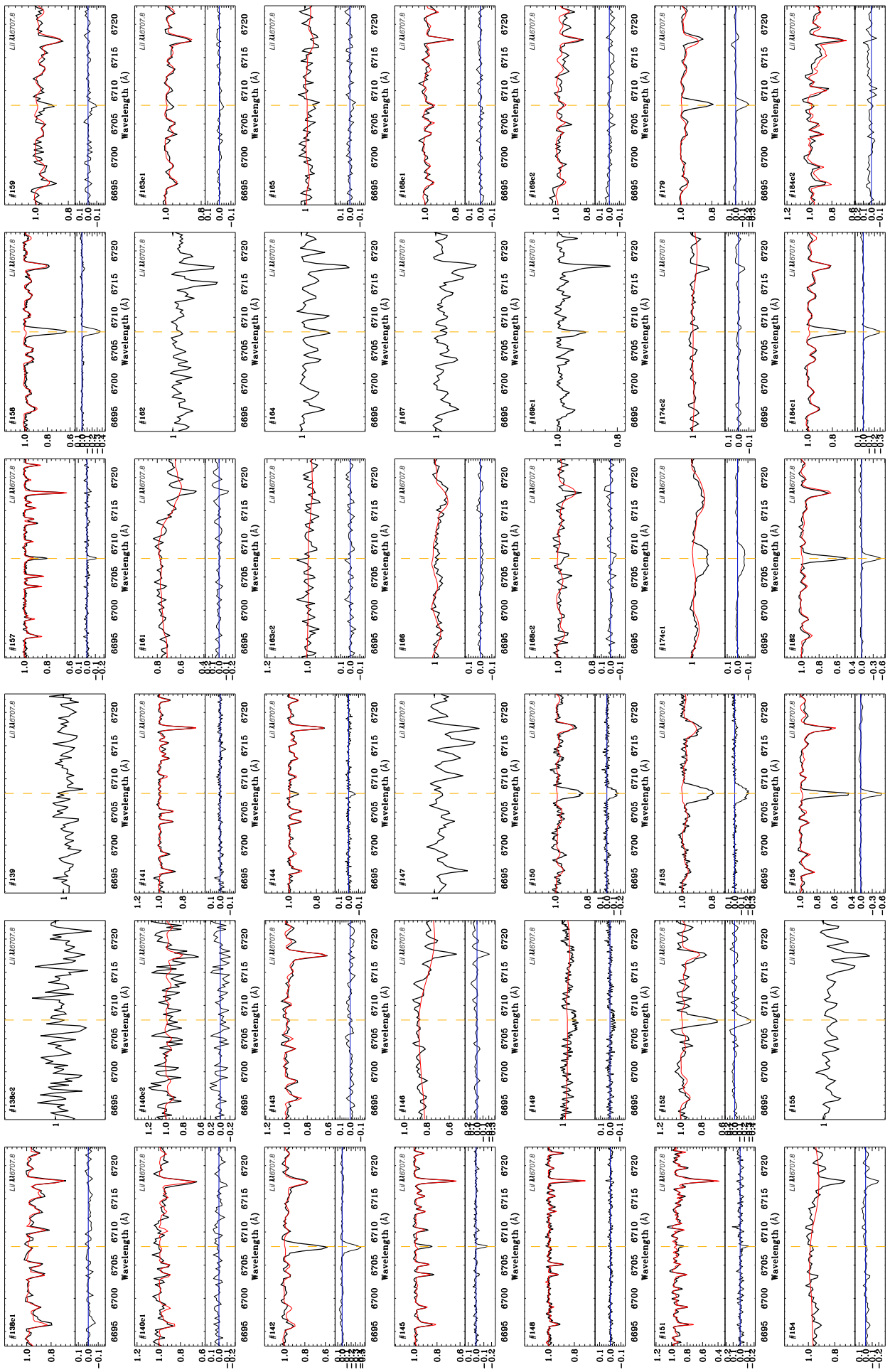


Fig. E.2. Continued

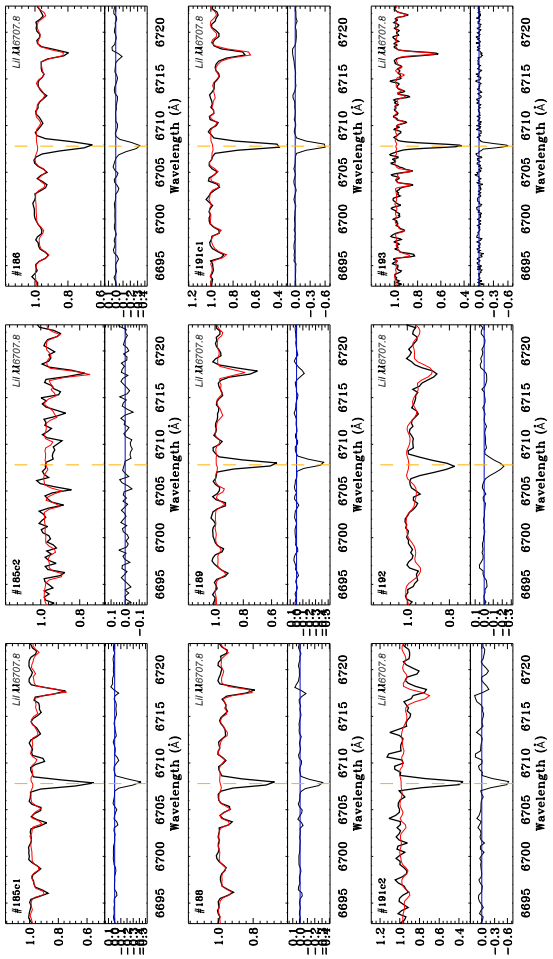


Fig. E.2. Continued

Table 1. Main parameters of the young stars candidates available in 2009, when the sample was created.

#	X-ray name 1RXS	IR name 2MASS	GSC II name	Other name	α (2000) (h m s)	δ (2000) (° ′ ″)	B (mag)	Ref.	V (mag)	Ref.	J (mag)	H (mag)	K_s (mag)	B–V [a] (mag)	V–J [b] (mag)
	Stars cross-identified with a source of the RASS catalogs:														
1	J000221.0+552519	J00022092+5525145	NAHS000445		00 02 20.929	+55 25 14.55	13.58	G_J	12.64	G_V	9.828	9.056	8.859	(0.94)	(2.81)
2 ‡	J000806.3+475659	J00080642+4757025	NAH9000368		00 08 06.428	+47 57 02.50	14.53	G_B	12.69	U	8.523	8.000	7.677	1.84	4.17
3 ‡	J002158.0+491245	J00215781+4912379	NAH1000233	GJ 3030	00 21 57.815	+49 12 37.96	13.43	G_J	12.75	U	9.139	8.454	8.205	(1.14)	3.61
4 *, ⋆	J002827.8+785750	J00282798+7857426	NAG0000520	TYC 4500-730-1	00 28 27.987	+78 57 42.70	11.20	T	10.61	T	9.251	8.916	8.868	0.59	1.36
5	J002854.1+502226	J00285391+5022330	NAIJ018308	GJ 3036	00 28 53.920	+50 22 33.02	14.09	G_J	13.16	U	8.847	8.289	7.991	[0.93]	4.32
6 *, ⋆, ‡	J003904.2+791912 [8]	J00390355+7919191	NAG3000177		00 39 03.554	+79 19 19.11	14.66	G_J	13.46	G_V	10.479	9.837	9.627	(1.20)	(2.98)
7 *, ‡	J005300.8+682125	J00530041+6821225	NAZ0000392	GSC 04296-00542	00 53 00.419	+68 21 22.52	12.80	G_J	12.01	G_V	10.088	9.468	9.367	(0.79)	(1.92)
8	J010112.8+570839	J01011345+5708444	NANY000113		01 01 13.458	+57 08 44.43	15.84	G_B	14.58	U	10.050	9.135	8.818	1.26	4.53
9	J011319.6+585523	J01131976+5855224	NANP000198	NLTT 4027	01 13 19.767	+58 55 22.42	12.73	G_J	11.58	U	8.409	7.770	7.570	(1.46)	3.17
10 ‡	J011415.5+715933	J01141803+7159271	NAD4000574	TYC 4305-1502-1	01 14 18.033	+71 59 27.12	12.15	T	11.43	T	10.132	9.611	9.484	0.73	1.30
11 ‡	J011523.1+882923	J01153189+8829200	NA9T000196		01 15 31.890	+88 29 20.04	13.53	G_J	12.50	U	9.733	9.069	8.877	[1.03]	2.77
12	J011740.0+582954	J01173999+5829508	NANP000382		01 17 39.996	+58 29 50.90	13.73	G_B	12.51	U	9.399	8.773	8.528	1.22	3.11
13 *, ‡	J012927.4+744448	J01292907+7444495	NACY000071	GSC 04309-00722	01 29 29.074	+74 44 49.51	14.01	G_J	13.40	U	10.641	10.066	9.925	(1.23)	2.76
14	J013426.8+642651	J01342688+6426505	NAZ6000334		01 34 26.886	+64 26 50.54	14.55	G_J	12.38	G_V	9.301	8.772	8.517	(2.17)	(3.08)
15	J015949.7+532301	J01595005+5323080	NBYW000158		01 59 50.055	+53 23 08.04	14.78	G_B	14.01	U	10.083	9.383	9.226	0.77	3.93
16	J020434.1+675635	J02043300+6756308	NAZ8000167		02 04 33.006	+67 56 30.88	13.66	G_B	12.71	U	10.579	10.091	10.003	0.85	2.13
17 *	J022036.3+774419	J02203711+7744132	NAGK000428	GSC 04499-02076	02 20 37.113	+77 44 13.20	13.98	G_B	12.60	U	9.619	8.969	8.811	1.38	2.98
18 ‡	J023919.7+872828	J02391539+8728237	NAA7000100		02 39 15.392	+87 28 23.73	13.78	G_B	12.89	U	10.642	10.012	9.813	0.89	2.25
19 ‡	J024324.6+695320	J02433138+6953362	NB0N000191	TYC 4316-2055-1	02 43 31.385	+69 53 36.22	11.83	T	11.08	T	9.716	9.285	9.249	0.75	1.36
20 ‡	J025538.5+544706	J02553878+5447121	NAIO000292		02 55 38.782	+54 47 12.12	13.91	Y	13.08	Y	10.405	9.700	9.454	(0.83)	3.61
21	J025620.0+614129	J02561984+6141223	NAWU000406	GSC 04048-00621	02 56 19.846	+61 41 22.37	14.89	G_B	14.04	U	9.741	9.170	8.927	0.85	4.30
22	J030016.2+722537	J03001477+7225410	NB0J000073	TYC 4321-507-1	03 00 14.779	+72 25 41.02	11.32	T	10.71	T	8.872	8.358	8.287	0.61	1.84
23 ‡	J030926.6+673238	J03092643+6732425	NB27000316		03 09 26.435	+67 32 42.51	15.03	G_B	13.00	U	9.572	8.986	8.767	2.03	3.43
24	J031026.1+582608	J03102649+5826086	NAVB000247	GJ 3204	03 10 26.490	+58 26 08.66	12.83	G_J	12.08	U	8.332	7.742	7.503	(1.27)	3.75
25 ‡	J032802.3+642341	J03280189+6423409	NB1L000603		03 28 01.891	+64 23 41.00	13.30	G_B	12.19	U	9.753	9.259	9.054	1.11	2.44
26	J034458.8+634439	J03445843+6344327	NB1E000050		03 44 58.433	+63 44 32.71	14.21	G_B	13.33	U	9.658	9.015	8.786	0.88	3.67
27	J034857.2+785910	J03485943+7859114	NAGP000513		03 48 59.436	+78 59 11.44	13.49	G_B	12.97	U	10.196	9.689	9.508	0.52	2.78
28 ‡	J040745.1+875030	J04073943+8750250	NAA5000047	BD+87 28	04 07 39.437	+87 50 25.00	11.51	T	10.72	T	9.253	8.865	8.762	0.79	1.47
29	J041128.6+754422	J04112810+7544231	NAEJ000542		04 11 28.109	+75 44 23.17	13.72	G_B	12.60	U	9.464	8.804	8.608	1.12	3.13
30	J041244.9+612123	J04124477+6121201	NASI000025		04 12 44.771	+61 21 20.17	15.94	G_B	14.37	U	9.995	9.417	9.183	1.57	4.37
31	J041641.4+613848	J04164046+6138443	NATF000004		04 16 40.465	+61 38 44.39	14.69	G_B	13.62	U	10.615	10.02	9.827	1.07	3.00
32 ‡	J043208.0+811627	J04321010+8116139	NAFQ000210	TYC 4522-713-1	04 32 10.108	+81 16 13.91	12.25	T	11.14	T	9.140	8.564	8.414	1.11	2.00
33 ‡	J044912.7+773719	J04491531+7737122	NADY000313	TYC 4515-156-1	04 49 15.318	+77 37 12.23	11.72	T	10.92	T	9.520	9.148	9.030	0.81	1.40
34	J045741.8+683548	J04574103+6835478	NAX6000074		04 57 41.031	+68 35 47.88	13.55	G_B	12.61	U	9.227	8.574	8.412	0.98	3.39
35	J045808.2+790813	J04580667+7908072	NAFX000397		04 58 06.670	+79 08 07.30	14.15	G_J	12.88	U	9.657	9.000	8.830	(1.66)	3.22
36	J050248.7+735215	J05024924+7352143	NAF0000068		05 02 49.245	+73 52 14.34	13.35	G_B	11.89	U	9.348	8.726	8.550	1.46	2.54
37 ‡	J050642.4+745604	J05063831+7456010	NAF1000019	TYC 4354-433-1	05 06 38.314	+74 56 01.08	11.44	T	10.80	T	9.416	9.127	9.048	0.64	1.38
38 ‡	J053459.0+652146	J05345873+6521435	NAQ7000082	StKM 1-570	05 34 58.736	+65 21 43.53	12.70	G_J	11.55	U	8.709	8.037	7.841	(1.42)	2.84
39	J061330.8+820121	J06133128+8201270	N74P000117		06 13 31.287	+82 01 27.04	16.12	G_B	14.57	U	10.090	9.507	9.258	1.55	4.48
40 ‡	J061946.4+771933	J06194548+7719330	N76R000372		06 19 45.489	+77 19 33.04	13.47	G_B	12.71	U	(10.245)	9.651	9.523	0.76	(2.46)
41 ‡	J062558.2+822124	J06260175+8221277	N74T000027	BD+82 160	06 26 01.753	+82 21 27.76	11.51	T	10.78	T	9.277	8.874	8.771	0.73	1.50
42	J063405.9+770040	J06340499+7700395	N773000344	TYC 4529-1687-1	06 34 04.991	+77 00 39.52	11.05	T	10.45	T	9.179	8.831	8.756	0.61	1.27
43 ‡	J064241.4+880442	J06423375+8804441	N741000014	BD+88 28	06 42 33.754	+88 04 44.16	11.53	T	10.83	T	9.560	9.188	9.106	0.70	1.27
44	J070350.7+831346	J07035520+8313387	N74Q000405	BD+83 171p	07 03 55.208	+83 13 38.78	11.39	T	10.79	T	9.510	9.249	9.150	0.60	1.28
45	J071537.9+764648	J07153237+7647084	N76Z000045	TYC 4526-474-1	07 15 32.373	+76 47 08.40	11.26	T	10.65	T	9.594	9.318	9.216	0.61	1.06
46 ‡	J071743.1+764416	J07174240+7644203	N76W000013	TYC 4526-646-1	07 17 42.401	+76 44 20.39	11.96	T	11.19	T	9.477	9.017	8.907	0.78	1.71
47 ‡	J075427.0+780633	J07543054+7806452	N7AC000093	NR Cam	07 54 30.541	+78 06 45.23	11.74	T	10.98	T	9.399	8.954	8.870	0.76	1.58
48	J075556.7+832310	J07555396+8323049	N74L003701	GJ 1101	07 55 53.968	+83 23 04.99	14.36	G_J	13.52	U	8.744	8.144	7.912	[0.84]	4.77
49 ‡	J083407.4+791449	J08340581+7914458	N7B2000444	TYC 4543-837-1	08 34 05.814	+79 14 45.86	11.50	T	10.69	T	9.079	8.640	8.513	0.81	1.61
50 ‡	J085353.7+870708	J08535198+8707127	N74F000137	BD+87 64	08 53 51.989	+87 07 12.72	11.61	T	10.99	T	9.129	8.766	8.619	0.63	1.86
51	J092654.8+812751	J09265323+8127469	N79W000299		09 26 53.231	+81 27 46.90	13.36	G_B	12.30	U	9.616	8.943	8.826	1.06	2.68
52	J093852.0+852625	J09385059+8526172	N75H000195	BD+86 136	09 38 50.597	+85 26 17.22	11.32	T	10.75	T	9.502	9.109	9.041	0.57	1.25
53	J102225.9+752828	J10222618+7528312	N78Q000124	TYC 4542-1861-1	10 22 26.188	+75 28 31.29	11.95	T	11.18	T	9.443	8.931	8.815	0.76	1.74
54	J112114.0+824715	J11211194+8247172	N752000249	FBS 1117-830	11 21 11.945	+82 47 17.22	16.04	G_B	14.03	U	10.263	9.645	9.418	2.01	3.77

[8] This source is the companion to TYC 4500-1549-1, which turns out to be the brighter component of a visual binary reported by Tachihara et al. (2005). See Appendix D for details.

Table 1. Continued.

#	X-ray name 1RXS	IR name 2MASS	GSC II name	Other name	α (2000) (h m s)	δ (2000) (° ′ ″)	B (mag)	Ref.	V (mag)	Ref.	J (mag)	H (mag)	K_s (mag)	B–V [a] (mag)	V–J [b] (mag)
55 ‡	J113533.7+825920	J11353465+8259217	N753000234	TYC 4632-1171-1	11 35 34.655	+82 59 21.71	11.91	T	11.15	T	(8.939)	8.280	8.091	0.76	(2.21)
56 ‡	J123048.8+832257	J12303982+8323081	N3YZ000121	TYC 4633-1518-1	12 30 39.826	+83 23 08.18	12.39	T	11.70	T	10.604	10.256	10.184	0.69	1.10
57 ‡	J123205.6+841719	J12320278+8417191	N3YW000031		12 32 02.788	+84 17 19.14	13.31	G_B	12.35	U	9.975	9.319	9.162	0.96	2.38
58	J125912.7+743529	J12591320+7435207	N41R000077	TYC 4407-145-1	12 59 13.208	+74 35 20.77	11.34	T	10.78	T	9.475	9.127	9.035	0.56	1.31
59	J130433.9+882441	J13033881+8824072	N3Y9000244	TYC 4645-293-1	13 03 38.815	+88 24 07.23	12.11	T	11.48	T	10.501	10.268	10.197	0.64	0.98
60	J134050.7+792553	J13405128+7925550	N44S000296		13 40 51.282	+79 25 55.01	12.83	G_B	11.88	U	9.519	8.919	8.776	0.95	2.36
61	J135117.4+770307	J13511765+7703008	N40K000009		13 51 17.653	+77 03 00.81	14.54	G_B	13.43	U	10.287	9.653	9.496	1.11	3.14
62	J135337.0+773708	J13533877+7737083	N450000288	NLTT 35712 ?	13 53 38.772	+77 37 08.30	14.14	G_J	13.40	U	8.635	8.056	7.795	(1.42)	4.76
63	J141447.2+680442	J14144719+6804420	N4PK000120	TYC 4403-57-1	14 14 47.196	+68 04 42.05	11.42	T	10.83	T	9.404	9.146	9.072	0.58	1.43
64	J143642.7+613935	J14363900+6139519	N4KS000228		14 36 39.010	+61 39 51.93	12.82	G_B	12.19	U	9.882	9.388	9.250	0.63	2.31
65	J145154.8+604616	J14515684+6046205	N4LA000311	TYC 4180-1135-1	14 51 56.842	+60 46 20.60	11.79	T	11.16	T	9.717	9.315	9.199	0.63	1.44
66 ‡	J145228.8+714026	J14523175+7140132	N4OX000133	TYC 4413-1113-1	14 52 31.757	+71 40 13.20	11.81	T	11.22	T	9.720	9.381	9.274	0.60	1.50
67	J150043.3+682234	J15004194+6822327	N4QK000131	TYC 4411-1400-1	15 00 41.946	+68 22 32.75	12.60	T	11.77	T	10.214	9.730	9.627	0.84	1.56
68	J154457.5+793054	J15445657+7931016	N455000017	TYC 4563-1484-1	15 44 56.576	+79 31 01.63	11.87	T	11.26	T	10.007	9.546	9.438	0.62	1.25
69 ‡	J154522.2+751500	J15452354+7514548	N431000294		15 45 23.546	+75 14 54.84	14.71	G_B	13.32	U	9.725	9.142	8.897	1.39	3.60
70	J155547.5+684014	J15554725+6840138	N4MO000164		15 55 47.250	+68 40 13.86	13.70	G_B	11.94	U	8.593	7.962	7.752	1.76	3.35
71	J160438.3+702212	J16043736+7022142	N4LX003834		16 04 37.363	+70 22 14.26	12.34	G_J	11.30	U	8.793	8.180	8.002	[1.04]	2.51
72	J160820.6+700353	J16081945+7003468	N4MQ000416	TYC 4422-1970-1	16 08 19.455	+70 03 46.84	11.63	T	10.96	T	9.548	9.116	9.010	0.67	1.41
73	J161939.9+765515	J16193872+7655165	N434000404		16 19 38.730	+76 55 16.58	13.82	G_B	12.59	U	9.357	8.719	8.511	1.23	3.24
74	J162708.9+662620	J16270823+6626144	N4MK000366	TYC 4196-1624-1	16 27 08.233	+66 26 14.42	12.32	T	11.42	T	10.107	9.705	9.618	0.89	1.31
75	J162939.7+620505	J16293983+6205131	N4HU000060	BD+62 1487	16 29 39.838	+62 05 13.14	11.53	T	10.84	T	8.906	8.454	8.310	0.69	1.93
76 ‡	J163747.2+723937	J16374587+7239423	N42S000309	TYC 4426-221-1	16 37 45.880	+72 39 42.39	12.05	T	11.34	T	10.176	9.787	9.650	0.72	1.16
77	J165315.4+701554	J16531433+7015596	N4LJ000266	TYC 4423-1336-1	16 53 14.334	+70 15 59.68	11.42	T	10.74	T	9.338	8.898	8.754	0.68	1.40
78 ‡	J170526.8+743600	J17052388+7436042	N43J000280	TYC 4427-715-1	17 05 23.886	+74 36 04.28	11.61	T	10.93	T	9.713	9.357	9.285	0.68	1.22
79 ‡	J171928.8+652227	J17192868+6522298	N4EF000088	TYC 4206-459-1	17 19 28.682	+65 22 29.81	12.15	T	11.40	T	10.034	9.602	9.516	0.75	1.37
80	J173451.2+784419	J17345173+7844186	N440000010		17 34 51.734	+78 44 18.66	14.25	G_B	12.90	U	9.495	8.773	8.621	1.35	3.41
81 ‡	J174104.6+842458	J17410836+8424552	N3ZO000437		17 41 08.370	+84 24 55.29	14.65	G_B	13.09	U	(10.386)	(9.859)	(9.466)	1.56	(2.71)
82	J175140.9+730509	J17514141+7305112	N43C000018	TYC 4436-501-1	17 51 41.415	+73 05 11.24	11.41	T	10.84	T	9.736	9.419	9.340	0.57	1.10
83	J175614.1+680707	J17561374+6807116	N41S000411		17 56 13.748	+68 07 11.65	13.77	G_B	13.19	U	10.481	9.888	9.775	0.58	2.71
84 ‡	J175910.1+584300	J17591035+5842594	N4F5000235	TYC 3914-118-1	17 59 10.359	+58 42 59.49	11.63	T	11.01	T	9.465	9.073	8.981	0.63	1.55
85	J180643.4+682200	J18064367+6822031	N0U8000324		18 06 43.679	+68 22 03.19	14.38	G_J	12.85	G_V	9.685	9.064	8.845	(1.47)	(3.17)
86	J181048.9+701601	J18104997+7016100	N0UL000431	TYC 4433-597-1	18 10 49.975	+70 16 10.07	11.28	T	10.63	T	9.183	8.810	8.679	0.65	1.45
87 ‡	J181610.9+585539	J18161159+5855420	N13Y000374	TYC 3916-1907-1	18 16 11.596	+58 55 42.10	11.24	T	10.57	T	8.945	8.498	8.383	0.67	1.63
88	J183552.8+800536	J18355181+8005394	N0YQ000010	GJ 4068	18 35 51.818	+80 05 39.48	14.36	G_J	13.27	U	8.989	8.419	8.163	(1.32)	4.28
89 ‡	J183627.4+715311	J18362702+7153157	N0UK000328	TYC 4438-627-1	18 36 27.025	+71 53 15.76	11.82	T	11.14	T	9.644	9.256	9.149	0.68	1.50
90	J183810.6+682424	J18381041+6824221	N1HR000382		18 38 10.414	+68 24 22.14	14.99	G_B	14.41	U	11.847	11.285	11.144	0.58	2.56
91 ‡	J184830.1+642330	J18482942+6423281	N14N000211	TYC 4223-399-1	18 48 29.427	+64 23 28.12	12.25	T	11.31	T	9.094	8.557	8.447	0.94	2.22
92 ‡	J185131.1+584258	J18513099+5842579	N16J000101	TYC 3930-1709-1	18 51 30.991	+58 42 57.98	11.76	T	10.98	T	9.442	9.079	8.984	0.78	1.54
93	J190445.7+700628	J19044518+7006293	N1HM000270	TYC 4435-516-1	19 04 45.189	+70 06 29.33	11.79	T	11.18	T	10.02	9.673	9.584	0.61	1.16
94	J190921.0+562658	J19092137+5626548	N16E000589	TYC 3928-1195-1	19 09 21.372	+56 26 54.87	11.23	T	10.65	T	9.627	9.292	9.219	0.58	1.02
95	J191412.4+615122	J19141236+6151223	N149000119		19 14 12.369	+61 51 22.39	14.21	G_B	12.94	U	10.701	10.097	9.932	1.28	2.24
96	J191519.4+660830	J19151619+6608517	N1I0000495	TYC 4229-1836-1	19 15 16.198	+66 08 51.77	11.25	T	10.69	T	9.652	9.337	9.274	0.56	1.04
97	J192104.3+561940	J19210447+5619420	N15Z000573	TYC 3929-1500-1	19 21 04.470	+56 19 42.09	11.45	T	10.85	T	9.692	9.402	9.346	0.60	1.16
98	J192127.4+611208	J19212759+6112042	N15A000164		19 21 27.599	+61 12 04.27	13.26	G_B	12.45	U	10.39	9.901	9.739	0.81	2.06
99	J192215.6+673918[9]	J19221289+6739053	N1IX000468	TYC 4444-1831-1	19 22 12.897	+67 39 05.34	12.37	T	11.67	T	9.510	8.924	8.825	0.70	2.16
100 ‡	J193003.3+663021	J19300213+6630231	N1I2000502	HD 184481	19 30 02.135	+66 30 23.16	9.78	T	9.25	T	8.118	7.845	7.803	0.52	1.13
101	J193026.5+580427	J19302663+5804352	N154000033	TYC 3929-592-1	19 30 26.637	+58 04 35.21	11.53	T	10.55	T	8.393	7.903	7.696	0.98	2.16
102 ‡	J193124.1+672401	J19312400+6723567	N1IX000266	TYC 4242-151-1	19 31 24.007	+67 23 56.76	13.09	T	12.77	T	(10.367)	10.052	(9.827)	0.32	(2.40)
103 ‡	J193141.7+641951	J19314063+6419520	N1HU000422	TYC 4238-1049-1	19 31 40.632	+64 19 52.02	11.01	T	10.37	T	8.831	8.434	8.349	0.63	1.54
104	J193231.8+565905	J19323041+5659071	N12G000059	TYC 3929-1760-1	19 32 30.418	+56 59 07.20	12.29	T	11.62	T	9.295	8.765	8.630	0.67	2.33
105 ‡	J193958.2+851032	J19400095+8510230	N0U3000120	TYC 4652-781-1	19 40 00.952	+85 10 23.03	12.24	T	11.44	T	10.009	9.542	9.460	0.80	1.43
106	J194206.0+654655	J19420596+6546497	N1I7007118	TYC 4242-1123-1	19 42 05.966	+65 46 49.75	11.50	T	10.81	T	9.540	9.157	9.053	0.69	1.27
107	J194616.6+701413	J19461559+7014135	N1J2000362		19 46 15.595	+70 14 13.58	14.71	G_B	13.22	U	10.224	9.585	9.402	1.49	2.99
108	J195139.1+710122	J19513766+7101255	N1ID000252		19 51 37.660	+71 01 25.53	13.87	G_B	12.74	U	10.128	9.570	9.416	1.13	2.61
109 ‡	J195542.3+663207	J19554228+6632051	N1HY000096	TYC 4243-473-1	19 55 42.283	+66 32 05.19	13.08	T	11.79	T	9.248	8.666	8.453	1.28	2.54
110 ‡	J195758.2+664253	J19575836+6642514	N1HY000042	TYC 4243-597-1	19 57 58.365	+66 42 51.46	11.14	T	10.22	T	8.806	8.402	8.281	0.92	1.41

[9] The X-ray emission seems to be produced from the galaxy 2MASX 19221485+6739143. See Appendix D for details.

Table 1. Continued.

#	X-ray name 1RXS	IR name 2MASS	GSC II name	Other name	α (2000) (h m s)	δ (2000) (° ′ ″)	B (mag)	Ref.	V (mag)	Ref.	J (mag)	H (mag)	K_s (mag)	B–V [a] (mag)	V–J [b] (mag)
111	J200110.8+743025	J20011185+7430305	N0V3000572		20 01 11.856	+74 30 30.57	15.61	G_B	14.08	U	10.821	10.145	9.957	1.53	3.26
112	J200245.4+592015	J20024462+5920162	N124000775	TYC 3948-1516-1	20 02 44.627	+59 20 16.27	11.57	T	10.69	T	8.792	8.312	8.185	0.88	1.90
113	J200348.4+642542	J20034781+6425471	N1JN000198	TYC 4240-978-1	20 03 47.812	+64 25 47.12	12.49	T	11.29	T	8.267	7.659	7.486	1.20	3.02
114 *	J201424.6+660521	J20142610+6605199	N1JT000259	TYC 4244-322-1	20 14 26.110	+66 05 19.95	12.25	T	11.58	T	9.688	9.150	9.033	0.67	1.89
115 *	J202513.8+733638	J20251540+7336332	N0UQ000374	TYC 4459-83-1	20 25 15.402	+73 36 33.26	11.51	T	10.69	T	9.128	8.731	8.639	0.82	1.56
116	J203549.9+594930	J20354953+5949379	N1F8000090		20 35 49.539	+59 49 37.95	13.75	G_B	12.37	U	9.883	9.386	9.249	1.38	2.48
117	J203638.5+553811	J20363836+5538141	N11P000076		20 36 38.364	+55 38 14.14	13.59	G_J	12.28	G_V	9.978	9.362	9.177	(1.31)	(2.30)
118 *	J203813.1+692413	J20381376+6924127	N1JB000834	GSC 04451-00172	20 38 13.769	+69 24 12.78	14.11	G_B	13.42	U	10.559	9.907	9.757	0.69	2.86
119 ‡	J203857.5+580452	J20385772+5804567	N1E1000002		20 38 57.728	+58 04 56.74	15.04	G_B	14.22	U	11.424	10.914	10.79	0.82	2.80
120 ‡	J203903.6+640707	J20390451+6407067	N1JQ000885	TYC 4254-18-1	20 39 04.512	+64 07 06.79	10.46	T	9.96	T	8.713	8.356	(8.508)	0.51	1.25
121	J205405.4+601811	J20540505+6018041	N1FG000257		20 54 05.054	+60 18 04.14	15.86	G_B	13.71	G_V	10.098	9.450	9.256	(2.15)	5.22
122 *	J210419.0+750359	J21042093+7504049	N0XV000343	TYC 4586-348-1	21 04 20.936	+75 04 04.97	11.81	T	11.15	T	9.804	9.404	9.325	0.66	1.35
123 ‡	J210444.0+522326	J21044434+5223256	N30J000168	GSC 03600-00513	21 04 44.340	+52 23 25.63	12.12	G_B	11.47	U	10.297	9.972	9.885	0.65	1.17
124 ‡	J210751.6+690923	J21075194+6909234	N1JE000111		21 07 51.942	+69 09 23.46	14.84	G_B	14.27	U	11.343	10.649	10.499	0.57	2.92
125 ‡	J211000.9+603644	J21100200+6036455	N1FD000400	TYC 4248-1247-1	21 10 02.006	+60 36 45.55	12.56	T	11.81	T	10.409	10.08	9.976	0.75	1.40
126 *	J211024.8+704600	J21102448+7045575	N1JH007278	TYC 4464-1372-1	21 10 24.483	+70 45 57.60	11.77	T	10.95	T	9.396	8.987	8.899	0.82	1.55
127	J211114.9+614436	J21111668+6144388	N1F6000070	TYC 4248-411-1	21 11 16.685	+61 44 38.81	12.49	T	11.71	T	10.124	9.720	9.629	0.78	1.59
128	J211232.5+741227	J21123576+7412339	N0WW000208	TYC 4473-229-1	21 12 35.768	+74 12 33.99	12.46	T	11.77	T	10.191	9.815	9.709	0.70	1.58
129	J211627.5+575501	J21162559+5754571	N1DY000213	TYC 3961-84-1	21 16 25.596	+57 54 57.11	11.85	T	11.19	T	10.100	9.770	9.688	0.66	1.09
130	J212606.8+555026	J21260610+5550242	N1AN000243	TYC 3970-530-1	21 26 06.103	+55 50 24.26	12.12	T	11.42	T	9.316	8.764	8.662	0.70	2.10
131 ‡	J212929.0+621859	J21292533+6218582	N1EN000408	TYC 4253-1617-1	21 29 25.338	+62 18 58.23	12.16	T	11.47	T	9.684	9.141	8.965	0.68	1.79
132 *	J213253.9+703751	J21325388+7037436	N1G6000228	GSC 04465-01410	21 32 53.889	+70 37 43.65	13.51	G_B	12.61	U	10.054	9.416	9.285	0.90	2.56
133 *, ‡	J213749.2+803228	J21374757+8032311	N0YD000068	TYC 4607-461-1	21 37 47.573	+80 32 31.15	12.48	T	11.54	T	9.147	8.554	8.396	0.94	2.39
134 ‡	J214719.8+611618	J21471905+6116173	N1EL000789		21 47 19.051	+61 16 17.39	12.79	G_B	11.83	U	10.221	9.692	9.642	0.96	1.61
135 ‡	J214909.0+591341	J21490916+5913348	N1B9000224		21 49 09.163	+59 13 34.81	13.68	G_B	11.99	U	9.937	9.289	9.099	1.67	2.05
136	J220214.4+562800	J22021462+5628051	N1BX000508		22 02 14.625	+56 28 05.11	13.99	G_B	13.06	U	10.149	9.535	9.378	0.93	2.91
137 *	J220524.6+655219	J22052579+6552198	N1GT000629	TYC 4275-1998-1	22 05 25.799	+65 52 19.87	11.66	T	11.08	T	9.690	9.321	9.252	0.58	1.39
138	J220639.1+613425	J22063973+6134269	N1B7000261		22 06 39.736	+61 34 26.93	14.67	G_B	13.47	U	9.962	9.297	9.088	0.80	3.51
139	J221055.6+632339	J22105525+6323533	N1GG000302	STF 2879C	22 10 55.258	+63 23 53.33	11.85	G_B	11.10	G_V	11.109	10.977	10.893	[0.75]	(-0.01)
140 ‡	J221712.3+545100	J22171260+5451062	N1B3000489		22 17 12.610	+54 51 06.29	14.09	G_J	12.56	G_V	(11.637)	(11.077)	10.964	(1.53)	(0.92)
141	J221828.6+695134	J22182783+6951402	N1H9000216	WW Cep	22 18 27.836	+69 51 40.23	11.77	T	10.77	T	8.957	8.515	8.385	0.99	1.81
142	J222257.8+744322	J22225898+7443211	N0X8000186		22 22 58.986	+74 43 21.12	13.91	G_B	12.85	U	10.41	9.847	9.701	1.14	2.44
143	J222405.9+881244	J22240615+8812498	N0SI000264		22 24 06.158	+88 12 49.81	14.28	G_J	13.62	U	10.167	9.495	9.311	[0.66]	3.45
144 ‡	J222923.1+674923	J22292260+6749164	N1HA000396	TYC 4476-1415-1	22 29 22.601	+67 49 16.45	11.60	T	11.03	T	9.376	8.888	8.822	0.56	1.65
145	J223613.9+703206	J22361592+7032042	N1H7000172	TYC 4480-965-1	22 36 15.929	+70 32 04.28	11.61	T	10.69	T	8.546	8.030	7.824	0.92	2.14
146 ‡	J224000.2+642310	J22400038+6423130	N195000284		22 40 00.384	+64 23 13.04	14.10	G_J	13.34	U	9.633	9.037	8.784	(1.46)	3.71
147 ‡	J224917.6+522634	J22491811+5226360	N17N000016	TYC 3633-2139-1	22 49 18.111	+52 26 36.05	12.05	T	10.62	T	8.692	8.091	7.961	1.43	1.93
148 ⋆	J225059.7+781435	J22510533+7814216	N0YH000446		22 51 05.331	+78 14 21.63	13.00	G_B	12.21	U	10.46	10.143	10.098	0.79	1.75
149 ‡	J225641.1+593031	J22564095+5930368	N1DH000105	TYC 3997-191-1	22 56 40.956	+59 30 36.87	12.07	T	11.40	T	10.002	9.695	9.563	0.68	1.40
150	J225855.7+673117	J22585395+6731186	N1FU000550		22 58 53.957	+67 31 18.66	12.89	G_B	11.95	G_V	10.397	10.046	9.915	(0.73)	2.20
151	J230604.0+635538	J23060482+6355339	N1A1000396	GJ 9809	23 06 04.827	+63 55 33.95	12.15	T	10.93	T	7.815	7.167	6.977	1.23	3.12
152 ⋆, ‡	J230822.7+790829	J23082206+7908236	N0YA000504		23 08 22.063	+79 08 23.69	13.99	G_B	12.49	U	10.084	9.511	9.271	1.50	2.40
153 *, ⋆, ‡	J231616.5+784156	J23161828+7841558	N0YA000035	TYC 4605-170-1	23 16 18.287	+78 41 55.90	12.69	T	11.75	T	9.535	9.002	8.826	0.94	2.22
154 ‡	J232209.7+575626	J23220944+5756296	N1D1000255		23 22 09.444	+57 56 29.63	14.65	G_B	13.36	U	9.939	9.293	9.088	1.29	3.43
155 ‡	J232346.4+620620	J23234618+6206193	N1A6000239		23 23 46.183	+62 06 19.33	15.15	G_B	11.94	U	9.758	9.262	9.099	4.26	2.18
156 ⋆, ‡	J232647.5+770304	J23264947+7703062	N0WV000748		23 26 49.478	+77 03 06.22	14.33	G_J	12.95	G_V	10.269	9.573	9.416	(1.38)	(2.68)
157 ⋆, ‡	J233702.3+751625	J23370398+7516206	N0WQ000534	TYC 4602-862-1	23 37 03.981	+75 16 20.67	11.51	T	10.83	T	9.519	9.160	9.087	0.68	1.31
158 ⋆	J234920.7+783000	J23492002+7829467	N0WG000199	TYC 4606-1905-1	23 49 20.027	+78 29 46.73	12.30	T	11.53	T	9.767	9.278	9.151	0.76	1.76
159 ‡	J235502.1+541516	J23550237+5415171	N176000076		23 55 02.377	+54 15 17.13	13.25	G_B	12.39	G_V	10.406	9.812	9.638	(1.20)	2.63
	Stars only cross-identified with a source of the XMM-Newton catalog:														
160 ⋆, ‡	184257	J22372780+7515256	N0XD010154	[KP93] 2-43	22 37 27.806	+75 15 25.62	18.86	G_B	16.44	U	11.289	10.202	9.854	2.42	5.15
161	186704	J23025635+5835565	N1DJ000620	LSPM J2302+5835	23 02 56.352	+58 35 56.55	14.63	G_J	13.70	U	9.999	9.373	9.150	(1.12)	3.70
162 ‡	189583	J23364300+6204331	N19Y000541		23 36 43.006	+62 04 33.15	12.57	G_B	11.64	U	10.158	9.807	9.711	0.93	1.48
	Stars in Tachihara et al. (2005) not selected using our multivariate analysis:														
163 *, ⋆	J000002.5+733942	J00000208+7339463	NACK000433	TYC 4306-1190-1	00 00 02.089	+73 39 46.37	13.00	T	11.93	T	9.779	9.261	9.094	1.06	2.15

Table 1. Continued.

#	X-ray name 1RXS	IR name 2MASS	GSC II name	Other name	α (2000) (h m s)	δ (2000) (° ′ ″)	B (mag)	Ref.	V (mag)	Ref.	J (mag)	H (mag)	K_s (mag)	B–V [a] (mag)	V–J [b] (mag)
164 *, ⋆, ‡	J000142.0+773057	J00014256+7731061	NACG000699	TYC 4496-2286-1	00 01 42.564	+77 31 06.19	13.15	T	12.03	T	10.037	9.451	9.281	1.12	1.99
165 *, ⋆	J004621.1+741251	J00462233+7412489	NADB000010	GSC 04307-01640	00 46 22.335	+74 12 48.96	13.46	G_B	12.72	U	11.432	11.208	11.079	0.74	1.29
166 *	J010117.1+713114	J01011729+7131126	NABO000533	TYC 4304-1407-1	01 01 17.299	+71 31 12.65	11.73	T	10.73	T	8.947	8.453	8.353	1.00	1.78
167 *, ‡	J010929.0+683916	J01092883+6839146	NB0A000048	V1065 Cas	01 09 28.832	+68 39 14.70	11.44	T	10.32	T	7.637	7.071	6.923	1.12	2.68
168 *	J011934.6+713028	J01193440+7130318	NB04000593	TYC 4305-1893-1	01 19 34.408	+71 30 31.81	12.12	T	11.39	T	(10.347)	(9.984)	(9.900)	0.73	(1.04)
169 *, ‡	J013925.5+701853	J01392593+7018500	NB06000531	TYC 4314-1757-1	01 39 25.935	+70 18 50.05	10.80	T	10.16	T	8.451	8.002	7.882	0.63	1.71
170 *, ‡	J022613.0+681127	J02261282+6811329	NB20000348	GSC 04312-00734	02 26 12.829	+68 11 32.96	13.17	G_B	12.42	U	10.721	10.373	10.242	0.75	1.70
171 *	J200549.1+770550	J20054896+7705530	N0Y0000647	TYC 4589-2335-1	20 05 48.967	+77 05 53.04	12.66	T	11.08	T	8.633	7.985	7.816	1.59	2.45
172 *	J201151.4+783434	J20115370+7834374	N0ZB000125	TYC 4589-369-1	20 11 53.700	+78 34 37.46	12.49	T	11.71	T	9.913	9.435	9.266	0.78	1.80
173 *	J201948.8+653408	J20194855+6534095	N1JZ000119	GSC 04241-01092	20 19 48.556	+65 34 09.56	11.79	G_B	11.19	U	10.571	10.186	10.088	0.60	0.61
174 *	J202026.6+780717	J20202937+7807222	N0ZB000672	TYC 4589-1101-1	20 20 29.379	+78 07 22.26	11.10	T	10.34	T	8.965	8.516	8.434	0.77	1.38
175 *, ‡	J203341.8+705321	J20334380+7053188	N1JA000022	TYC 4451-1270-1	20 33 43.801	+70 53 18.86	13.43	T	11.65	T	10.215	9.675	9.621	1.78	1.44
176 *	J204327.6+711546	J20432832+7115467	N1J5000308	TYC 4455-856-1	20 43 28.322	+71 15 46.77	12.70	T	12.27	T	10.79	10.537	10.473	0.44	1.48
177 *	J205312.2+792031	J20531202+7920218	N0ZJ000194	GSC 04594-01127	20 53 12.024	+79 20 21.82	13.78	G_B	12.89	U	10.100	9.565	9.406	0.89	2.79
178 *, ‡	J205607.9+651033	J20560940+6510312	N1KG000089	TYC 4255-314-1	20 56 09.407	+65 10 31.25	10.80	T	10.35	T	9.436	9.176	9.090	0.44	0.91
179 *	J211127.5+761435	J21112933+7614290	N0Y6000103	TYC 4586-1090-1	21 11 29.335	+76 14 29.02	12.45	T	11.47	T	10.192	9.735	9.692	0.98	1.28
180 *	J211143.9+685428	J21114388+6854231	N1JE000286	TYC 4460-1614-1	21 11 43.890	+68 54 23.13	11.19	T	10.58	T	9.455	9.144	9.059	0.60	1.13
181 *	J214258.6+803021	J21425760+8030197	N0YD000086	TYC 4607-611-1	21 42 57.600	+80 30 19.75	12.03	T	11.47	T	10.016	9.676	9.582	0.56	1.45
182 *, ⋆	J221107.9+791801	J22111127+7917599	N0YI000354	GSC 04608-01986	22 11 11.277	+79 17 59.98	14.24	G_B	13.81	U	10.329	9.737	9.558	0.43	3.48
183 *	J221158.7+681953	J22115779+6819524	N1GX000280	TYC 4463-818-1	22 11 57.798	+68 19 52.46	12.50	T	11.47	T	9.763	9.208	9.093	1.03	1.71
184 *, ‡	J222706.6+652127	J22270525+6521313	N1GU000092	GSC 04272-00174	22 27 05.254	+65 21 31.33	13.75	G_B	13.36	U	10.822	10.323	10.212	0.39	2.54
185 *	J223345.1+703321	J22334483+7033181	N1H7000161	TYC 4480-917-1	22 33 44.839	+70 33 18.19	12.97	T	11.16	T	8.508	7.817	7.616	1.81	2.65
186 *, ⋆	J223956.5+774934	J22395815+7749394	N0WM000002	TYC 4604-743-1	22 39 58.155	+77 49 39.44	12.47	T	11.94	T	10.007	9.530	9.387	0.53	1.93
187 *, ⋆	J225133.9+763549	J22513566+7635537	N0WL000167	TYC 4601-1894-1	22 51 35.668	+76 35 53.73	12.48	T	11.94	T	10.272	9.886	9.801	0.54	1.67
188 *, ⋆, ‡	J230043.2+772833	J23004455+7728385	N0WM000641	TYC 4605-2733-1	23 00 44.552	+77 28 38.54	11.76	T	11.42	T	9.409	8.977	8.840	0.34	2.01
189 *, ⋆	J230533.0+782238	J23053649+7822389	N0YA000256	GSC 04605-00268	23 05 36.498	+78 22 38.98	14.36	G_B	13.46	U	10.307	9.656	9.508	0.90	3.15
190 *, ⋆	J230757.5+765146	J23075657+7651478	N0WL000003	TYC 4601-938-1	23 07 56.571	+76 51 47.84	11.90	T	10.71	T	8.483	7.894	7.714	1.19	2.23
191 *, ⋆, ‡	J230942.9+735725	J23094349+7357152	N0XO000049	GSC 04489-00036	23 09 43.490	+73 57 15.29	14.10	G_B	12.94	U	9.757	9.081	8.906	1.16	3.18
192 *, ‡	J234342.3+684631	J23434195+6846271	N1FN000105	GSC 04479-00348	23 43 41.954	+68 46 27.12	13.46	G_B	12.78	U	10.892	10.364	10.249	0.68	1.89
193 *, ⋆	J235107.5+785802	J23511013+7858050	N0Y8000689	TYC 4610-1318-1	23 51 10.132	+78 58 05.00	12.39	T	11.34	T	9.572	9.184	9.041	1.04	1.77
	Other young field stars projected towards the CO Cepheus void and its surrounding, which also appear either in Guillout et al. (2010, sources labeled as G1 to G4) or in Frasca et al. (2018, sources labeled as F1 to F4):														
G1 ⋆, ‡	J000038.4+794037	J00004121+7940398	NAA8000377	BD+78 853	00 00 41.214	+79 40 39.82	10.98	T	10.25	T	8.922	8.612	8.523	0.72	1.33
G2 ⋆, ‡	J001337.6+770210	J00134052+7702104	NACH000519	TYC 4496-780-1	00 13 40.521	+77 02 10.49	10.35	T	9.78	T	8.208	7.758	7.570	0.57	1.57
G3 ⋆, ‡	J003804.2+790328	J00380610+7903206	NAG3000270	TYC 4500-1478-1	00 38 06.100	+79 03 20.66	11.19	T	10.29	T	8.763	8.323	8.213	0.91	1.53
G4 ⋆, ‡	J003941.9+790526	J00394018+7905307	NAG3000255	BD+78 19	00 39 40.184	+79 05 30.77	10.24	T	9.57	T	8.303	7.933	7.854	0.67	1.27
F1 ⋆, ‡	J210621.9+690645	J21062175+6906410	N0133022143	BD+68 1182	21 06 21.750	+69 06 41.00	10.75	T	10.15	T	9.011	8.754	8.703	0.60	1.14
F2 ⋆	J222316.2+774157	J22231885+7741577	N0103120435	BD+76 857a	22 23 18.857	+77 41 57.79	10.81	T	10.23	T	8.796	8.449	8.368	0.59	1.43
F3 ⋆, ‡	J232052.2+741359	J23205208+7414071	N0102321423	V395 Cep	23 20 52.090	+74 14 07.13	11.06	T	10.16	T	8.308	7.754	7.480	0.90	1.85
F4 ⋆	J235115.0+773934	J23511729+7739351	N0102103473	TYC 4606-740-1	23 51 17.294	+77 39 35.16	11.74	T	10.69	T	8.788	8.316	8.191	1.05	1.90

Notes associated to the recno. * Selected by both this study and the work of Tachihara et al. (2005); ⋆ Towards the CO Cepheus void; ‡ Multiple system (VB and SB).

Notes.

[a] The B–V color indexes are mainly in the Johnson-Cousins system. The bracketed values are the GCS II photographic color indexes, while the square-bracketed ones are the result of a mixture of both systems.

[b] The V–J color index values are put in parentheses if the V magnitude is not in the Johnson-Cousins system or if the J magnitude is an upper limit or a poor quality value.

References. T = Høg et al. (2000); U = Monet et al. (2003); Y = Zacharias et al. (2004); G = Lasker et al. (2008) where the suffix corresponds to their B, j, or V-band magnitude.

Table 3. Radial and rotational velocities, atmospheric parameters, and lithium equivalent widths derived for our targets during the survey.

#⋆	Instrument	H.J.D. [2400000+]	RV [km s^{-1}]	$v \sin i$ [km s^{-1}]	SpT	$T_{\rm eff}$ [K]	$\log g$ [cm^2 s^{-1}]	$[Fe/H]$ [dex]	$W_{\rm Li}$ [mÅ]	Note
1	IDS	55079.6090728	2.2 ± 0.3	17 ± 9	G1.5V	5827 ± 61	4.07 ± 0.12	−0.12 ± 0.11	72 ± 15	
2	IDS	55079.6255449	−75.7 ± 5.6	…	…	…	…	…	…	*RV*1 of an SB2 system with two M-type stars (M3.5V)
2	IDS	55079.6255449	10.6 ± 8.4	…	…	…	…	…	…	*RV*2 of an SB2 system with two M-type stars (M3.5V)
3	IDS	55079.5934565	−14.3 ± 2.0	15 ± 6	M4V	3397 ± 50	4.56 ± 0.15	−0.15 ± 0.11	18 ± 41	
4	SOPHIE	55101.4586116	…	…	…	…	…	…	…	W UMa-type star
5	IDS	55080.6417659	3.1 ± 2.4	38 ± 3	M4V	3397 ± 50	4.58 ± 0.16	−0.15 ± 0.11	9 ± 31	
5	IDS	55083.6659514	3.0 ± 1.3	15 ± 4	M5V	3339 ± 70	4.57 ± 0.18	−0.14 ± 0.11	45 ± 59	
6 c1	IDS	55084.6707247	−108.0 ± 4.5	…	…	…	…	…	…	*RV*1 of the SB2 system, strong Li line, Target = TYC 4500-1549-1
6 c1	IDS	55084.6707247	83.1 ± 4.6	…	…	…	…	…	…	*RV*2 of the SB2 system, strong Li line, Target = TYC 4500-1549-1
6 c1	IDS	55168.4497949	6.4 ± 1.2	…	…	…	…	…	…	Clear asymmetry in the CCF profile, strong Li line, Target = TYC 4500-1549-1
6 c1	IDS	55524.4605440	−94.0 ± 3.8	…	…	…	…	…	…	*RV*1 of the SB2 system, strong Li line, Target = TYC 4500-1549-1
6 c1	IDS	55524.4605440	72.8 ± 5.0	…	…	…	…	…	…	*RV*2 of the SB2 system, strong Li line, Target = TYC 4500-1549-1
6 c1	IDS	55524.4873016	−106.5 ± 3.8	…	…	…	…	…	…	*RV*1 of the SB2 system, strong Li line, Target = TYC 4500-1549-1
6 c1	IDS	55524.4873016	79.1 ± 4.7	…	…	…	…	…	…	*RV*2 of the SB2 system, strong Li line, Target = TYC 4500-1549-1
6 c2	IDS	55168.4497949	−9.1 ± 1.2	29 ± 7	M0V	3998 ± 189	4.63 ± 0.14	−0.16 ± 0.13	335 ± 55	
6 c2	IDS	55524.4873016	−8.4 ± 0.8	15 ± 8	M0V	3885 ± 58	4.63 ± 0.10	−0.08 ± 0.12	313 ± 48	
6 c3	IDS	55524.4605440	−1.7 ± 9.1	…	…	…	…	…	…	Target = *Gaia* DR2 5647079737331340 80
7	IDS	55081.7128973	−147.5 ± 2.0	43 ± 3	K1V	5011 ± 91	3.94 ± 0.23	−0.18 ± 0.11	18 ± 71	Double-peaked Hα profile (SB2?)
7	IDS	55081.7128973	∼80	…	…	…	…	…	…	Radial velocity of faint source in case of an SB2 system
8	IDS	55084.6961890	−83.0 ± 0.7	15 ± 9	K5III	3833 ± 78	2.84 ± 0.44	−0.11 ± 0.11	3 ± 41	
9	IDS	55082.7141749	−17.6 ± 1.8	22 ± 6	M2V	3625 ± 62	4.63 ± 0.15	−0.12 ± 0.11	6 ± 65	
10	SOPHIE	55102.5221099	50.6 ± 0.6	…	…	…	…	…	…	*RV*1 of the SB2 system, blended peaks
10	SOPHIE	55102.5221099	21.5 ± 0.8	…	…	…	…	…	…	*RV*2 of the SB2 system, blended peaks
11	IDS	55079.6372917	−30.7 ± 0.6	…	…	…	…	…	…	*RV*1 of the SB2 system
11	IDS	55079.6372917	27.2 ± 6.3	…	…	…	…	…	…	*RV*2 of the SB2 system (small and blended peak)
11	IDS	56225.5137565	3.2 ± 0.7	18 ± 2	K0IV	4923 ± 108	3.58 ± 0.23	0.01 ± 0.11	36 ± 45	
12	IDS	55079.6563403	−20.6 ± 2.9	15 ± 2	M4V	3413 ± 112	4.59 ± 0.15	−0.14 ± 0.11	29 ± 39	
13	IDS	55080.7295766	−123.0 ± 7.1	…	…	…	…	…	…	*RV*1 of the SB2 system
13	IDS	55080.7295766	85.7 ± 7.7	…	…	…	…	…	…	*RV*2 of the SB2 system
13	IDS	55083.7103077	67.9 ± 8.2	…	…	…	…	…	…	*RV*1 of the SB2 system
13	IDS	55083.7103077	−109.5 ± 8.7	…	…	…	…	…	…	*RV*2 of the SB2 system
14	IDS	55079.7286600	−10.1 ± 1.9	15 ± 1	M3.5V	3563 ± 80	4.41 ± 0.24	−0.15 ± 0.11	8 ± 28	
15	IDS	55083.7314967	7.1 ± 1.0	21 ± 6	M0V	3912 ± 67	4.62 ± 0.15	−0.11 ± 0.10	37 ± 35	
16	IDS	55079.6711282	−7.3 ± 0.4	17 ± 3	K2V	5103 ± 59	4.27 ± 0.20	−0.10 ± 0.10	200 ± 32	
16	FOCES	55107.5866862	−6.23 ± 0.18	15.0 ± 1.9	K0V	5146 ± 56	4.50 ± 0.21	−0.03 ± 0.05	208 ± 30	
17	IDS	55079.6869501	−14.7 ± 0.3	15 ± 8	K0III-IV	5204 ± 91	3.58 ± 0.25	−0.09 ± 0.11	11 ± 23	
18	IDS	55079.7061001	58.0 ± 2.2	…	…	…	…	…	…	*RV*1 of the SB2 system
18	IDS	55079.7061001	−57.2 ± 4.1	…	…	…	…	…	…	*RV*2 of the SB2 system
19	SOPHIE	55102.5487604	60.335 ± 0.018	…	…	…	…	…	…	*RV*1 of the SB2 system
19	SOPHIE	55102.5487604	−72.950 ± 0.018	…	…	…	…	…	…	*RV*2 of the SB2 system
19	FOCES	55110.5642208	66.49 ± 0.46	…	…	…	…	…	…	*RV*1 of the SB2 system
19	FOCES	55110.5642208	−77.81 ± 0.44	…	…	…	…	…	…	*RV*2 of the SB2 system
20	IDS	55083.7504098	20.3 ± 2.6	…	…	…	…	…	…	*RV*1 of the SB2 system
20	IDS	55083.7504098	−41.3 ± 2.4	…	…	…	…	…	…	*RV*2 of the SB2 system
20	IDS	56225.5366156	22.6 ± 2.8	…	…	…	…	…	…	*RV*1 of the SB2 system
20	IDS	56225.5366156	−47.0 ± 3.5	…	…	…	…	…	…	*RV*2 of the SB2 system
21	IDS	55084.7172196	−10.9 ± 1.0	15 ± 15	M5V	3397 ± 50	4.56 ± 0.15	−0.15 ± 0.11	17 ± 36	
22	SOPHIE	55102.5667200	−10.284 ± 0.005	10.0 ± 1.0	K1V	5127 ± 121	4.55 ± 0.06	−0.06 ± 0.10	258 ± 12	
22	FOCES	55107.6229096	−10.38 ± 0.09	9.5 ± 1.0	K1V	5115 ± 59	4.55 ± 0.15	−0.02 ± 0.05	287 ± 24	
23	IDS	55084.7367683	30.4 ± 1.7	…	…	…	…	…	…	*RV*1 of an SB2 system with two M-type stars (M3.5V)
23	IDS	55084.7367683	−64.4 ± 1.6	…	…	…	…	…	…	*RV*2 of an SB2 system with two M-type stars (M3.5V)
24	IDS	55081.6962023	25.2 ± 2.4	15 ± 12	M2V	3607 ± 50	4.60 ± 0.16	−0.13 ± 0.11	31 ± 49	
25	IDS	55081.7295722	−22.2 ± 0.7	15 ± 1	K5V	4722 ± 129	4.00 ± 0.22	−0.04 ± 0.11	0 ± 28	
26	IDS	55084.7557299	3.2 ± 1.2	25 ± 7	M2V	3622 ± 55	4.56 ± 0.22	−0.05 ± 0.13	28 ± 81	
27	IDS	55082.7338377	−35.9 ± 0.6	17 ± 2	K1III	4809 ± 91	3.08 ± 0.22	−0.03 ± 0.11	56 ± 24	Hα faint double-peaked emission
28	SOPHIE	55101.6452849	−58.985 ± 0.019	…	…	…	…	…	…	*RV*1 of the SB2 system
28	SOPHIE	55101.6452849	59.685 ± 0.019	…	…	…	…	…	…	*RV*2 of the SB2 system
28	FOCES	55107.6445504	−74.43 ± 0.29	…	…	…	…	…	…	*RV*1 of the SB2 system

Table 3. Continued.

#⋆	Instrument	H.J.D. [2400000+]	RV [km s^{-1}]	$v \sin i$ [km s^{-1}]	SpT	$T_{\rm eff}$ [K]	$\log g$ [cm^2 s^{-1}]	$[Fe/H]$ [dex]	$W_{\rm Li}$ [mÅ]	Note
28	FOCES	55107.6445504	76.57 ± 0.41	…	…	…	…	…	…	*RV*2 of the SB2 system
29	IDS	55083.7657904	−7.2 ± 0.8	26 ± 10	M0V	3816 ± 79	4.65 ± 0.14	−0.11 ± 0.10	35 ± 58	
30	IDS	56226.6080778	−22.6 ± 4.9	34 ± 2	M4.5V	3436 ± 56	4.50 ± 0.33	−0.14 ± 0.11	37 ± 37	
31 c1	IDS	55524.5662608	−44.7 ± 0.5	15 ± 1	K1IV	4765 ± 62	2.83 ± 0.22	0.00 ± 0.11	11 ± 35	Target = *Gaia* DR2 475251432820143872
31 c2	IDS	55524.5662608	18.0 ± 0.7	25 ± 1	K7V	4363 ± 95	4.48 ± 0.17	−0.18 ± 0.12	59 ± 39	
32	SOPHIE	55102.5925771	−11.906 ± 0.013	15.0 ± 1.03	K3V	4845 ± 127	4.55 ± 0.07	0.01 ± 0.13	119 ± 10	SB1
32	FOCES	55107.6681762	7.53 ± 0.12	14.8 ± 0.5	K3V	4767 ± 111	4.37 ± 0.20	−0.03 ± 0.04	142 ± 16	SB1
33	SOPHIE	55102.6191246	…	…	…	…	…	…	…	Likely SB2 system composed of two fast rotators
33	FOCES	55107.6911711	…	117.5 ± 11.0	G5V	5483 ± 313	4.32 ± 0.31	−0.07 ± 0.17	207 ± 60	
33	FOCES	55110.5854832	…	120.1 ± 13.6	G3IV	5359 ± 361	4.24 ± 0.35	−0.04 ± 0.15	184 ± 56	
34	IDS	56225.6732600	6.3 ± 1.4	25 ± 7	M0V	3887 ± 61	4.64 ± 0.11	−0.10 ± 0.12	44 ± 107	
35	IDS	55524.5899614	−94.7 ± 0.6	19 ± 3	K7V	4172 ± 121	4.53 ± 0.17	−0.16 ± 0.12	104 ± 52	Double-peaked Hα profile (SB2?)
36	FOCES	55108.6540370	−7.19 ± 0.34	41.4 ± 2.5	K5V	4731 ± 238	4.59 ± 0.33	−0.05 ± 0.10	69 ± 27	
36	FOCES	55168.5676429	−8.5 ± 3.5	39.2 ± 3.7	K4V	4662 ± 271	4.59 ± 0.38	−0.06 ± 0.11	23 ± 38	
37 c1	SOPHIE	55101.6671374	−30.5 ± 0.2	…	…	…	…	…	…	*RV*1 of the SB2 system
37 c1	SOPHIE	55101.6671374	−63.7 ± 0.8	…	…	…	…	…	…	*RV*2 of the SB2 system
37 c1	IDS	55524.6197432	−48.4 ± 0.9	…	…	…	…	…	…	*RV*1 of the SB3 system
37 c1	IDS	55524.6197432	−105.7 ± 1.4	…	…	…	…	…	…	*RV*2 of the SB3 system
37 c1	IDS	55524.6197432	11.6 ± 9.1	…	…	…	…	…	…	*RV*3 of the SB3 system
37 c2	IDS	55524.6197432	−53.9 ± 0.6	18 ± 13	F7IV	6107 ± 86	3.91 ± 0.11	−0.16 ± 0.12	39 ± 33	Small peak at RV = 242.4 ± 8.5 km s^{-1}; Target = TYC 4354-793-1
38	IDS	55082.7548248	18.2 ± 1.2	17 ± 3	K8V	4103 ± 71	4.58 ± 0.15	−0.10 ± 0.10	12 ± 34	
39	IDS	55524.6410282	−10.4 ± 3.1	17 ± 10	M1.5V	3466 ± 122	4.77 ± 0.24	−0.20 ± 0.11	0 ± 50	
40 c1	IDS	56381.4256583	−6.6 ± 0.4	15 ± 1	K5V	4597 ± 54	4.61 ± 0.10	0.00 ± 0.11	1 ± 44	
40 c2	IDS	56381.4256583	29.4 ± 1.8	…	…	…	…	…	…	*RV*1 of the SB2 system, Target = *Gaia* DR2 1116789735748819968
40 c2	IDS	56381.4256583	−38.5 ± 4.2	…	…	…	…	…	…	*RV*2 of the SB2 system, Target = *Gaia* DR2 1116789735748819968
40 c3	IDS	56381.4256583	−32.9 ± 0.7	15 ± 1	K1V	4976 ± 82	4.49 ± 0.14	−0.29 ± 0.13	7 ± 56	Target = *Gaia* DR2 1116789667029342080
41	FOCES	55109.6976899	…	145.7 ± 18.3	G5V	5443 ± 227	4.31 ± 0.22	−0.13 ± 0.16	2 ± 33	
41	IDS	56616.7658037	−81.5 ± 9.2	167 ± 9	G8V	5300 ± 121	3.93 ± 0.30	−0.53 ± 0.15	6 ± 38	SB1
41	IDS	56708.5273948	62.6 ± 3.5	131 ± 18	K2V	5272 ± 110	4.26 ± 0.29	−0.47 ± 0.14	16 ± 31	SB1
42 c1	FOCES	55110.6079134	−7.44 ± 0.11	11.7 ± 0.6	G1.5V	5802 ± 119	4.38 ± 0.10	−0.03 ± 0.07	97 ± 17	
42 c1	IDS	56707.6473027	−8.5 ± 0.4	18 ± 1	G4V	5787 ± 86	4.31 ± 0.12	−0.05 ± 0.12	91 ± 16	
42 c1	IDS	56708.5474164	−11.3 ± 0.6	18 ± 2	G4V	5788 ± 79	4.29 ± 0.12	−0.03 ± 0.11	108 ± 23	
42 c1	IDS	56708.5665972	−9.0 ± 0.3	18 ± 2	G1.5Vb	5822 ± 72	4.37 ± 0.12	−0.08 ± 0.11	76 ± 16	
42 c2	IDS	56708.5474164	−20.9 ± 0.6	20 ± 2	K7V	4318 ± 82	4.60 ± 0.10	−0.14 ± 0.11	11 ± 126	Target = *Gaia* DR2 1116535920362524928
43	FOCES	55110.6333984	−86.14 ± 1.62	56.7 ± 6.0	G0IV	5717 ± 310	4.19 ± 0.18	−0.11 ± 0.15	34 ± 48	SB2?
44 c1	IDS	55524.6959770	10 ± 15	224 ± 14	G2V	5732 ± 73	3.96 ± 0.20	−0.03 ± 0.11	7 ± 15	
44 c2	IDS	55524.6959770	−21.1 ± 0.7	19 ± 10	F6IV	6277 ± 98	4.05 ± 0.13	−0.16 ± 0.11	9 ± 15	Target = TYC 4618-329-1 / *Gaia* DR2 1149573805235028352
45	FOCES	55110.6542632	−8.54 ± 0.11	8.2 ± 0.4	G2V	5798 ± 78	4.33 ± 0.08	0.04 ± 0.09	73 ± 16	
46	SOPHIE	55102.6724754	−15.664 ± 0.014	16.9 ± 1.0	K1V	5108 ± 125	4.54 ± 0.09	−0.11 ± 0.12	159 ± 9	Likely SB2 system with low M_2/M_1 mass ratio
46	FOCES	55108.6932431	−15.61 ± 0.11	19.0 ± 1.4	K0V	5204 ± 112	4.52 ± 0.21	−0.10 ± 0.06	170 ± 22	Likely SB2 system with low M_2/M_1 mass ratio
46	FOCES	55110.6764087	−15.90 ± 0.28	18.4 ± 1.4	K0V	5195 ± 161	4.49 ± 0.20	−0.08 ± 0.08	204 ± 43	Likely SB2 system with low M_2/M_1 mass ratio
47	IDS	55524.7132031	−55 ± 17	182 ± 21	G2V	5684 ± 79	4.05 ± 0.13	−0.29 ± 0.14	7 ± 12	Double-peaked Hα profile (SB2?)
49	IDS	56226.7552961	12.0 ± 0.7	35 ± 2	K1V	5065 ± 97	4.52 ± 0.14	−0.20 ± 0.14	30 ± 36	SB1
49	IDS	56382.4941385	−128.0 ± 0.8	35 ± 2	K1V	5032 ± 99	4.51 ± 0.14	−0.22 ± 0.12	25 ± 15	SB1
50	IDS	56383.4526273	−104.8 ± 5.7	…	…	…	…	…	…	*RV*1 of the SB2 system
50	IDS	56383.4526273	−230.9 ± 9.1	…	…	…	…	…	…	*RV*2 of the SB2 system
51	IDS	56379.5190672	−7.3 ± 0.6	16 ± 1	K4V	4411 ± 86	4.61 ± 0.15	0.04 ± 0.11	21 ± 23	
51	IDS	56383.4744413	−156.9 ± 0.6	15 ± 1	K6V	4411 ± 84	4.61 ± 0.14	0.03 ± 0.11	9 ± 21	Likely wrong RV
51	IDS	56384.5122070	−147.5 ± 0.9	15 ± 1	K5V	4355 ± 77	4.61 ± 0.11	0.04 ± 0.11	3 ± 23	Likely wrong RV
51	IDS	56707.6040424	−8.3 ± 0.5	16 ± 1	K5V	4378 ± 64	4.61 ± 0.10	0.04 ± 0.11	23 ± 14	
52	IDS	56379.4905068	−47.0 ± 1.2	56 ± 7	G1.5Vb	5653 ± 111	3.90 ± 0.19	−0.06 ± 0.12	5 ± 21	SB1
52	IDS	56707.6221921	−26.6 ± 0.8	48 ± 1	G2V	5600 ± 92	4.20 ± 0.17	−0.00 ± 0.12	76 ± 16	SB1
70	IDS	55080.3799252	−11.1 ± 1.9	15 ± 16	M2.5V	3624 ± 55	4.52 ± 0.23	−0.14 ± 0.11	53 ± 69	SB1?
70	IDS	55081.3663773	−16.4 ± 1.7	17 ± 6	M2V	3607 ± 50	4.60 ± 0.15	−0.14 ± 0.11	25 ± 55	SB1?
71	IDS	55084.3544051	2.1 ± 0.5	15 ± 1	K5V	4514 ± 93	4.36 ± 0.17	−0.07 ± 0.11	7 ± 29	
73	IDS	55081.3839854	−8.2 ± 2.8	289 ± 5	M1.5V	3666 ± 76	3.30 ± 0.32	−0.13 ± 0.11	23 ± 66	Double-peaked Hα profile (SB2?)
76	IDS	55083.3602331	−2.9 ± 1.3	…	…	…	…	…	…	*RV*1 of an SB2 system
76	IDS	55083.3602331	−69.5 ± 4.9	…	…	…	…	…	…	*RV*2 of an SB2 system
77	IDS	55082.3663651	37.2 ± 2.1	90 ± 4	G8IV	5431 ± 101	3.91 ± 0.10	−0.01 ± 0.11	7 ± 28	Slight asymmetry of CCF profile (SB2?)

Table 3. Continued.

#⋆	Instrument	H.J.D. [2400000+]	RV [km s^{-1}]	$v \sin i$ [km s^{-1}]	SpT	$T_{\rm eff}$ [K]	$\log g$ [cm^2 s^{-1}]	$[Fe/H]$ [dex]	$W_{\rm Li}$ [mÅ]	Note
78	IDS	56379.6028405	−245.7 ± 2.6	…	…	…	…	…	…	Clear asymmetry in the CCF profile, SB2 with blended peaks, no Li, Wrong RV?
78	IDS	56707.7128193	9.0 ± 2.2	…	…	…	…	…	…	Slight asymmetry of CCF profile
78	IDS	56708.6577932	−64.9 ± 1.2	…	…	…	…	…	…	Clear asymmetry in the CCF profile, SB2 with blended peaks, no Li
79	IDS	56379.6260616	−97.1 ± 3.3	…	…	…	…	…	…	*RV*1 of an SB2 system
79	IDS	56379.6260616	−15.1 ± 12.0	…	…	…	…	…	…	*RV*2 of an SB2 system
80	IDS	55081.4025855	−26.9 ± 2.3	25 ± 7	M2V	3623 ± 55	4.55 ± 0.22	−0.13 ± 0.11	7 ± 69	
81 c1	IDS	55084.3799811	−9.7 ± 1.1	15 ± 9	M2V	3650 ± 116	4.59 ± 0.16	−0.13 ± 0.11	29 ± 79	
81 c2	IDS	55084.3799811	−10.5 ± 1.1	15 ± 9	M5V	3397 ± 50	4.57 ± 0.15	−0.15 ± 0.11	20 ± 80	Target = *Gaia* DR2 1723454381704389248
82	FOCES	55109.2943862	20.22 ± 0.21	21.1 ± 1.3	G2V	5714 ± 136	4.36 ± 0.09	−0.01 ± 0.08	10 ± 17	
82	IDS	56379.6476301	18.3 ± 1.2	26 ± 6	G8V	5513 ± 70	4.32 ± 0.12	−0.12 ± 0.13	2 ± 26	
83	IDS	55081.4207273	−155.2 ± 1.5	97 ± 3	K5V	4597 ± 85	4.14 ± 0.24	−0.08 ± 0.11	15 ± 44	
84	FOCES	55109.3127430	−108.40 ± 0.35	…	…	…	…	…	…	*RV*1 of an SB2 system
84	FOCES	55109.3127430	72.46 ± 0.43	…	…	…	…	…	…	*RV*2 of an SB2 system
85	IDS	55083.3820091	−13.0 ± 1.6	15 ± 8	M5V	3397 ± 50	4.57 ± 0.15	−0.14 ± 0.11	11 ± 45	
86	FOCES	55109.3305934	−20.85 ± 0.08	15.8 ± 0.5	K0V	5220 ± 125	4.28 ± 0.14	−0.06 ± 0.05	215 ± 17	SB1?
86	IDS	56382.6981631	−28.5 ± 0.5	17 ± 1	K1V	5264 ± 104	4.13 ± 0.26	−0.01 ± 0.11	207 ± 18	SB1?
87	FOCES	55110.2941155	−17.89 ± 0.16	19.4 ± 0.6	G9.5IV	5138 ± 151	3.79 ± 0.31	−0.04 ± 0.07	29 ± 12	
87	FOCES	55110.2941155	−52.65 ± 1.85	…	…	…	…	…	…	Radial velocity of faint source in case of an SB2 system
88	IDS	55083.4036979	8.9 ± 3.3	17 ± 3	M5V	3343 ± 70	4.59 ± 0.19	−0.14 ± 0.11	42 ± 35	
89	FOCES	55110.3164964	−70.42 ± 0.37	…	…	…	…	…	…	*RV*1 of an SB2 system
89	FOCES	55110.3164964	64.74 ± 0.41	…	…	…	…	…	…	*RV*2 of an SB2 system
90	IDS	55083.4284131	171.0 ± 5.9	215 ± 35	K7V	4685 ± 207	3.19 ± 0.43	−0.17 ± 0.15	19 ± 45	
91	FOCES	55110.3377116	1.51 ± 0.20	21.8 ± 1.3	K0IV	5051 ± 125	3.65 ± 0.40	−0.13 ± 0.07	29 ± 18	
92	FOCES	55110.3577589	24.78 ± 0.68	…	…	…	…	…	…	*RV*1 of an SB3 system
92	FOCES	55110.3577589	−8.04 ± 0.39	…	…	…	…	…	…	*RV*2 of an SB3 system
92	FOCES	55110.3577589	−47.79 ± 0.99	…	…	…	…	…	…	*RV*3 of an SB3 system
92	IDS	56382.6735452	2.3 ± 3.2	…	…	…	…	…	…	*RV*1 of an SB2 system
92	IDS	56382.6735452	−56.4 ± 7.6	…	…	…	…	…	…	*RV*2 of an SB2 system
92	IDS	56383.6233936	−80.0 ± 3.6	…	…	…	…	…	…	*RV*1 of an SB3 system
92	IDS	56383.6233936	45.3 ± 0.6	…	…	…	…	…	…	*RV*2 of an SB3 system
92	IDS	56383.6233936	−15.1 ± 0.7	…	…	…	…	…	…	*RV*3 of an SB3 system
93	IDS	56379.6709380	−10.5 ± 1.1	32 ± 1	G2V	5565 ± 12	4.32 ± 0.11	−0.05 ± 0.13	200 ± 22	
94	FOCES	55110.3774734	−10.56 ± 0.30	26.0 ± 1.3	G2.5V	5775 ± 92	4.17 ± 0.10	0.11 ± 0.05	24 ± 26	
95	IDS	55081.4400960	−18.4 ± 0.6	15 ± 1	K5V	4540 ± 83	4.30 ± 0.30	−0.03 ± 0.11	11 ± 48	
96	FOCES	55110.3949910	−12.78 ± 0.47	25.0 ± 1.3	G1.5Vb	5881 ± 173	4.19 ± 0.11	−0.01 ± 0.10	28 ± 24	
97	FOCES	55110.4120357	…	286.6 ± 14.0	sdF8	6128 ± 413	3.99 ± 0.15	−1.00 ± 0.31	…	
98	IDS	55079.4387020	−30.8 ± 0.5	40 ± 1	K3V	4836 ± 67	4.01 ± 0.29	0.04 ± 0.11	119 ± 34	Slight asymmetry of CCF profile (SB2?)
99	FOCES	55109.3509585	−22.48 ± 0.05	3.3 ± 1.7	G9III	4835 ± 102	2.80 ± 0.23	−0.12 ± 0.06	16 ± 11	
100	IDS	55082.4133394	−15.6 ± 0.6	16 ± 3	G1.5V	5940 ± 142	4.13 ± 0.11	−0.08 ± 0.11	23 ± 19	
101	IDS	55082.3933040	−19.6 ± 0.5	15 ± 1	K4V	4583 ± 99	4.36 ± 0.20	−0.01 ± 0.11	3 ± 13	
102	IDS	55082.4621634	−24.0 ± 0.7	27 ± 3	K3V	4858 ± 103	3.31 ± 0.18	0.02 ± 0.11	166 ± 58	
103	IDS	55082.4492793	−10.7 ± 0.8	…	…	…	…	…	…	*RV*1 of an SB2 system, blended CCF peaks
103	IDS	55082.4492793	−65.8 ± 9.4	…	…	…	…	…	…	*RV*2 of an SB2 system, blended CCF peaks
104	FOCES	55109.3745146	−27.96 ± 0.06	7.3 ± 1.0	K1III-IV	4709 ± 98	2.69 ± 0.26	−0.02 ± 0.07	17 ± 14	
105	SOPHIE	55102.3700894	16.135 ± 0.011	13.4 ± 1.4	K0V	5350 ± 94	4.49 ± 0.10	−0.14 ± 0.10	5 ± 7	SB1
105	FOCES	55107.4723974	−83.71 ± 0.11	15.4 ± 0.4	K1V	5193 ± 100	4.43 ± 0.20	−0.06 ± 0.05	12 ± 24	SB1
106 c1	IDS	55084.4198646	−11.6 ± 0.9	60 ± 1	G5V	5444 ± 108	3.92 ± 0.13	−0.05 ± 0.10	248 ± 40	
106 c1	FOCES	55108.3093674	−10.44 ± 0.90	63.1 ± 11.3	G5V	5439 ± 218	4.25 ± 0.37	−0.04 ± 0.12	238 ± 74	
106 c1	IDS	56383.6967227	−20.1 ± 0.9	60 ± 1	K1V	5259 ± 82	4.29 ± 0.21	−0.18 ± 0.12	260 ± 22	
106 c2	IDS	56383.6967227	−13.6 ± 0.7	15 ± 1	K0V	5187 ± 69	3.99 ± 0.16	0.02 ± 0.11	28 ± 93	Target = *Gaia* DR2 2248508292487691008
107	IDS	55081.4609906	8.6 ± 0.9	16 ± 2	K7V	4080 ± 139	4.54 ± 0.15	−0.15 ± 0.12	3 ± 23	
108	IDS	55079.4549152	−30.6 ± 0.3	15 ± 1	K1III	4760 ± 60	2.74 ± 0.17	−0.03 ± 0.11	25 ± 13	
109	IDS	55084.4658235	−65.1 ± 0.8	43 ± 3	K1IV	4765 ± 87	2.97 ± 0.34	−0.09 ± 0.11	96 ± 27	Double-peaked Hα profile (SB2?)
110	IDS	55084.4781905	−96.0 ± 2.5	…	…	…	…	…	…	*RV*1 of an SB2 system
110	IDS	55084.4781905	59.4 ± 2.7	…	…	…	…	…	…	*RV*1 of an SB2 system
110	IDS	55084.4781905	−35.0 ± 21.0	…	…	…	…	…	…	Radial velocity of faint source in case of an SB3 system
111	IDS	55083.4852060	−8.8 ± 0.9	35 ± 6	M2V	3676 ± 74	4.64 ± 0.16	−0.12 ± 0.11	13 ± 60	
112	FOCES	55110.4332919	−22.31 ± 0.14	7.7 ± 0.3	K1V	5118 ± 80	4.40 ± 0.15	−0.07 ± 0.05	157 ± 20	
112	IDS	56382.6854679	−25.2 ± 0.7	15 ± 1	K2.5V	4997 ± 76	4.52 ± 0.12	−0.05 ± 0.11	158 ± 13	

Table 3. Continued.

#⋆	Instrument	H.J.D. [2400000+]	RV [km s^{-1}]	$v \sin i$ [km s^{-1}]	SpT	$T_{\rm eff}$ [K]	$\log g$ [cm^2 s^{-1}]	$[Fe/H]$ [dex]	$W_{\rm Li}$ [mÅ]	Note
113	IDS	55084.5071613	−3.1 ± 0.6	15 ± 8	K7V	4151 ± 120	4.53 ± 0.15	−0.11 ± 0.11	22 ± 30	
114	FOCES	55109.3980335	−13.74 ± 0.06	8.3 ± 0.5	K3V	4813 ± 91	4.35 ± 0.21	0.02 ± 0.06	29 ± 10	
115	SOPHIE	55102.3938018	−11.178 ± 0.007	9.6 ± 0.9	G9.5IV	5125 ± 187	4.01 ± 0.42	−0.09 ± 0.12	291 ± 9	
115	FOCES	55108.3725324	−11.40 ± 0.06	9.8 ± 1.3	G9.5IV	5219 ± 107	4.02 ± 0.23	−0.02 ± 0.07	290 ± 16	
116	IDS	55082.4760161	−9.7 ± 0.9	46 ± 3	G8IV	5242 ± 68	3.91 ± 0.14	−0.10 ± 0.11	112 ± 25	Slight asymmetry of CCF profile (SB2?)
117	IDS	55081.4803878	−65.7 ± 0.7	15 ± 1	K1III	4617 ± 76	2.50 ± 0.23	−0.07 ± 0.11	8 ± 35	
118	IDS	55079.4882147	−3.8 ± 0.5	20 ± 1	K5V	4628 ± 146	3.96 ± 0.25	−0.21 ± 0.11	6 ± 32	
119	IDS	55082.4935946	78.4 ± 4.5	...	...	...	...	...	...	$RV1$ of an SB2 system
119	IDS	55082.4935946	−61.0 ± 4.7	...	...	...	...	...	...	$RV2$ of an SB2 system
120	IDS	55084.5179598	−20.1 ± 0.9	55 ± 10	F8V	6061 ± 81	4.01 ± 0.13	−0.01 ± 0.11	22 ± 27	
121	IDS	55084.5687318	−24.4 ± 0.5	16 ± 3	M5V	3397 ± 50	4.55 ± 0.15	−0.14 ± 0.11	0 ± 54	
122	FOCES	55110.4532427	11.39 ± 0.57	30.9 ± 1.7	G2V	5708 ± 146	4.30 ± 0.16	0.02 ± 0.10	41 ± 20	
123	IDS	55079.4139454	−21.8 ± 0.5	29 ± 2	G2.5V	5685 ± 116	3.96 ± 0.14	−0.08 ± 0.11	156 ± 61	
123	IDS	55079.4221410	−23.0 ± 0.3	24 ± 2	G1.5bV	5647 ± 94	3.96 ± 0.11	−0.09 ± 0.11	195 ± 31	
124	IDS	55083.5114570	−14.9 ± 0.6	37 ± 3	K7V	4261 ± 166	4.48 ± 0.17	−0.11 ± 0.11	393 ± 65	
124	IDS	55168.3269044	−12.1 ± 0.7	37 ± 3	K7V	4340 ± 188	4.47 ± 0.18	−0.12 ± 0.11	430 ± 81	
125	FOCES	55109.4220827	−21.44 ± 0.09	13.4 ± 1.5	K4V	5532 ± 168	4.31 ± 0.11	−0.01 ± 0.07	181 ± 37	
126	IDS	55084.5870534	37.8 ± 0.6	30 ± 1	K1V	5240 ± 71	4.33 ± 0.14	−0.07 ± 0.11	47 ± 16	
127	FOCES	55109.4465507	...	131.1 ± 11.1	K1V	5212 ± 296	4.42 ± 0.35	−0.04 ± 0.15	177 ± 86	
128	SOPHIE	55102.4157992	−18.752 ± 0.009	7.46 ± 2.16	G1V	5682 ± 131	4.28 ± 0.19	−0.34 ± 0.16	38 ± 7	$RV1$ of a possible SB3 system
128	SOPHIE	55102.4157992	41.8 ± 0.9	...	...	...	...	...	...	$RV2$ in case of an SB3 system
128	SOPHIE	55102.4157992	−72.3 ± 0.9	...	...	...	...	...	...	$RV3$ in case of an SB3 system
128	FOCES	55109.4719452	−19.14 ± 0.09	10.5 ± 1.3	G1V	5863 ± 78	4.23 ± 0.05	−0.05 ± 0.08	62 ± 13	$RV1$ of a possible SB3 system
128	FOCES	55109.4719452	−46.36 ± 0.75	...	...	...	...	...	...	$RV2$ in case of an SB3 system
128	FOCES	55109.4719452	12.91 ± 0.96	...	...	...	...	...	...	$RV3$ in case of an SB3 system
129	FOCES	55109.4972983	−20.53 ± 0.50	47.5 ± 1.8	G1.5Vb	5799 ± 163	4.23 ± 0.11	0.00 ± 0.11	147 ± 35	
130	FOCES	55109.5207365	...	106.0 ± 4.7	K2V	5069 ± 244	4.40 ± 0.34	−0.08 ± 0.10	244 ± 88	
131	FOCES	55109.5436838	−29.57 ± 0.15	...	...	...	...	...	...	$RV1$ of an SB2 system
131	FOCES	55109.5436838	−3.04 ± 0.23	...	...	...	...	...	...	$RV2$ of an SB2 system
132	IDS	55079.4708973	42.1 ± 0.4	15 ± 1	K0III-IV	4824 ± 68	3.21 ± 0.21	−0.13 ± 0.12	47 ± 22	
133	SOPHIE	55102.4856691	25.297 ± 0.007	11.9 ± 0.8	K0III	4500 ± 200	2.15 ± 0.74	−0.29 ± 0.22	77 ± 10	SB1
133	FOCES	55108.3992783	−18.49 ± 0.08	11.7 ± 0.7	K1IV	4761 ± 131	2.96 ± 0.43	−0.01 ± 0.09	68 ± 16	SB1
134	IDS	55084.6008565	−4.8 ± 0.8	...	...	...	...	...	...	$RV1$ of an SB2 system
134	IDS	55084.6008565	−62.8 ± 6.4	...	...	...	...	...	...	$RV2$ of an SB2 system
135	IDS	55081.5434654	−37.3 ± 0.7	30 ± 1	K3V	4658 ± 108	3.17 ± 0.25	−0.06 ± 0.11	29 ± 27	
136	IDS	55079.5087978	−7.2 ± 0.6	15 ± 1	K5V	4542 ± 130	3.83 ± 0.19	−0.07 ± 0.10	44 ± 26	
137	FOCES	55108.4214544	...	262.8 ± 26.7	G1IV	5729 ± 612	4.12 ± 0.36	−0.16 ± 0.25	...	
138 c1	IDS	55083.5351512	−69.3 ± 0.7	15 ± 1	K1III	4602 ± 102	2.40 ± 0.22	−0.09 ± 0.12	18 ± 19	
138 c1	IDS	55168.3536372	−70.2 ± 0.4	15 ± 1	K1III	4601 ± 126	2.31 ± 0.21	−0.09 ± 0.11	25 ± 38	
138 c2	IDS	55168.3536372	...	...	A9IV	7260 ± 137	3.77 ± 0.18	−0.13 ± 0.16	62 ± 82	Fast rotator, Target = *Gaia* DR2 2203366330791767552
139	IDS	55168.3747409	...	...	A6V	7956 ± 219	3.97 ± 0.12	0.11 ± 0.14	...	Fast rotator
140 c1	IDS	55082.5169938	−16.3 ± 0.6	15 ± 1	K4V	4823 ± 56	3.83 ± 0.34	−0.05 ± 0.11	37 ± 62	
140 c2	IDS	55082.5169938	−17.5 ± 1.6	28 ± 9	G1V	5268 ± 168	3.93 ± 0.25	−0.06 ± 0.11	21 ± 43	Target = *Gaia* DR2 2005807146670408704
141	FOCES	55108.4399839	60.85 ± 0.07	11.3 ± 1.5	K0V	5304 ± 90	4.26 ± 0.11	−0.06 ± 0.05	16 ± 12	
142	IDS	55081.5039811	−9.7 ± 0.5	25 ± 1	K3V	4828 ± 56	4.30 ± 0.18	−0.10 ± 0.11	445 ± 36	
142	IDS	55082.6200845	−8.4 ± 0.6	23 ± 2	K5V	4837 ± 84	4.09 ± 0.26	−0.10 ± 0.12	419 ± 57	
143	IDS	55081.5219193	−17.2 ± 1.1	15 ± 1	K8V	4166 ± 127	4.53 ± 0.15	−0.11 ± 0.11	4 ± 62	
144	FOCES	55108.4588134	20.90 ± 0.08	15.7 ± 0.6	K0V	5325 ± 140	4.36 ± 0.13	−0.13 ± 0.07	35 ± 11	
145	FOCES	55108.4772190	−31.43 ± 0.06	11.5 ± 0.3	K0IV	4975 ± 114	3.28 ± 0.45	−0.08 ± 0.06	66 ± 9	
146	IDS	55079.5256864	−47.9 ± 1.2	24 ± 10	M3V	3659 ± 70	4.64 ± 0.15	−0.12 ± 0.11	77 ± 64	
147	IDS	55082.5508470	77.2 ± 1.6	...	...	...	...	...	...	$RV1$ of an SB2 system
147	IDS	55082.5508470	−24.5 ± 3.4	...	...	...	...	...	...	$RV2$ of an SB2 system
148	SOPHIE	55101.6074655	−17.543 ± 0.011	6.9 ± 1.0	F6IV	6075 ± 198	3.84 ± 0.18	−0.23 ± 0.20	3 ± 4	
149	FOCES	55109.5981177	...	102.8 ± 15.6	K1V	5823 ± 397	4.14 ± 0.19	−0.08 ± 0.22	146 ± 71	
150	FOCES	55109.5706683	−13.43 ± 0.48	42.8 ± 3.3	G0V	5645 ± 221	4.18 ± 0.26	0.03 ± 0.11	208 ± 47	
151	FOCES	55110.4837770	−23.22 ± 0.22	9.5 ± 2.4	K7V	4354 ± 79	4.47 ± 0.18	−0.13 ± 0.07	44 ± 18	
152	IDS	55081.5570883	−8.8 ± 0.9	30 ± 1	K5V	4760 ± 126	4.13 ± 0.28	−0.09 ± 0.11	428 ± 98	Slight asymmetry of CCF profile (SB2?)
153	SOPHIE	55101.4924232	−13.599 ± 0.202	64.8 ± 3.2	K2V	5050 ± 76	4.57 ± 0.06	−0.21 ± 0.03	432 ± 34	SB1
153	FOCES	55107.5049149	−5.20 ± 0.89	63.4 ± 3.9	K3V	4837 ± 217	4.57 ± 0.51	−0.04 ± 0.11	432 ± 65	SB1

Table 3. Continued.

#⋆	Instrument	H.J.D. [2400000+]	RV [km s^{-1}]	$v \sin i$ [km s^{-1}]	SpT	$T_{\rm eff}$ [K]	$\log g$ [cm^2 s^{-1}]	$[Fe/H]$ [dex]	$W_{\rm Li}$ [mÅ]	Note
153	FOCES	55108.5236282	−7.99 ± 0.66	65.1 ± 3.1	K3V	4831 ± 192	4.54 ± 0.63	−0.02 ± 0.10	463 ± 56	SB1
154	IDS	55083.6251829	−75.8 ± 1.3	39 ± 8	M2V	3725 ± 68	4.65 ± 0.14	−0.12 ± 0.11	12 ± 43	SB1
154	IDS	55168.4203365	−22.0 ± 1.9	47 ± 14	M0V	3789 ± 78	4.65 ± 0.15	−0.11 ± 0.10	23 ± 92	SB1
155	IDS	55082.5984520	−10.8 ± 0.8	…	…	…	…	…	…	*RV*1 of an SB3 system
155	IDS	55082.5984520	−85.9 ± 1.1	…	…	…	…	…	…	*RV*2 of an SB3 system
155	IDS	55082.5984520	80.3 ± 4.4	…	…	…	…	…	…	*RV*3 of an SB3 system
156	IDS	55081.6114206	−10.7 ± 1.1	15 ± 1	K7V	4245 ± 161	4.42 ± 0.28	−0.17 ± 0.12	473 ± 53	Likely SB1 system
156	IDS	55083.6014848	−4.6 ± 0.6	15 ± 8	K7V	4356 ± 98	4.38 ± 0.27	−0.11 ± 0.11	457 ± 40	Likely SB1 system
157	SOPHIE	55101.5735636	−10.958 ± 0.007	7.8 ± 0.7	G5V	5649 ± 149	4.24 ± 0.18	0.02 ± 0.12	52 ± 7	
158	SOPHIE	55101.5440024	−8.209 ± 0.015	25.0 ± 1.0	K1V	5089 ± 74	4.38 ± 0.37	−0.09 ± 0.09	331 ± 16	
158	FOCES	55109.6300243	−8.91 ± 0.22	25.6 ± 1.0	K2V	5084 ± 71	4.41 ± 0.23	−0.07 ± 0.05	357 ± 35	
159	IDS	55080.6631020	−24.5 ± 1.5	32 ± 6	G8III	4998 ± 100	3.30 ± 0.22	−0.12 ± 0.12	56 ± 26	
159	IDS	55081.6316086	−58.7 ± 1.2	30 ± 1	K0IV	4800 ± 85	3.32 ± 0.22	−0.13 ± 0.11	117 ± 55	
159	IDS	55081.6316086	59.4 ± 8.4	…	…	…	…	…	…	Radial velocity of faint source in case of an SB2 system
159	IDS	55081.6476659	−59.1 ± 0.9	28 ± 2	K2V	5055 ± 102	3.62 ± 0.24	−0.19 ± 0.12	98 ± 64	
159	IDS	55081.6476659	67.0 ± 9.4	…	…	…	…	…	…	Radial velocity of faint source in case of an SB2 system
161	IDS	55083.5823330	−6.9 ± 1.2	15 ± 9	M2V	3607 ± 50	4.60 ± 0.15	−0.13 ± 0.11	66 ± 67	
161	IDS	55168.3958781	−8.8 ± 1.8	16 ± 13	M2V	3606 ± 50	4.61 ± 0.15	−0.13 ± 0.11	66 ± 67	
162	IDS	55084.6344091	43.7 ± 2.2	…	…	…	…	…	…	*RV*1 of an SB2 system
162	IDS	55084.6344091	−62.3 ± 2.7	…	…	…	…	…	…	*RV*2 of an SB2 system
163 c1	IDS	55524.4297626	−45.3 ± 0.6	32 ± 2	G8IV	5529 ± 68	3.80 ± 0.16	−0.02 ± 0.11	35 ± 19	Slight asymmetry of CCF profile (SB2?)
163 c2	IDS	55524.4297626	−4.3 ± 2.3	275 ± 11	F2IV	6740 ± 103	4.26 ± 0.11	−0.03 ± 0.11	2 ± 41	Target = *Gaia* DR2 537608345003955840
164	IDS	56227.5352424	−9.9 ± 1.1	…	…	…	…	…	…	*RV*1 of an SB2 system
164	IDS	56227.5352424	84.2 ± 4.0	…	…	…	…	…	…	*RV*2 of an SB2 system
165	IDS	55525.4337780	−32.1 ± 2.5	93 ± 12	F3IV	6753 ± 100	4.13 ± 0.11	0.00 ± 0.10	61 ± 43	
166	IDS	55525.4543251	−2.6 ± 1.3	80 ± 4	G5III	5576 ± 87	3.81 ± 0.15	0.02 ± 0.10	51 ± 26	Slight asymmetry of CCF profile (SB2?)
167	IDS	55525.4693819	45.1 ± 1.4	…	…	…	…	…	…	*RV*1 of an SB2 system
167	IDS	55525.4693819	−29.1 ± 5.6	…	…	…	…	…	…	*RV*2 of an SB2 system
168 c1	IDS	55525.4910577	−11.6 ± 0.8	15 ± 1	F8V	6059 ± 97	4.05 ± 0.13	0.03 ± 0.11	78 ± 94	
168 c1	IDS	55528.4448003	−6.0 ± 1.0	15 ± 8	F8V	5679 ± 121	3.94 ± 0.13	−0.10 ± 0.14	16 ± 189	
168 c1	IDS	55528.4898928	−7.9 ± 0.4	15 ± 7	G1.5bV	5844 ± 79	4.03 ± 0.14	−0.10 ± 0.11	17 ± 24	
168 c2	IDS	55525.4910577	−38.5 ± 1.4	39 ± 28	G3V	5812 ± 184	3.95 ± 0.12	−0.17 ± 0.13	90 ± 250	Target = *Gaia* DR2 534835788997551488
168 c2	IDS	55528.4898928	−37.5 ± 0.6	26 ± 20	F8IV	5906 ± 150	3.98 ± 0.13	−0.24 ± 0.12	65 ± 44	Target = *Gaia* DR2 534835788997551488
169 c1	IDS	55524.5177831	26.2 ± 1.9	…	…	…	…	…	…	*RV*1 of an SB2 system
169 c1	IDS	55524.5177831	−33.7 ± 2.7	…	…	…	…	…	…	*RV*2 of an SB2 system
169 c1	IDS	55528.5188044	1.1 ± 0.7	50 ± 4	G0V	5960 ± 76	4.05 ± 0.15	0.00 ± 0.11	44 ± 32	SB2 with blended peaks
169 c1	SOPHIE	55589.3272880	9.750 ± 0.005	…	…	…	…	…	…	*RV*1 of an SB2 system
169 c1	SOPHIE	55589.3272880	−16.5 ± 1.8	…	…	…	…	…	…	*RV*2 of an SB2 system
169 c1	IDS	56613.5135269	−24.1 ± 1.7	…	…	…	…	…	…	*RV*1 of an SB2 system
169 c1	IDS	56613.5135269	30.5 ± 4.1	…	…	…	…	…	…	*RV*2 of an SB2 system
169 c2	IDS	55524.5177831	−20.6 ± 0.6	18 ± 5	F7IV	5961 ± 94	4.01 ± 0.13	−0.10 ± 0.11	32 ± 35	Target = *Gaia* DR2 533784174844087168
174 c1	IDS	56380.7696598	3.5 ± 3.9	120 ± 5	K0IV	5300 ± 77	4.26 ± 0.17	−0.11 ± 0.13	273 ± 53	
174 c2	IDS	56380.7696598	−30.7 ± 0.7	43 ± 16	F4V	6575 ± 82	4.01 ± 0.12	−0.15 ± 0.11	0 ± 30	Target = *Gaia* DR2 2291000598671699200
179	IDS	56381.7515829	−147.8 ± 0.8	32 ± 2	K1V	5181 ± 67	3.98 ± 0.19	−0.14 ± 0.11	236 ± 31	Likely wrong RV
182	IDS	55525.3646672	−11.4 ± 0.5	15 ± 1	K5V	4464 ± 119	4.28 ± 0.30	−0.10 ± 0.12	441 ± 39	
184 c1	IDS	56227.4707076	−5.0 ± 0.7	19 ± 2	K0V	5110 ± 67	4.33 ± 0.10	0.02 ± 0.11	316 ± 36	SB1?
184 c1	IDS	56384.7604811	−10.0 ± 0.7	18 ± 1	K2.5V	5096 ± 71	3.96 ± 0.32	−0.01 ± 0.11	335 ± 42	SB1?
184 c2	IDS	56227.4707076	−98.8 ± 0.9	15 ± 1	K5III	3977 ± 79	1.30 ± 0.26	−0.10 ± 0.11	56 ± 76	Target = *Gaia* DR2 2206637339215351936
184 c2	IDS	56384.7604811	−104.4 ± 1.0	15 ± 8	K3.5IIIb	3949 ± 68	1.14 ± 0.20	−0.10 ± 0.11	51 ± 79	Target = *Gaia* DR2 2206637339215351936
185 c1	IDS	56226.4549371	−16.4 ± 0.7	15 ± 8	K0III	4664 ± 83	2.61 ± 0.22	−0.08 ± 0.13	326 ± 29	
185 c2	IDS	56226.4549371	−55.4 ± 0.8	15 ± 8	G8IV-V	5232 ± 90	3.78 ± 0.17	−0.07 ± 0.12	0 ± 98	Target = *Gaia* DR2 2226453257466755328
186	IDS	56226.4757748	−3.8 ± 0.7	19 ± 2	K2V	5085 ± 79	4.50 ± 0.12	−0.07 ± 0.12	349 ± 24	
188	IDS	56226.4922890	−11.1 ± 0.7	15 ± 7	K1V	5242 ± 83	4.25 ± 0.20	−0.07 ± 0.12	255 ± 18	
189	IDS	56226.5114830	−5.6 ± 0.7	17 ± 1	K4V	4503 ± 86	4.62 ± 0.10	0.01 ± 0.10	360 ± 31	
191 c1	IDS	56227.4891806	−7.6 ± 0.8	16 ± 1	K7V	4066 ± 72	4.63 ± 0.10	−0.06 ± 0.12	551 ± 41	
191 c2	IDS	56227.4891806	−7.1 ± 1.3	24 ± 7	M1.0V	3701 ± 81	4.69 ± 0.13	−0.15 ± 0.11	540 ± 95	Target = *Gaia* DR2 2231866565525667712
192	IDS	56225.4960186	−10.3 ± 0.8	38 ± 2	K2V	5039 ± 85	4.48 ± 0.14	−0.06 ± 0.10	313 ± 40	
193	FOCES	55168.4199992	−7.58 ± 0.39	11.0 ± 1.0	K1V	5172 ± 100	4.27 ± 0.22	−0.06 ± 0.06	305 ± 48	
193	IDS	55524.4053541	−7.6 ± 0.5	15 ± 1	K2V	5142 ± 68	4.20 ± 0.21	−0.10 ± 0.10	296 ± 21	

Table 3. Continued.

#⋆	Instrument	H.J.D. [2400000+]	RV [km s^{-1}]	$v \sin i$ [km s^{-1}]	SpT	$T_{\rm eff}$ [K]	$\log g$ [cm^2 s^{-1}]	$[Fe/H]$ [dex]	$W_{\rm Li}$ [mÅ]	Note
G1	IDS	55079.5501320	-11.2 ± 0.4	32 ± 4	G1V	5561 ± 77	4.27 ± 0.12	-0.07 ± 0.11	210 ± 38	
G1	SOPHIE	55102.4611823	-7.932 ± 0.008	29.2 ± 1.0	G2V	5711 ± 139	4.40 ± 0.11	-0.04 ± 0.05	208 ± 20	
G1	FOCES	55108.5564041	-8.90 ± 0.19	30.6 ± 0.7	G2V	5696 ± 158	4.33 ± 0.13	0.00 ± 0.07	211 ± 24	
G1	FOCES	55110.5085252	-8.38 ± 0.49	30.6 ± 0.8	G2V	5757 ± 128	4.32 ± 0.11	0.03 ± 0.09	207 ± 27	
G3 c1	IDS	55079.5690304	-9.3 ± 0.3	15 ± 1	K1V	5105 ± 56	4.28 ± 0.18	-0.09 ± 0.10	310 ± 22	
G3 c1	SOPHIE	55102.4410682	-8.977 ± 0.009	12.0 ± 1.0	K1V	5108 ± 81	4.12 ± 0.49	-0.07 ± 0.10	316 ± 12	
G3 c1	FOCES	55108.5807998	-9.14 ± 0.09	12.3 ± 0.5	K1V	5145 ± 96	4.39 ± 0.22	-0.05 ± 0.04	303 ± 19	
G3 c1	FOCES	55110.5331687	-9.33 ± 0.15	13.3 ± 1.4	K0V	5148 ± 159	4.30 ± 0.32	-0.05 ± 0.07	289 ± 37	
G3 c1	IDS	55525.4020459	-8.5 ± 0.4	15 ± 1	K2V	5143 ± 69	4.23 ± 0.18	-0.08 ± 0.10	316 ± 26	
G3 c2	IDS	55525.4020459	-8.7 ± 0.7	32 ± 3	K7V	4262 ± 166	4.49 ± 0.17	-0.11 ± 0.11	453 ± 90	Target = *Gaia* DR2 5646984517893591 04
G4	IDS	55079.5781353	-9.8 ± 0.3	...	...	...	...	...	...	SB2 with blended peaks
G4	IDS	55080.6849896	-10.3 ± 0.9	...	...	...	...	...	...	SB2 with blended peaks
G4	IDS	55081.5941743	-29.1 ± 1.8	...	...	...	...	...	...	*RV*1 of an SB2 system
G4	IDS	55081.5941743	15.9 ± 1.9	...	...	...	...	...	...	*RV*2 of an SB2 system
G4	IDS	55082.6486286	-35.8 ± 2.0	...	...	...	...	...	...	*RV*1 of an SB2 system
G4	IDS	55082.6486286	17.1 ± 2.0	...	...	...	...	...	...	*RV*2 of an SB2 system
G4	IDS	55083.6483453	19.5 ± 2.1	...	...	...	...	...	...	*RV*1 of an SB2 system
G4	IDS	55083.6483453	-41.5 ± 2.3	...	...	...	...	...	...	*RV*2 of an SB2 system
G4	IDS	55084.6542722	-43.6 ± 2.2	...	...	...	...	...	...	*RV*1 of an SB2 system
G4	IDS	55084.6542722	24.5 ± 2.3	...	...	...	...	...	...	*RV*2 of an SB2 system
G4	SOPHIE	55101.5200320	-46.449 ± 0.013	...	...	...	...	...	...	*RV*1 of an SB2 system
G4	SOPHIE	55101.5200320	28.267 ± 0.013	...	...	...	...	...	...	*RV*2 of an SB2 system
G4	FOCES	55107.5591610	-30.69 ± 0.29	...	...	...	...	...	...	*RV*1 of an SB2 system
G4	FOCES	55107.5591610	11.91 ± 0.30	...	...	...	...	...	...	*RV*2 of an SB2 system
G4	FOCES	55108.5935676	-27.41 ± 0.17	...	...	...	...	...	...	*RV*1 of an SB2 system
G4	FOCES	55108.5935676	8.31 ± 0.18	...	...	...	...	...	...	*RV*2 of an SB2 system
G4	FOCES	55109.6618153	-24.63 ± 0.21	...	...	...	...	...	...	*RV*1 of an SB2 system
G4	FOCES	55109.6618153	5.99 ± 0.22	...	...	...	...	...	...	*RV*2 of an SB2 system
G4	FOCES	55110.5460213	3.83 ± 0.34	...	...	...	...	...	...	*RV*1 of an SB2 system
G4	FOCES	55110.5460213	-23.22 ± 0.33	...	...	...	...	...	...	*RV*2 of an SB2 system
G4	FOCES	55168.3934106	33.80 ± 0.55	...	...	...	...	...	...	*RV*1 of an SB2 system
G4	FOCES	55168.3934106	-51.59 ± 0.60	...	...	...	...	...	...	*RV*2 of an SB2 system

⋆ During one IDS observation, several apertures might be visible on the cuts perpendicular to the spectral direction. In such a case, we ranked the sources in reverse order to their maximum intensity (i.e., "c1" = the brightest one).

Table 4. Galactic positions and space velocities of the targets, along with the astrometry in *Gaia* DR2, and the average *RV* values and lithium equivalent widths obtained during our survey.

#⋆	π [mas]	$\mu_\alpha \cos\delta$ [mas yr^{-1}]	μ_δ [mas yr^{-1}]	$\langle RV \rangle$ [km s^{-1}]	X [pc]	Y [pc]	Z [pc]	$U_\odot$ [km s^{-1}]	$V_\odot$ [km s^{-1}]	$W_\odot$ [km s^{-1}]	$\langle W_{\rm Li} \rangle$ [mÅ]	A_v [mag]	Note
1	0.3580 ± 0.0294	−4.088 ± 0.043	−3.706 ± 0.041	2.2 ± 0.3	1210 ± 100	2495 ± 205	−330 ± 27	−41.6 ± 4.0	35.6 ± 2.0	−48.5 ± 4.1	72 ± 15	1.76	
2	53.6844 ± 0.0763	−123.729 ± 0.114	4.509 ± 0.071	…	7.762 ± 0.017	16.297 ± 0.024	−4.598 ± 0.016	…	…	…	…	…	SB2
3	33.8287 ± 0.0602	208.768 ± 0.097	−35.025 ± 0.068	−14.3 ± 2.0	13.498 ± 0.028	25.394 ± 0.046	−6.840 ± 0.025	19.7 ± 0.9	−26.1 ± 1.7	−3.4 ± 0.5	18 ± 41	0	VB
4	5.7787 ± 0.0258	−12.682 ± 0.045	0.420 ± 0.033	…	87.57 ± 0.39	141.29 ± 0.63	48.11 ± 0.22	…	…	…	…	…	W UMa-type star
5	74.2071 ± 0.9587	447.857 ± 1.179	132.925 ± 0.941	3.05 ± 0.93	6.434 ± 0.083	11.485 ± 0.148	−2.879 ± 0.037	24.0 ± 0.6	−12.5 ± 0.8	12.9 ± 0.2	27 ± 26	0.49	
6 c1	6.4739 ± 0.1404	24.376 ± 0.307	−3.003 ± 0.209	…	79.2 ± 1.7	125.2 ± 2.7	43.77 ± 0.95	…	…	…	…	…	SB2, VB, Cep I member
6 c2	6.7211 ± 0.0321	23.318 ± 0.061	−2.834 ± 0.046	−8.75 ± 0.56	76.32 ± 0.36	120.56 ± 0.58	42.17 ± 0.21	8.3 ± 0.3	−15.9 ± 0.5	−5.3 ± 0.2	324 ± 27	0	Cep I member
6 c3	0.6803 ± 0.0424	5.705 ± 0.074	7.679 ± 0.057	−1.7 ± 9.1	754 ± 47	1191 ± 74	416 ± 26	46.5 ± 5.2	−24.8 ± 7.5	40.9 ± 4.1	…	…	
7	7.9526 ± 0.0297	−1.495 ± 0.043	−9.372 ± 0.047	…	68.31 ± 0.26	104.88 ± 0.39	12.019 ± 0.068	…	…	…	…	0	Likely an SB2 system
8	0.1731 ± 0.0331	−0.951 ± 0.039	−0.495 ± 0.042	−83.0 ± 0.7	3240 ± 620	4750 ± 910	−575 ± 110	−66.6 ± 4.2	−54.7 ± 2.9	−18.2 ± 2.8	3 ± 41	0.94	
9	36.0837 ± 0.0377	163.840 ± 0.039	−132.775 ± 0.047	−17.6 ± 1.8	16.160 ± 0.017	22.438 ± 0.024	−1.851 ± 0.013	8.3 ± 1.0	−28.2 ± 1.5	−14.6 ± 0.1	6 ± 65	0	
10	5.2527 ± 0.0256	3.741 ± 0.045	−17.551 ± 0.045	…	107.04 ± 0.52	154.47 ± 0.75	30.43 ± 0.17	…	…	…	…	…	SB2
11	2.4320 ± 0.0250	−6.039 ± 0.049	0.370 ± 0.037	…	202.5 ± 2.1	310.5 ± 3.2	177.8 ± 1.8	…	…	…	…	…	SB2
12	23.0372 ± 0.0313	102.226 ± 0.034	−44.68 ± 0.039	−16.8 ± 2.9	25.667 ± 0.035	34.862 ± 0.048	−3.179 ± 0.016	7.6 ± 1.7	−26.7 ± 2.3	−6.0 ± 0.2	29 ± 39	0	
13	5.6032 ± 0.0235	158.233 ± 0.039	12.937 ± 0.040	…	101.30 ± 0.43	142.12 ± 0.60	37.30 ± 0.17	…	…	…	…	…	SB2
14	48.4853 ± 0.0351	−139.231 ± 0.044	8.374 ± 0.052	−10.1 ± 1.9	12.562 ± 0.010	16.342 ± 0.012	0.706 ± 0.010	−16.9 ± 1.2	0.5 ± 1.5	1.33 ± 0.07	8 ± 28	0.27	
15†	18.4 ± 2.7	78.8 ± 2.3	−17.6 ± 2.2	7.1 ± 1.0	36.78 ± 5.4	39.3 ± 5.8	−7.7 ± 1.1	20.1 ± 2.3	−8.8 ± 2.1	0.7 ± 1.1	37 ± 35	0.13	
16	5.6542 ± 0.0258	27.276 ± 0.035	−10.930 ± 0.039	−6.8 ± 0.4	112.43 ± 0.51	135.25 ± 0.62	18.61 ± 0.10	12.2 ± 0.3	−22.0 ± 0.3	−4.51 ± 0.07	204 ± 16	0.01	
17	1.1687 ± 0.0240	8.010 ± 0.045	−0.711 ± 0.045	−14.7 ± 0.3	504 ± 10	651 ± 13	232 ± 5	15.3 ± 0.5	−32.1 ± 0.5	4.2 ± 0.3	11 ± 23	1.66	
18	6.9947 ± 0.0256	47.790 ± 0.048	−54.249 ± 0.042	…	72.90 ± 0.27	107.29 ± 0.39	60.13 ± 0.22	…	…	…	…	…	SB2, VB
19	5.4731 ± 0.0333	40.407 ± 0.045	−30.676 ± 0.061	…	121.53 ± 0.74	133.34 ± 0.81	28.89 ± 0.20	…	…	…	…	…	SB2
20	1.2991 ± 0.0357	7.673 ± 0.075	−4.235 ± 0.065	…	591 ± 16	491 ± 13	−51.7 ± 1.5	…	…	…	…	…	SB2
21	28.8414 ± 0.0377	−106.525 ± 0.045	−14.385 ± 0.059	−10.9 ± 1.0	25.409 ± 0.034	23.550 ± 0.032	1.404 ± 0.015	−20.0 ± 0.7	4.1 ± 0.7	−3.90 ± 0.04	17 ± 36	0	
22	14.7594 ± 0.0241	58.050 ± 0.035	−48.909 ± 0.041	−10.332 ± 0.041	44.692 ± 0.074	48.947 ± 0.080	14.048 ± 0.030	3.40 ± 0.04	−25.80 ± 0.04	−4.88 ± 0.03	273 ± 14	0.07	
23	19.7872 ± 0.2785	−67.072 ± 0.353	54.409 ± 0.435	…	35.72 ± 0.51	35.03 ± 0.50	7.14 ± 0.20	…	…	…	…	…	SB2
24	44.3712 ± 0.0418	106.167 ± 0.112	−195.529 ± 0.076	25.2 ± 2.4	17.338 ± 0.017	14.398 ± 0.015	0.129 ± 0.010	26.5 ± 1.8	−4.3 ± 1.5	−21.87 ± 0.02	31 ± 49	0	
25	9.2418 ± 0.0296	−55.973 ± 0.044	−47.168 ± 0.044	−22.2 ± 0.7	80.98 ± 0.26	70.72 ± 0.23	12.22 ± 0.05	−38.1 ± 0.5	−5.5 ± 0.5	−20.5 ± 0.1	0 ± 28	0.19	VB
26	20.9650 ± 0.0303	−57.998 ± 0.045	0.564 ± 0.048	3.2 ± 1.2	36.664 ± 0.054	29.943 ± 0.045	5.856 ± 0.018	−5.8 ± 0.9	10.1 ± 0.8	−6.8 ± 0.1	28 ± 81	0	
27	1.2592 ± 0.0232	−1.625 ± 0.040	−4.432 ± 0.039	−35.9 ± 0.6	493 ± 9	566 ± 10	259 ± 5	−32.1 ± 0.4	−21.7 ± 0.5	10.2 ± 0.3	56 ± 24	0.41	
28	6.5852 ± 0.0215	34.434 ± 0.038	−44.658 ± 0.044	…	77.98 ± 0.26	112.44 ± 0.37	65.86 ± 0.22	…	…	…	…	…	SB2
29	…	…	…	−7.2 ± 0.8	…	…	…	…	…	…	35 ± 58	…	
30	28.7320 ± 0.0629	60.480 ± 0.089	52.074 ± 0.089	−7.2 ± 0.8	28.197 ± 0.063	19.911 ± 0.046	4.449 ± 0.022	1.0 ± 0.6	−3.0 ± 0.5	14.7 ± 0.1	37 ± 37	0	
31 c1	1.8134 ± 0.0309	16.712 ± 0.048	−14.941 ± 0.050	−44.7 ± 0.5	446.9 ± 7.6	314.1 ± 5.4	75.7 ± 1.3	−16.7 ± 0.6	−69.8 ± 0.7	16.6 ± 0.7	11 ± 35	0.83	
31 c2	7.4244 ± 0.0323	−4.818 ± 0.050	−65.643 ± 0.045	18.0 ± 0.7	109.17 ± 0.48	76.70 ± 0.34	18.46 ± 0.09	7.1 ± 0.6	−21.2 ± 0.4	−39.9 ± 0.2	59 ± 39	0.21	
32	16.0546 ± 0.0294	46.852 ± 0.038	−65.595 ± 0.048	…	37.640 ± 0.071	43.835 ± 0.081	23.269 ± 0.045	…	…	…	131 ± 10	0.06	SB1
33	5.9174 ± 0.0310	4.733 ± 0.042	−22.797 ± 0.059	…	110.62 ± 0.58	113.38 ± 0.60	58.88 ± 0.31	…	…	…	196 ± 30	0	Likely an SB2 system
34	18.8651 ± 0.0766	0.455 ± 0.088	−103.492 ± 0.133	6.3 ± 1.4	40.439 ± 0.167	31.143 ± 0.132	14.305 ± 0.067	−2.1 ± 1.1	19.3 ± 0.8	−18.4 ± 0.4	44 ± 107	0.13	
35	11.9227 ± 0.1175	28.985 ± 0.157	−151.159 ± 0.192	−94.7 ± 0.6	53.39 ± 0.53	56.83 ± 0.57	30.88 ± 0.31	−74.6 ± 0.6	−71.0 ± 0.5	45.9 ± 0.4	104 ± 52	0.24	SB2?
36	17.4243 ± 1.3576	47.673 ± 1.903	−56.696 ± 1.902	−7.19 ± 0.34	40.4 ± 3.2	36.3 ± 2.9	18.7 ± 1.6	−1.88 ± 0.95	−21.02 ± 0.96	3.5 ± 1.1	46 ± 23	0.57	
37 c1	2.9523 ± 0.9175	10.377 ± 1.508	2.675 ± 1.446	…	234 ± 73	216 ± 67	115 ± 36	…	…	…	…	…	SB3
37 c2	3.2707 ± 0.0247	11.665 ± 0.037	8.623 ± 0.043	−53.9 ± 0.6	203.0 ± 1.5	187.3 ± 1.4	131.2 ± 1.0	−20.1 ± 0.4	13.8 ± 0.4	52.5 ± 0.3	39 ± 33	0.08	SB2?
38	19.1742 ± 0.0778	47.633 ± 0.085	−118.803 ± 0.113	18.2 ± 1.2	41.94 ± 0.17	26.97 ± 0.12	15.28 ± 0.07	12.1 ± 1.0	−30.3 ± 0.6	−16.3 ± 0.4	12 ± 34	0	VB
39	22.9945 ± 0.0554	−31.231 ± 0.083	48.491 ± 0.118	−10.4 ± 3.1	26.080 ± 0.071	29.316 ± 0.077	18.754 ± 0.046	−6.3 ± 1.9	12.9 ± 2.1	6.6 ± 1.3	0 ± 50	0.51	
40 c1	7.4974 ± 0.0222	−2.118 ± 0.032	19.196 ± 0.040	−6.6 ± 0.4	88.29 ± 0.26	82.99 ± 0.25	55.75 ± 0.17	−0.2 ± 0.3	12.2 ± 0.3	6.7 ± 0.2	1 ± 44	0.26	
40 c2	7.4445 ± 0.0401	−2.593 ± 0.053	16.775 ± 0.078	…	88.92 ± 0.48	83.58 ± 0.45	56.15 ± 0.30	…	…	…	…	…	SB2
40 c3	3.0993 ± 0.0479	−14.653 ± 0.067	−28.313 ± 0.099	−32.9 ± 0.7	213.6 ± 3.3	200.7 ± 3.1	134.9 ± 2.1	−53.8 ± 0.7	−23.7 ± 0.6	0.5 ± 0.5	7 ± 56	0.21	
41	8.5741 ± 0.0262	0.767 ± 0.049	−50.389 ± 0.053	…	69.29 ± 0.21	78.62 ± 0.24	51.18 ± 0.16	…	…	…	8 ± 17	0	SB1
42 c1	6.9216 ± 0.0477	−10.073 ± 0.065	3.677 ± 0.075	−9.06 ± 0.44	95.90 ± 0.66	88.5 ± 0.61	62.01 ± 0.43	−9.2 ± 0.3	6.8 ± 0.3	2.4 ± 0.2	99 ± 10	0	
42 c2	3.2707 ± 0.0247	11.665 ± 0.037	8.623 ± 0.043	−20.9 ± 0.6	203.0 ± 1.5	187.3 ± 1.4	131.20 ± 0.99	1.8 ± 0.4	7.8 ± 0.4	28.5 ± 0.3	11 ± 126	0	
43	5.7831 ± 0.0218	4.642 ± 0.032	−22.886 ± 0.041	−86.14 ± 1.62	88.53 ± 0.34	126.03 ± 0.48	78.60 ± 0.30	−49.9 ± 0.8	0.3 ± 1.2	72.8 ± 0.7	34 ± 48	0	SB2?, VB
44 c1	4.1646 ± 0.0237	−4.263 ± 0.039	−41.491 ± 0.042	10 ± 15	138.72 ± 0.79	162.15 ± 0.92	110.10 ± 0.63	−19 ± 9	−43 ± 10	−11 ± 7	7 ± 15	0	
44 c2	2.4455 ± 0.0231	−1.912 ± 0.039	−31.611 ± 0.042	−21.1 ± 0.7	236.1 ± 2.2	276.2 ± 2.6	187.5 ± 1.8	−42.8 ± 0.6	−46.9 ± 0.6	13.4 ± 0.3	9 ± 15	0	
45	6.4866 ± 0.0274	−12.031 ± 0.039	5.834 ± 0.045	−8.54 ± 0.11	101.11 ± 0.43	91.64 ± 0.39	71.73 ± 0.30	−8.84 ± 0.08	9.48 ± 0.07	−0.64 ± 0.07	73 ± 16	0	
46	7.1974 ± 0.0844	2.489 ± 0.145	−51.861 ± 0.133	−15.725 ± 0.081	91.10 ± 1.07	82.41 ± 0.97	64.91 ± 0.76	−25.3 ± 0.3	−25.3 ± 0.3	11.6 ± 0.1	178 ± 14	0.01	Likely an SB2 system
47	7.9920 ± 0.0264	−7.424 ± 0.037	−89.250 ± 0.049	−55 ± 17	78.32 ± 0.26	75.30 ± 0.25	62.06 ± 0.21	−63 ± 11	−19 ± 10	39 ± 8	7 ± 12	0.38	SB2?, VB
48	76.3524 ± 0.0354	−291.565 ± 0.063	−599.348 ± 0.077	…	7.4080 ± 0.0034	8.7695 ± 0.0041	6.3049 ± 0.0029	…	…	…	…	…	No obs
49	10.8249 ± 0.0274	−101.079 ± 0.057	−137.703 ± 0.067	…	55.10 ± 0.14	56.49 ± 0.15	48.03 ± 0.12	…	…	…	28 ± 13	0	SB1
50	5.5026 ± 0.0186	−18.795 ± 0.036	−23.996 ± 0.038	…	93.26 ± 0.32	129.53 ± 0.44	86.90 ± 0.29	…	…	…	…	…	SB2

Table 4. Continued.

#⋆	π [mas]	$\mu_\alpha \cos\delta$ [mas yr^{-1}]	μ_δ [mas yr^{-1}]	$\langle RV \rangle$ [km s^{-1}]	X [pc]	Y [pc]	Z [pc]	U$_\odot$ [km s^{-1}]	V$_\odot$ [km s^{-1}]	W$_\odot$ [km s^{-1}]	$\langle W_{\rm Li} \rangle$ [mÅ]	A$_v$ [mag]	Note
51	14.8348 ± 0.0256	−41.177 ± 0.047	−61.103 ± 0.044	−7.8 ± 0.4	37.237 ± 0.067	43.156 ± 0.076	35.985 ± 0.064	−23.2 ± 0.2	−8.5 ± 0.3	2.7 ± 0.2	14 ± 10	0.10	
52	2.5699 ± 0.0295	20.772 ± 0.069	−7.142 ± 0.072	…	201.9 ± 2.3	269.3 ± 3.1	195.2 ± 2.2	…	…	…	76 ± 16	0	SB1
53	5.8065 ± 0.0851	24.885 ± 0.131	0.041 ± 0.196	…	94.1 ± 1.4	97.2 ± 1.4	106.6 ± 1.6	…	…	…	…	…	No Obs
54	24.9252 ± 0.0482	110.257 ± 0.084	10.349 ± 0.076	…	19.726 ± 0.040	26.901 ± 0.054	22.289 ± 0.048	…	…	…	…	…	No Obs
55	13.7809 ± 0.0560	−60.794 ± 0.078	−25.573 ± 0.060	…	35.19 ± 0.15	49.03 ± 0.20	40.30 ± 0.17	…	…	…	…	…	No Obs, VB
56	3.2342 ± 0.0213	−18.996 ± 0.039	19.453 ± 0.032	…	142.5 ± 0.9	214.1 ± 1.4	171.6 ± 1.1	…	…	…	…	…	No Obs, VB
57	9.2549 ± 0.0876	−51.835 ± 0.184	−5.563 ± 0.142	…	50.13 ± 0.48	75.72 ± 0.72	58.56 ± 0.57	…	…	…	…	…	No Obs, VB
58	4.2768 ± 0.0502	−33.077 ± 0.107	20.811 ± 0.075	…	91.9 ± 1.1	145.8 ± 1.7	158.1 ± 1.9	…	…	…	…	…	No Obs
59	2.8816 ± 0.0262	−10.664 ± 0.048	−5.061 ± 0.044	…	165.0 ± 1.5	255.7 ± 2.3	166.8 ± 1.5	…	…	…	…	…	No Obs
60	3.1480 ± 0.0238	8.920 ± 0.054	−43.060 ± 0.040	…	126.52 ± 0.95	218.3 ± 1.7	193.0 ± 1.5	…	…	…	…	…	No Obs
61	11.0816 ± 0.0209	−53.993 ± 0.043	2.051 ± 0.034	…	33.33 ± 0.06	61.05 ± 0.12	57.49 ± 0.11	…	…	…	…	…	No Obs
62	75.4702 ± 0.0477	224.138 ± 0.083	−15.142 ± 0.074	…	4.9439 ± 0.0051	9.0343 ± 0.0075	8.3372 ± 0.0083	…	…	…	…	…	No Obs
63	3.8375 ± 0.0262	−59.593 ± 0.051	−15.637 ± 0.040	…	65.38 ± 0.45	164.6 ± 1.1	191.2 ± 1.3	…	…	…	…	…	No Obs
64	3.0534 ± 0.0193	−44.860 ± 0.039	31.579 ± 0.039	…	47.12 ± 0.31	199.4 ± 1.3	255.5 ± 1.6	…	…	…	…	…	No Obs
65	6.2061 ± 0.0534	4.768 ± 0.115	14.430 ± 0.087	…	18.02 ± 0.19	100.46 ± 0.87	124.68 ± 1.07	…	…	…	…	…	No Obs
66	6.6284 ± 0.0305	−38.712 ± 0.052	22.158 ± 0.048	…	39.06 ± 0.18	104.30 ± 0.48	101.77 ± 0.47	…	…	…	…	…	No Obs, VB
67	2.4303 ± 0.0206	9.664 ± 0.044	12.593 ± 0.039	…	85.27 ± 0.73	280.8 ± 2.4	288.5 ± 2.4	…	…	…	…	…	No Obs
68	5.0937 ± 0.0235	−21.055 ± 0.039	50.833 ± 0.040	…	66.38 ± 0.31	147.60 ± 0.68	111.13 ± 0.51	…	…	…	…	…	No Obs
69	20.201 ± 0.9409	−28.939 ± 1.691	−63.378 ± 1.797	…	13.61 ± 0.86	37.0 ± 1.8	30.0 ± 1.5	…	…	…	…	…	No Obs, VB
70	38.9953 ± 0.0241	−44.449 ± 0.055	132.876 ± 0.050	−13.75 ± 2.08	4.3145 ± 0.0093	19.021 ± 0.013	16.650 ± 0.011	4.2 ± 0.4	−8.3 ± 1.5	−19.8 ± 1.4	39 ± 33	0	SB1?
71	20.6676 ± 1.1712	46.597 ± 2.011	15.837 ± 2.412	2.1 ± 0.5	9.2 ± 1.0	36.5 ± 2.1	30.4 ± 1.8	10.7 ± 0.6	3.7 ± 0.6	1.6 ± 0.6	7 ± 29	0.10	
72	2.7087 ± 0.0198	−2.164 ± 0.046	25.359 ± 0.045	…	67.53 ± 0.51	279.6 ± 2.0	231.4 ± 1.7	…	…	…	…	…	No Obs
73	13.236 ± 0.0635	−65.135 ± 0.121	−109.923 ± 0.125	−8.2 ± 2.8	21.68 ± 0.12	58.28 ± 0.28	42.91 ± 0.21	−42.7 ± 0.8	15.4 ± 2.2	10.0 ± 1.6	23 ± 66	0.04	SB2?
74	5.3235 ± 0.0613	12.598 ± 0.122	17.661 ± 0.120	…	21.41 ± 0.30	144.7 ± 1.7	117.9 ± 1.4	…	…	…	…	…	No Obs
75	13.6064 ± 0.0584	35.568 ± 0.111	−2.158 ± 0.121	…	2.951 ± 0.062	56.11 ± 0.24	47.37 ± 0.21	…	…	…	…	…	No Obs
76	3.5706 ± 0.0319	−9.927 ± 0.050	12.871 ± 0.062	…	59.48 ± 0.55	220.0 ± 2.0	162.8 ± 1.5	…	…	…	…	…	SB2
77	4.9581 ± 0.0220	−6.434 ± 0.037	9.490 ± 0.049	37.2 ± 2.1	33.81 ± 0.17	161.16 ± 0.72	116.46 ± 0.52	6.6 ± 0.4	−18.1 ± 1.7	33.7 ± 1.2	7 ± 28	0	SB2?
78	3.4832 ± 0.0344	−19.142 ± 0.060	−15.277 ± 0.073	…	68.23 ± 0.69	230.8 ± 2.3	156.5 ± 1.5	…	…	…	…	…	SB2
79	3.1255 ± 0.0227	−15.645 ± 0.047	1.572 ± 0.053	…	24.81 ± 0.24	264.1 ± 1.9	179.0 ± 1.3	…	…	…	…	…	SB2
80	25.5038 ± 0.0242	−15.571 ± 0.050	88.112 ± 0.047	−26.9 ± 2.3	11.912 ± 0.019	31.700 ± 0.031	19.770 ± 0.019	−2.3 ± 0.7	−14.2 ± 1.9	−28.2 ± 1.2	7 ± 69	0	
81 c1	18.4582 ± 0.0300	22.243 ± 0.057	−8.491 ± 0.054	−9.7 ± 1.1	21.475 ± 0.041	42.400 ± 0.070	26.003 ± 0.043	−0.4 ± 0.4	5.0 ± 0.9	−10.3 ± 0.5	29 ± 79	…	
81 c2	18.4850 ± 0.0246	23.474 ± 0.048	−13.040 ± 0.045	−10.5 ± 1.1	21.443 ± 0.029	42.339 ± 0.056	25.965 ± 0.035	−1.1 ± 0.4	6.2 ± 0.9	−10.9 ± 0.5	20 ± 80	…	
82	5.3350 ± 0.1333	9.708 ± 0.267	30.734 ± 0.302	19.26 ± 0.76	39.1 ± 1.1	157.2 ± 3.9	94.3 ± 2.4	25.0 ± 0.7	−18.6 ± 0.7	14.8 ± 0.5	6 ± 11	0	
83	8.7512 ± 0.0221	−22.065 ± 0.039	32.895 ± 0.047	−155.2 ± 1.5	14.077 ± 0.067	97.80 ± 0.25	57.39 ± 0.15	−20.4 ± 0.2	−27.7 ± 1.3	152.9 ± 0.8	15 ± 44	0	
84	6.2996 ± 0.0226	5.755 ± 0.041	30.190 ± 0.042	…	−6.375 ± 0.071	137.86 ± 0.49	78.44 ± 0.28	…	…	…	…	…	SB2
85	18.9468 ± 0.1350	25.464 ± 0.239	123.209 ± 0.229	−13.0 ± 1.6	6.78 ± 0.13	45.58 ± 0.33	25.73 ± 0.19	18.9 ± 0.3	−24.9 ± 1.4	−13.6 ± 0.8	11 ± 45	0	
86	9.1725 ± 0.0563	−6.353 ± 0.089	24.018 ± 0.113	−24.7 ± 2.7	17.64 ± 0.16	93.87 ± 0.58	52.57 ± 0.32	−0.8 ± 0.4	−14.8 ± 2.3	−23.6 ± 1.3	211 ± 9	0	SB1?
87	2.8321 ± 0.0211	−1.789 ± 0.037	−12.790 ± 0.041	…	−11.7 ± 0.16	313.1 ± 2.3	162.7 ± 1.2	…	…	…	29 ± 12	0	Likely an SB2 system
88	60.9596 ± 0.0417	123.984 ± 0.067	210.513 ± 0.079	8.9 ± 3.3	5.408 ± 0.013	13.528 ± 0.010	7.5390 ± 0.0054	18.4 ± 1.1	−8.8 ± 2.7	4.9 ± 1.5	42 ± 35	0.23	
89	6.1821 ± 0.0214	−4.278 ± 0.035	20.837 ± 0.049	…	31.45 ± 0.13	140.86 ± 0.49	73.03 ± 0.25	…	…	…	…	…	SB2
90	3.1178 ± 0.0136	2.981 ± 0.029	−32.215 ± 0.033	171.0 ± 5.9	43.69 ± 0.21	284.2 ± 1.2	142.06 ± 0.62	5.6 ± 0.8	79.4 ± 5.2	159.1 ± 2.6	19 ± 45	0.72	
91	2.9807 ± 0.0777	−17.761 ± 0.147	−6.453 ± 0.196	1.51 ± 0.20	24.22 ± 0.83	304.1 ± 7.9	139.6 ± 3.6	−29.8 ± 0.4	−1.5 ± 0.4	4.1 ± 0.7	29 ± 18	0.43	VB
92	4.8178 ± 0.0318	2.645 ± 0.063	2.795 ± 0.069	…	−4.63 ± 0.12	191.1 ± 1.3	80.85 ± 0.54	…	…	…	…	…	SB3
93	5.1302 ± 0.0273	4.877 ± 0.056	11.036 ± 0.045	−10.5 ± 1.1	34.07 ± 0.20	174.39 ± 0.93	80.15 ± 0.43	6.4 ± 0.2	−10.6 ± 1.0	−9.0 ± 0.5	200 ± 22	0	
94	4.6757 ± 0.0217	−30.967 ± 0.042	8.135 ± 0.041	−10.56 ± 0.30	−10.380 ± 0.090	200.74 ± 0.93	73.06 ± 0.34	−26.14 ± 0.07	−21.3 ± 0.3	−5.5 ± 0.2	24 ± 26	0	
95	8.8428 ± 0.0227	3.651 ± 0.049	23.806 ± 0.056	−18.4 ± 0.6	5.008 ± 0.057	105.37 ± 0.27	40.76 ± 0.11	5.60 ± 0.05	−16.7 ± 0.6	−13.9 ± 0.2	11 ± 48	0.45	
96	4.4582 ± 0.0349	1.089 ± 0.079	23.109 ± 0.059	−12.78 ± 0.47	25.87 ± 0.24	205.9 ± 1.6	85.16 ± 0.67	8.9 ± 0.2	−25.6 ± 0.4	−5.6 ± 0.2	28 ± 24	0	
97	4.5618 ± 0.0233	8.716 ± 0.051	37.931 ± 0.052	…	−9.00 ± 0.11	207.8 ± 1.1	69.24 ± 0.36	…	…	…	…	0.01	
98	…	…	…	−30.8 ± 0.5	…	…	…	…	…	…	119 ± 34	…	SB2?
99	0.6552 ± 0.0203	3.535 ± 0.043	−5.721 ± 0.048	−22.48 ± 0.05	219.5 ± 6.8	1397 ± 43	575 ± 18	4.6 ± 1.3	36.3 ± 0.4	−39.2 ± 0.8	16 ± 11	0.08	
100	7.2575 ± 0.7471	20.703 ± 1.708	55.176 ± 1.547	−15.6 ± 0.6	18.0 ± 2.5	127.4 ± 13.1	49.4 ± 5.2	23.4 ± 3.6	−33.8 ± 1.2	−6.2 ± 2.0	23 ± 19	0	VB
101 †	36.0 ± 6.9	78.1 ± 5.3	135.9 ± 5.2	−19.6 ± 0.5	−0.126 ± 0.024	26.4 ± 5.1	8.5 ± 1.6	15.4 ± 3.3	−20.3 ± 0.9	−12.7 ± 2.2	3 ± 13	0.09	
102	3.9580 ± 0.0213	6.072 ± 0.042	12.173 ± 0.040	−24.0 ± 0.7	36.77 ± 0.22	232.7 ± 1.3	91.37 ± 0.49	8.5 ± 0.1	−20.1 ± 0.6	−19.1 ± 0.3	166 ± 58	0.02	VB
103	2.7289 ± 0.0329	1.937 ± 0.066	18.633 ± 0.048	…	35.50 ± 0.46	342.3 ± 4.1	125.9 ± 1.5	…	…	…	…	…	SB2
104	1.9334 ± 0.0183	−9.797 ± 0.037	−11.373 ± 0.041	−27.96 ± 0.06	−10.45 ± 0.20	493.9 ± 4.7	153.1 ± 1.5	−30.6 ± 0.3	6.70 ± 0.09	−34.0 ± 0.2	17 ± 14	0.40	
105	6.7536 ± 0.0191	1.544 ± 0.033	−24.437 ± 0.041	…	61.81 ± 0.18	117.84 ± 0.33	64.94 ± 0.18	…	…	…	8.5 ± 8.1	0	SB1
106 c1	5.3075 ± 0.0202	4.973 ± 0.041	8.978 ± 0.044	−14.0 ± 1.6	24.04 ± 0.11	175.84 ± 0.67	63.27 ± 0.24	5.1 ± 0.2	−11.8 ± 1.5	−10.7 ± 0.5	249 ± 23	0	
106 c2	1.5153 ± 0.0161	4.395 ± 0.032	−2.662 ± 0.037	−13.6 ± 0.7	84.02 ± 0.89	615.9 ± 6.5	221.5 ± 2.4	8.3 ± 0.2	4.9 ± 0.7	−18.7 ± 0.3	28 ± 93	0.02	
107	12.2966 ± 0.0554	33.271 ± 0.106	−32.095 ± 0.117	8.6 ± 0.9	16.22 ± 0.11	74.19 ± 0.33	29.10 ± 0.14	9.0 ± 0.2	17.6 ± 0.8	−1.1 ± 0.3	3 ± 23	0.10	

Table 4. Continued.

#⋆	π [mas]	$\mu_\alpha \cos\delta$ [mas yr^{-1}]	μ_δ [mas yr^{-1}]	$\langle RV \rangle$ [km s^{-1}]	X [pc]	Y [pc]	Z [pc]	U$_\odot$ [km s^{-1}]	V$_\odot$ [km s^{-1}]	W$_\odot$ [km s^{-1}]	$\langle W_{\rm Li} \rangle$ [mÅ]	A$_v$ [mag]	Note
108	...	−7.436 ± 1.367	1.816 ± 1.254	−30.6 ± 0.3	...	...	...	...	...	...	25 ± 13	...	
109	2.4886 ± 0.0235	6.109 ± 0.047	10.938 ± 0.053	−65.1 ± 0.8	60.27 ± 0.59	375.9 ± 3.5	128.7 ± 1.2	7.8 ± 0.2	−45.9 ± 0.8	−51.4 ± 0.3	96 ± 27	0.50	SB2?, VB
110	8.0362 ± 0.0372	7.506 ± 0.079	39.679 ± 0.096	...	19.23 ± 0.13	116.39 ± 0.54	39.59 ± 0.19	...	...	...	...	...	SB2
111	11.511 ± 0.0169	0.985 ± 0.032	−41.117 ± 0.035	−8.8 ± 0.9	23.649 ± 0.042	77.23 ± 0.11	31.984 ± 0.048	−8.3 ± 0.3	10.2 ± 0.8	−13.9 ± 0.3	13 ± 60	0	
112	14.4045 ± 0.0436	13.28 ± 0.084	28.408 ± 0.071	−23.76 ± 1.04	−3.292 ± 0.046	67.08 ± 0.20	17.584 ± 0.062	5.46 ± 0.06	−18.8 ± 1.0	−17.0 ± 0.3	158 ± 8	0.27	
113	27.1943 ± 0.1297	−9.618 ± 0.300	−99.601 ± 0.243	−3.1 ± 0.6	4.608 ± 0.071	34.87 ± 0.17	10.739 ± 0.069	−7.0 ± 0.1	12.8 ± 0.6	−10.0 ± 0.2	22 ± 30	0.09	
114	7.5609 ± 0.0199	23.899 ± 0.043	45.681 ± 0.037	−13.74 ± 0.06	21.133 ± 0.067	124.84 ± 0.33	38.23 ± 0.10	20.2 ± 0.07	−28.63 ± 0.06	−2.19 ± 0.06	29 ± 10	0	
115	6.2609 ± 0.0195	9.216 ± 0.035	13.006 ± 0.037	−11.29 ± 0.08	43.88 ± 0.14	143.80 ± 0.45	53.90 ± 0.17	6.50 ± 0.04	−13.44 ± 0.07	−7.09 ± 0.04	291 ± 6	0	
116	1.5591 ± 0.0237	−11.737 ± 0.047	−17.026 ± 0.044	−9.7 ± 0.9	60.45 ± 0.94	625.9 ± 9.5	126.6 ± 1.9	−46.0 ± 0.7	31.9 ± 0.9	−30.3 ± 0.7	112 ± 25	0.58	SB2?
117	0.6502 ± 0.0323	2.313 ± 0.051	1.043 ± 0.056	−65.7 ± 0.7	56.4 ± 2.9	1517 ± 75	237 ± 12	15.4 ± 0.7	−43.4 ± 0.7	−50.4 ± 0.8	8 ± 35	0.88	
118	6.8174 ± 0.0533	−9.090 ± 0.104	−30.432 ± 0.110	−3.8 ± 0.5	33.49 ± 0.29	136.5 ± 1.1	41.98 ± 0.34	−12.8 ± 0.2	13.9 ± 0.5	−12.0 ± 0.2	6 ± 32	0.41	
119	3.6599 ± 0.0173	7.367 ± 0.033	−7.720 ± 0.035	...	20.26 ± 0.12	268.3 ± 1.3	47.62 ± 0.23	...	...	...	...	...	SB2, VB
120	5.7303 ± 0.0288	17.652 ± 0.067	−4.347 ± 0.060	−20.1 ± 0.9	27.50 ± 0.16	167.40 ± 0.84	40.91 ± 0.22	10.0 ± 0.2	−7.8 ± 0.9	−21.7 ± 0.2	22 ± 27	0	VB
121	15.9895 ± 0.0465	−43.788 ± 0.112	−66.512 ± 0.085	−24.4 ± 0.5	7.831 ± 0.047	61.12 ± 0.18	10.708 ± 0.048	−19.12 ± 0.08	−1.2 ± 0.5	−28.0 ± 0.1	0 ± 54	0	
122	5.3036 ± 0.0247	26.598 ± 0.050	31.165 ± 0.048	11.39 ± 0.57	60.64 ± 0.29	168.37 ± 0.78	59.38 ± 0.28	33.7 ± 0.2	−12.6 ± 0.5	13.4 ± 0.2	41 ± 20	0.26	
123	3.4269 ± 0.0251	8.190 ± 0.050	5.784 ± 0.050	−22.4 ± 0.5	11.21 ± 0.14	291.0 ± 2.1	18.33 ± 0.17	10.9 ± 0.1	−20.7 ± 0.5	−12.1 ± 0.1	176 ± 27	0	Multiple system
124	4.1805 ± 0.0346	9.568 ± 0.057	6.836 ± 0.057	−13.50 ± 1.04	60.84 ± 0.51	223.6 ± 1.9	59.46 ± 0.50	8.6 ± 0.3	−14.7 ± 1.0	−8.3 ± 0.3	412 ± 39	0	VB
125	3.4229 ± 0.0223	6.410 ± 0.041	6.161 ± 0.042	−21.44 ± 0.09	44.38 ± 0.30	285.5 ± 1.9	43.53 ± 0.29	6.69 ± 0.08	−20.80 ± 0.09	−11.57 ± 0.08	181 ± 37	0.15	Multiple system
126	8.8830 ± 0.0254	13.314 ± 0.047	−25.113 ± 0.044	37.8 ± 0.6	31.089 ± 0.097	104.05 ± 0.30	29.657 ± 0.092	13.5 ± 0.2	35.6 ± 0.6	14.5 ± 0.2	47 ± 16	0	
127	5.2719 ± 0.0222	5.876 ± 0.044	39.134 ± 0.043	...	31.83 ± 0.14	184.51 ± 0.78	30.39 ± 0.14	...	...	...	177 ± 86	0.07	
128	3.6596 ± 0.0202	12.548 ± 0.044	7.840 ± 0.038	−18.9 ± 0.1	86.93 ± 0.49	245.8 ± 1.4	81.67 ± 0.46	11.7 ± 0.1	−20.4 ± 0.1	−13.2 ± 0.1	50 ± 10	0.33	SB3?
129	4.4840 ± 0.0419	14.574 ± 0.075	9.986 ± 0.070	−20.53 ± 0.50	28.60 ± 0.29	219.9 ± 2.1	23.82 ± 0.25	13.7 ± 0.2	−22.1 ± 0.5	−9.8 ± 0.2	147 ± 35	0	
130	8.5911 ± 0.0294	22.051 ± 0.055	9.817 ± 0.048	...	13.892 ± 0.064	115.31 ± 0.39	7.577 ± 0.050	...	...	...	244 ± 88	0.07	
131	6.7559 ± 0.0739	30.093 ± 0.165	11.946 ± 0.136	...	29.72 ± 0.35	143.5 ± 1.6	20.84 ± 0.27	...	...	...	...	...	SB2, VB
132	2.3376 ± 0.0228	−4.435 ± 0.038	14.822 ± 0.037	42.1 ± 0.4	127.3 ± 1.2	395.4 ± 3.9	102.2 ± 1.0	11.4 ± 0.2	11.0 ± 0.4	50.1 ± 0.2	47 ± 22	0.64	
133	2.8409 ± 0.0221	20.435 ± 0.040	15.224 ± 0.051	...	141.2 ± 1.1	297.6 ± 2.3	124.2 ± 1.0	...	...	...	73 ± 7	0.83	SB1
134	4.8381 ± 0.0433	−29.203 ± 0.074	12.606 ± 0.082	...	44.78 ± 0.42	200.7 ± 1.8	21.26 ± 0.23	...	...	...	...	...	SB2
135	2.4955 ± 0.0229	11.907 ± 0.046	26.296 ± 0.049	−37.3 ± 0.7	79.27 ± 0.74	391.7 ± 3.6	29.26 ± 0.30	18.4 ± 0.4	−62.7 ± 0.7	11.4 ± 0.4	29 ± 27	0	VB
136	12.1772 ± 0.0319	43.307 ± 0.067	6.028 ± 0.058	−7.2 ± 0.6	15.814 ± 0.051	80.57 ± 0.21	1.352 ± 0.035	15.2 ± 0.1	−9.5 ± 0.6	−4.50 ± 0.04	44 ± 26	0.59	
137	3.7221 ± 0.0237	15.461 ± 0.040	−2.988 ± 0.041	...	77.94 ± 0.50	254.2 ± 1.6	38.60 ± 0.26	...	...	...	...	0.09	
138 c1	0.7272 ± 0.0222	5.052 ± 0.044	−3.012 ± 0.041	−69.75 ± 0.42	345 ± 11	1326 ± 40	113.1 ± 3.5	12.6 ± 0.9	−49.1 ± 0.5	−61.4 ± 0.8	22 ± 14	1.05	
138 c2	0.5547 ± 0.0176	−3.437 ± 0.034	−2.566 ± 0.032	...	453 ± 14	1739 ± 55	148.3 ± 4.7	...	...	...	62 ± 82	0.96	
139	1.1202 ± 0.0288	−0.286 ± 0.057	−3.048 ± 0.052	...	245.7 ± 6.3	853 ± 22	92.0 ± 2.4	...	...	...	...	0.44	
140 c1	4.6715 ± 0.0166	15.432 ± 0.028	2.258 ± 0.029	−16.3 ± 0.6	44.11 ± 0.16	209.39 ± 0.74	−5.955 ± 0.051	11.9 ± 0.1	−17.4 ± 0.6	−8.46 ± 0.05	37 ± 62	0	VB
140 c2	0.8896 ± 0.0234	−0.651 ± 0.040	−3.487 ± 0.041	−17.5 ± 1.6	231.7 ± 6.1	1100 ± 29	−31.222 ± 0.82	−6.5 ± 0.5	−3.2 ± 1.6	−24.7 ± 0.5	21 ± 43	0.93	
141	9.3979 ± 0.0199	146.72 ± 0.037	17.614 ± 0.035	60.85 ± 0.07	36.436 ± 0.080	97.96 ± 0.21	19.945 ± 0.051	90.6 ± 0.1	30.5 ± 0.1	10.7 ± 0.1	16 ± 12	0.04	
142	6.1631 ± 0.0258	17.354 ± 0.047	7.584 ± 0.046	−9.05 ± 0.54	62.53 ± 0.27	143.99 ± 0.60	41.03 ± 0.18	9.8 ± 0.2	−13.2 ± 0.5	−4.7 ± 0.1	432 ± 25	0	Cep III member
143	13.6259 ± 0.0236	59.780 ± 0.044	49.546 ± 0.034	−17.2 ± 1.1	34.795 ± 0.062	56.240 ± 0.098	31.819 ± 0.058	15.3 ± 0.5	−27.6 ± 0.8	−5.6 ± 0.5	4 ± 62	0.30	
144	8.7382 ± 0.0309	−4.442 ± 0.048	−6.498 ± 0.042	20.90 ± 0.08	38.93 ± 0.14	106.26 ± 0.38	17.026 ± 0.073	4.35 ± 0.04	19.64 ± 0.07	7.10 ± 0.03	35 ± 11	0.24	VB
145	4.0426 ± 0.0235	22.659 ± 0.044	23.516 ± 0.040	−31.43 ± 0.06	91.34 ± 0.53	225.4 ± 1.3	45.38 ± 0.28	17.7 ± 0.2	−46.3 ± 0.1	1.7 ± 0.2	66 ± 9	0.52	
146	20.4651 ± 0.0262	144.623 ± 0.042	−38.632 ± 0.042	−47.9 ± 1.2	16.099 ± 0.024	45.935 ± 0.059	4.299 ± 0.019	14.9 ± 0.4	−44.2 ± 1.1	−36.3 ± 0.1	77 ± 64	0	VB
147	1.5399 ± 0.0263	−10.450 ± 0.040	−4.875 ± 0.038	...	164.8 ± 2.8	624 ± 11	−68.7 ± 1.2	...	...	...	...	...	SB2
148	2.0655 ± 0.0185	−12.114 ± 0.034	2.945 ± 0.033	−17.543 ± 0.011	209.0 ± 1.9	413.6 ± 3.7	140.1 ± 1.3	−29.4 ± 0.2	−10.2 ± 0.1	12.7 ± 0.1	3 ± 4	0.50	
149	2.2842 ± 0.0251	5.193 ± 0.048	−0.221 ± 0.041	...	141.3 ± 1.6	414.3 ± 4.5	−1.40 ± 0.15	...	...	...	146 ± 71	0.23	Multiple system
150	2.6622 ± 0.0217	7.054 ± 0.037	−1.329 ± 0.033	−13.43 ± 0.48	142.5 ± 1.2	344.6 ± 2.8	45.55 ± 0.39	6.1 ± 0.2	−14.3 ± 0.4	−10.1 ± 0.1	208 ± 47	0.36	
151	41.5395 ± 0.0282	173.626 ± 0.046	−58.869 ± 0.039	−23.22 ± 0.22	8.8728 ± 0.0078	22.334 ± 0.015	1.4204 ± 0.0089	9.43 ± 0.08	−23.7 ± 0.2	−18.1 ± 0.02	44 ± 18	0.93	
152	7.0082 ± 0.0198	22.582 ± 0.037	4.888 ± 0.037	−8.8 ± 0.9	64.00 ± 0.18	120.30 ± 0.34	42.35 ± 0.13	9.9 ± 0.4	−13.8 ± 0.8	−5.7 ± 0.3	428 ± 98	0.95	SB2?, VB, Cep III member
153	6.1071 ± 0.0229	21.034 ± 0.046	4.317 ± 0.034	...	74.11 ± 0.28	138.21 ± 0.52	47.08 ± 0.18	...	...	...	442 ± 26	0.37	SB1, Cep II member
154	6.0218 ± 1.1249	−6.251 ± 1.790	−27.815 ± 1.871	...	60 ± 11	155 ± 29	−8.4 ± 3.2	...	...	...	18 ± 34	0	SB1
155	...	...	...	...	...	...	...	...	...	...	...	...	SB3
156	6.0080 ± 0.6900	17.991 ± 1.375	9.678 ± 1.053	−7.7 ± 2.2	75.8 ± 8.7	142 ± 16	43.0 ± 5.2	10.6 ± 2.0	−14.4 ± 2.0	0.3 ± 1.4	465 ± 24	0.39	Likely SB1 system, Cep III member
157	7.8348 ± 0.0488	8.660 ± 0.064	−1.105 ± 0.073	−10.958 ± 0.007	58.67 ± 0.37	109.60 ± 0.68	28.92 ± 0.20	−0.69 ± 0.04	−11.45 ± 0.03	−4.04 ± 0.04	52 ± 7	0	VB
158	6.6269 ± 0.0296	23.351 ± 0.056	1.640 ± 0.043	−8.56 ± 0.25	71.97 ± 0.32	125.93 ± 0.56	41.62 ± 0.19	10.2 ± 0.1	−14.8 ± 0.2	−5.5 ± 0.1	344 ± 16	0.16	Cep II member
159	1.8441 ± 0.0369	13.252 ± 0.047	17.193 ± 0.036	...	224.3 ± 4.5	488.3 ± 9.8	−72.8 ± 1.5	...	...	...	90 ± 26	0.63	SB1 or SB2?
160	2.8245 ± 0.0701	6.988 ± 0.123	0.194 ± 0.112	...	142.6 ± 3.5	311.5 ± 7.7	89.3 ± 2.2	...	...	...	...	...	No Obs, VB
161	19.7195 ± 0.0352	168.459 ± 0.053	21.141 ± 0.048	−7.85 ± 1.01	16.662 ± 0.033	47.881 ± 0.086	−1.192 ± 0.022	35.5 ± 0.3	−21.3 ± 1.0	−3.00 ± 0.04	66 ± 34	0	
162	3.5435 ± 0.0276	−5.603 ± 0.041	−19.832 ± 0.040	...	116.15 ± 0.91	257.2 ± 2.0	2.28 ± 0.11	...	...	...	...	...	SB2
163 c1	2.3150 ± 0.3444	1.808 ± 0.643	−4.241 ± 0.541	−45.3 ± 0.6	207 ± 31	370 ± 55	84 ± 13	−20.2 ± 1.3	−39.5 ± 0.9	13.1 ± 1.7	35 ± 19	0.93	SB2?
163 c2	1.3287 ± 0.0176	1.946 ± 0.026	1.397 ± 0.028	−4.3 ± 2.3	361.1 ± 4.8	644.1 ± 8.5	145.6 ± 1.9	4.8 ± 1.1	−7.8 ± 2.0	2.6 ± 0.5	2 ± 41	1.02	

Table 4. Continued.

#⋆	π [mas]	$\mu_\alpha \cos\delta$ [mas yr^{-1}]	μ_δ [mas yr^{-1}]	$\langle RV \rangle$ [km s^{-1}]	X [pc]	Y [pc]	Z [pc]	U$_\odot$ [km s^{-1}]	V$_\odot$ [km s^{-1}]	W$_\odot$ [km s^{-1}]	$\langle W_{\rm Li} \rangle$ [mÅ]	A$_v$ [mag]	Note
164	1.7550 ± 0.0227	17.782 ± 0.048	−5.156 ± 0.037	…	276.7 ± 3.6	476.0 ± 6.2	146.6 ± 1.9	…	…	…	…	…	SB2
165	0.8193 ± 0.0263	−2.022 ± 0.040	−2.205 ± 0.040	−32.1 ± 2.5	644 ± 21	1008 ± 32	240.1 ± 7.7	−29.1 ± 1.4	−20.6 ± 2.1	−7.6 ± 0.7	61 ± 43	0.76	
166	1.4660 ± 0.0258	−1.493 ± 0.046	−2.800 ± 0.042	−2.6 ± 1.3	374.4 ± 6.6	560.9 ± 9.9	102.7 ± 1.8	−6.8 ± 0.7	0.2 ± 1.1	−8.1 ± 0.3	51 ± 26	0.53	SB2?
167	2.2415 ± 0.0285	6.647 ± 0.044	−12.438 ± 0.042	…	251.9 ± 3.2	365.4 ± 4.6	45.39 ± 0.60	…	…	…	…	…	SB2
168 c1	3.3354 ± 0.0607	35.354 ± 0.119	−6.973 ± 0.104	−8.50 ± 0.90	170.7 ± 3.1	242.2 ± 4.4	45.66 ± 0.87	34.2 ± 0.9	−37.4 ± 0.9	−11.3 ± 0.3	17 ± 24	0	
168 c2	1.9104 ± 0.0273	15.207 ± 0.043	14.083 ± 0.047	−38.00 ± 0.61	298.1 ± 4.3	422.8 ± 6.0	79.7 ± 1.1	14.2 ± 0.6	−48.8 ± 0.6	38.8 ± 0.5	65 ± 44	…	
169 c1	3.7323 ± 0.0304	16.785 ± 0.044	−14.285 ± 0.047	…	159.7 ± 1.3	212.0 ± 1.7	36.46 ± 0.31	…	…	…	…	…	SB2
169 c2	1.0620 ± 0.0188	1.891 ± 0.026	−4.733 ± 0.029	−20.6 ± 0.6	561 ± 10	745 ± 13	128.2 ± 2.7	−8.47 ± 0.4	−24.9 ± 0.5	−15.8 ± 0.4	32 ± 35	1.10	
170	3.8271 ± 0.0294	35.034 ± 0.033	−24.659 ± 0.041	…	172.2 ± 1.3	194.0 ± 1.5	31.51 ± 0.26	…	…	…	…	…	No Obs, VB
171	2.0881 ± 0.0237	−1.111 ± 0.044	1.466 ± 0.045	…	149.2 ± 1.7	416.8 ± 4.7	182.5 ± 2.1	…	…	…	…	…	No Obs
172	1.4190 ± 0.0202	−2.503 ± 0.040	4.729 ± 0.048	…	236.1 ± 3.4	605.6 ± 8.6	272.3 ± 3.9	…	…	…	…	…	No Obs
173	3.3140 ± 0.0234	6.048 ± 0.066	6.157 ± 0.044	…	47.50 ± 0.35	286.0 ± 2.0	83.50 ± 0.60	…	…	…	…	…	No Obs
174 c1	5.1913 ± 0.0263	17.103 ± 0.049	15.759 ± 0.049	3.5 ± 3.9	64.13 ± 0.33	166.51 ± 0.84	72.59 ± 0.37	20.1 ± 1.3	−7.6 ± 3.4	1.3 ± 1.5	273 ± 53	0	
174 c2	2.3286 ± 0.0287	−5.234 ± 0.044	1.331 ± 0.050	−30.7 ± 0.7	143.0 ± 1.8	371.2 ± 4.6	161.8 ± 2.0	−18.4 ± 0.3	−20.6 ± 0.6	−17.3 ± 0.3	0 ± 30	0	
175	7.0641 ± 0.0212	13.429 ± 0.040	18.865 ± 0.038	…	34.59 ± 0.11	130.30 ± 0.39	43.19 ± 0.13	…	…	…	…	…	No Obs, VB
176	3.0180 ± 0.0258	0.069 ± 0.041	−1.761 ± 0.043	…	85.34 ± 0.74	304.6 ± 2.6	98.60 ± 0.85	…	…	…	…	…	No Obs
177	1.7855 ± 0.0225	−4.142 ± 0.041	3.931 ± 0.039	…	204.3 ± 2.6	479.8 ± 6.0	204.3 ± 2.6	…	…	…	…	…	No Obs
178	4.4875 ± 0.2181	22.593 ± 0.471	24.558 ± 0.447	…	42.7 ± 2.2	213.1 ± 10.3	49.1 ± 2.5	…	…	…	…	…	No Obs, VB
179 △	4.5968 ± 0.0190	10.676 ± 0.036	8.783 ± 0.038	−9.74 ± 2.88	74.03 ± 0.31	192.24 ± 0.79	69.93 ± 0.29	9.3 ± 1.0	−13.3 ± 2.5	−6.0 ± 0.9	236 ± 31	0	
180	4.0183 ± 0.2705	24.296 ± 0.433	13.133 ± 0.443	…	63.6 ± 4.4	233 ± 16	60.1 ± 4.1	…	…	…	…	…	No Obs
181	1.4237 ± 0.0198	−4.132 ± 0.040	−3.404 ± 0.040	…	283.5 ± 3.9	593.8 ± 8.3	245.7 ± 3.4	…	…	…	…	…	No Obs
182	6.9380 ± 0.0210	19.547 ± 0.041	10.796 ± 0.038	−11.4 ± 0.5	59.15 ± 0.18	123.00 ± 0.37	46.35 ± 0.15	9.1 ± 0.2	−15.6 ± 0.4	−6.0 ± 0.2	441 ± 39	0.20	Cep III member
183	8.7931 ± 0.0268	22.613 ± 0.050	40.33 ± 0.044	…	36.53 ± 0.12	105.92 ± 0.32	19.509 ± 0.071	…	…	…	…	…	No Obs
184 c1	3.1496 ± 0.0250	10.564 ± 0.042	−3.011 ± 0.042	−7.5 ± 1.8	100.70 ± 0.80	298.9 ± 2.4	36.38 ± 0.31	12.1 ± 0.6	−7.2 ± 1.7	−11.5 ± 0.2	326 ± 21	0.47	SB1?, VB
184 c2	0.0992 ± 0.0397	−1.808 ± 0.063	−1.025 ± 0.063	−101.6 ± 2.0	3197 ± 1279	9490 ± 3798	1155 ± 462	−119 ± 30	−40 ± 9	−66 ± 25	54 ± 39	2.54	
185 c1	0.9852 ± 0.0233	−1.890 ± 0.042	2.795 ± 0.048	−16.4 ± 0.7	371.9 ± 8.8	925 ± 22	188.4 ± 4.5	−11.8 ± 0.4	−18.3 ± 0.7	7.6 ± 0.4	326 ± 29	1.22	
185 c2	1.9591 ± 0.0452	−13.348 ± 0.076	4.914 ± 0.077	−55.4 ± 0.8	187.1 ± 4.3	465 ± 11	94.7 ± 2.2	−47.5 ± 0.7	−44.6 ± 0.8	−2.0 ± 0.5	0 ± 98	0.55	
186	4.9378 ± 0.0247	15.025 ± 0.055	5.091 ± 0.043	−3.8 ± 0.7	85.22 ± 0.43	174.20 ± 0.87	58.35 ± 0.30	12.2 ± 0.3	−9.1 ± 0.6	−3.7 ± 0.2	349 ± 24	0.16	Cep III member
187	3.6518 ± 0.0259	−2.478 ± 0.046	3.446 ± 0.039	…	115.91 ± 0.82	237.3 ± 1.7	72.53 ± 0.52	…	…	…	…	…	No Obs
188	5.9488 ± 0.0245	20.620 ± 0.045	4.577 ± 0.043	−11.1 ± 0.7	73.19 ± 0.30	144.14 ± 0.59	46.10 ± 0.20	10.3 ± 0.3	−16.0 ± 0.6	−6.7 ± 0.2	255 ± 18	0.10	VB, Cep II member
189	3.1191 ± 0.9470	22.926 ± 1.637	4.261 ± 1.703	−5.6 ± 0.7	142 ± 43	272 ± 83	92 ± 28	29.0 ± 9.4	−18.4 ± 3.7	−10.4 ± 5.2	360 ± 31	0.41	
190	1.8118 ± 0.0299	13.866 ± 0.065	0.523 ± 0.068	…	242.1 ± 4.0	474.5 ± 7.8	144.64 ± 2.4	…	…	…	…	…	No Obs
191 c1	5.3870 ± 0.3028	16.134 ± 0.533	1.344 ± 0.628	−7.6 ± 0.8	79.3 ± 4.5	163.0 ± 9.2	40.1 ± 2.5	9.5 ± 0.9	−11.7 ± 0.8	−5.9 ± 0.6	551 ± 41	0.10	Cep III member
191 c2	4.9829 ± 0.0316	16.721 ± 0.054	−0.773 ± 0.055	−7.1 ± 1.3	85.74 ± 0.54	176.2 ± 1.1	43.36 ± 0.28	10.8 ± 0.6	−11.1 ± 1.1	−8.1 ± 0.3	540 ± 95	0.41	Cep III member
192	3.5560 ± 0.0303	17.308 ± 0.050	1.352 ± 0.040	−10.3 ± 0.8	126.1 ± 1.1	249.2 ± 2.1	32.85 ± 0.30	16.0 ± 0.4	−18.9 ± 0.7	−5.2 ± 0.1	313 ± 40	0.17	Multiple system
193	5.9923 ± 0.0252	21.618 ± 0.045	1.055 ± 0.045	−7.59 ± 0.22	79.93 ± 0.34	138.67 ± 0.58	47.25 ± 0.21	10.8 ± 0.1	−14.1 ± 0.2	−5.9 ± 0.1	301 ± 18	0	Cep II member
G1	6.3842 ± 0.0331	23.205 ± 0.046	0.753 ± 0.044	−8.40 ± 0.28	76.17 ± 0.40	128.94 ± 0.67	45.90 ± 0.25	10.3 ± 0.2	−15.1 ± 0.2	−5.8 ± 0.1	209 ± 14	0.08	VB, Cep II member
G2 ‡	5.7214 ± 0.0317	22.091 ± 0.053	−1.511 ± 0.055	…	86.60 ± 0.48	145.53 ± 0.81	43.24 ± 0.25	…	…	…	175 ± 10	…	VB, Cep III member
G3 c1	6.7087 ± 0.0416	20.413 ± 0.100	−1.844 ± 0.062	−9.2 ± 0.1	76.43 ± 0.47	121.03 ± 0.75	41.59 ± 0.27	6.6 ± 0.1	−15.3 ± 0.3	−4.11 ± 0.05	307 ± 12	0.08	Cep I member
G3 c2	6.7211 ± 0.0320	24.902 ± 0.059	−3.909 ± 0.051	−8.7 ± 0.7	76.29 ± 0.36	120.81 ± 0.58	41.51 ± 0.20	9.0 ± 0.4	−16.4 ± 0.6	−6.4 ± 0.2	453 ± 90	0.29	Cep I member
G4 *	6.7016 ± 0.0218	23.419 ± 0.059	−3.861 ± 0.035	−9.54 ± 0.41	76.67 ± 0.25	121.03 ± 0.39	41.71 ± 0.14	7.7 ± 0.2	−16.7 ± 0.3	−5.9 ± 0.1	216 ± 17	…	SB2, VB, Cep I member
F1 ‡	4.7892 ± 0.3432	11.015 ± 0.588	10.377 ± 0.665	−10.01 ± 1.96	52.7 ± 3.9	195 ± 14	52.2 ± 3.8	10.2 ± 1.1	−14.2 ± 1.9	−4.4 ± 1.1	205 ± 62	0	VB
F2 ‡	5.4139 ± 0.1187	17.066 ± 0.211	7.164 ± 0.191	−7.45 ± 1.80	75.2 ± 1.7	159.7 ± 3.5	54.3 ± 1.2	11.7 ± 0.8	−12.5 ± 1.6	−4.9 ± 0.6	245 ± 50	0.12	Cep III member
F3 ‡	5.2788 ± 0.0307	18.273 ± 0.050	−0.341 ± 0.050	−5.69 ± 1.00	83.35 ± 0.49	165.13 ± 0.96	40.86 ± 0.25	11.7 ± 0.4	−10.7 ± 0.9	−7.1 ± 0.2	365 ± 44	0.30	Multi. syst., Cep III member
F4 ‡	4.7005 ± 0.6512	18.328 ± 1.128	0.835 ± 0.968	−9.05 ± 0.72	102 ± 14	178 ± 25	55.7 ± 8.0	11.4 ± 2.5	−16.0 ± 1.4	−6.2 ± 1.1	330 ± 76	0.30	Cep III member

Note.
⋆ If we put two sources on the slit during one IDS observation, the brightest and faintest sources are "c1" and "c2", respectively.
† Astrometry from the URAT Parallax Catalog (UPC – Zacharias et al. 2015; Finch & Zacharias 2016).
‡ Radial velocity and lithium equivalent width from Paper III.
* Lithium equivalent width from Paper III. Radial velocity near the conjunction reported in Paper III (i.e., at HJD = 2455077.6191).
△ We used the *RV* measurement quoted in *Gaia* DR2 to compute the space-velocity components.

Table 5. Comoving companions of our targets whose names are in bold. We reported the astrometry, G magnitude and radial velocity RV_{Gaia} released in the *Gaia* DR2 catalog. We derived their angular separation (ρ), position angle (θ), and projected physical separation (s) with regard to the brightest star, along with the associated errors.

#	*Gaia* DR2 name	π [mas]	$\mu_\alpha \cos\delta$ [mas yr^{-1}]	μ_δ [mas yr^{-1}]	Gmag [mag]	RV$_{Gaia}$ [km s^{-1}]	ρ [$''$ ± mas]	θ [$^\circ$ ± $''$]	s [AU]
3	*Gaia* DR2 3941779422146835 20	33.8287 ± 0.0602	208.768 ± 0.097	−35.025 ± 0.068	11.8573 ± 0.0010	−12.39 ± 0.56	…	…	…
	Gaia DR2 3941779465102772 48	33.7578 ± 0.1084	209.999 ± 0.175	−29.251 ± 0.105	14.3724 ± 0.0009	…	2.27 ± 0.125	300.89 ± 47.17	67.2 ± 0.1
6	*Gaia* DR2 5647079737331328 00	6.4739 ± 0.1404	24.376 ± 0.307	−3.003 ± 0.209	11.6041 ± 0.0081	…	…	…	…
	Gaia DR2 5647079737331320 32	6.7211 ± 0.0321	23.318 ± 0.061	−2.834 ± 0.046	12.9056 ± 0.0009	−8.34 ± 2.37	12.01 ± 0.127	322.07 ± 3.02	1856 ± 9
	Gaia DR2 5648020506959787 52	6.9090 ± 0.0928	23.770 ± 0.156	−3.458 ± 0.135	17.1583 ± 0.0013	…	205.48 ± 0.185	358.53 ± 0.05	31740 ± 160
18	**Gaia DR2 5759217210245089 28**	6.9947 ± 0.0256	47.790 ± 0.048	−54.249 ± 0.042	12.6970 ± 0.0012	…	…	…	…
	Gaia DR2 5759217210245093 12	7.0859 ± 0.0239	47.536 ± 0.048	−54.317 ± 0.039	14.2886 ± 0.0005	…	5.84 ± 0.031	224.01 ± 2.03	835.1 ± 3.1
25	**Gaia DR2 4880389592106170 88**	9.2418 ± 0.0296	−55.973 ± 0.044	−47.168 ± 0.044	11.9592 ± 0.0005	−24.49 ± 0.67	…	…	…
	Gaia DR2 4880389592059882 24	9.2593 ± 0.0346	−55.936 ± 0.052	−52.590 ± 0.051	12.4361 ± 0.0018	−42.59 ± 7.78	1.58 ± 0.045	303.83 ± 21.77	170.8 ± 0.5
38	*Gaia* DR2 4799040162691406 08	19.1742 ± 0.0778	47.633 ± 0.085	−118.803 ± 0.113	11.4949 ± 0.0017	16.71 ± 0.6	…	…	…
	Gaia DR2 4799040162713047 04	18.6521 ± 0.1506	51.896 ± 0.184	−120.795 ± 0.266	11.6018 ± 0.0050	…	1.16 ± 0.077	275.43 ± 372.2	60.6 ± 0.2
40	**Gaia DR2 1116789731452567936**	7.4974 ± 0.0222	−2.118 ± 0.032	19.196 ± 0.040	12.3937 ± 0.0003	−12.18 ± 0.62	…	…	…
	Gaia DR2 1116789735748819968	7.4445 ± 0.0401	−2.593 ± 0.053	16.775 ± 0.078	13.8940 ± 0.0007	…	2.52 ± 0.032	115.13 ± 24.35	336 ± 1
43	**Gaia DR2 1152331242957967104**	5.7831 ± 0.0218	4.642 ± 0.032	−22.886 ± 0.041	10.7027 ± 0.0012	−60.88 ± 14.28	…	…	…
	Gaia DR2 1152331238662558464	5.9419 ± 0.0331	6.956 ± 0.054	−22.798 ± 0.062	12.2297 ± 0.0002	−24.09 ± 1.36	4.70 ± 0.013	102.13 ± 52.21	812 ± 3
47	**Gaia DR2 1138420290562688640**	7.9920 ± 0.0264	−7.424 ± 0.037	−89.250 ± 0.049	10.7933 ± 0.0085	…	…	…	…
	Gaia DR2 1138420256203049344	5.6153 ± 0.5873	−6.225 ± 0.929	−91.593 ± 1.173	15.5622 ± 0.0020	…	44.98 ± 0.573	211.14 ± 2.46	5630 ± 19
50	**Gaia DR2 1151984484476815360**	5.5026 ± 0.0186	−18.795 ± 0.036	−23.996 ± 0.038	10.5904 ± 0.0042	…	…	…	…
	Gaia DR2 1151984484477988096	5.5095 ± 0.0257	−20.891 ± 0.061	−22.002 ± 0.056	14.2201 ± 0.0024	…	2.52 ± 0.028	234.75 ± 9.59	458 ± 2
55	**Gaia DR2 1134776955703665280**	13.7809 ± 0.0560	−60.794 ± 0.078	−25.573 ± 0.06	10.5182 ± 0.0029	…	…	…	…
	Gaia DR2 1134776955704678656	13.6886 ± 0.1067	−56.688 ± 0.108	−28.878 ± 0.08	13.1162 ± 0.0016	−14.72 ± 4.62	3.77 ± 0.093	26.20 ± 3.86	273 ± 1
56	**Gaia DR2 1720278167490425472**	3.2342 ± 0.0213	−18.996 ± 0.039	19.453 ± 0.032	11.5351 ± 0.0103	−23.0 ± 18.23	…	…	…
	Gaia DR2 1720278167488409472	2.7156 ± 0.1770	−18.663 ± 0.341	19.584 ± 0.244	17.3547 ± 0.0061	…	2.78 ± 0.112	230.75 ± 23.71	859 ± 6
57	**Gaia DR2 1726350151734755200**	9.2549 ± 0.0876	−51.835 ± 0.184	−5.563 ± 0.142	12.6675 ± 0.0013	−27.80 ± 6.27	…	…	…
	Gaia DR2 1726350147444401280	9.5762 ± 0.0199	−45.295 ± 0.044	−4.474 ± 0.032	12.8263 ± 0.0040	−19.96 ± 3.41	1.77 ± 0.078	220.33 ± 13.86	191 ± 2
66	**Gaia DR2 1698467189688877568**	6.6284 ± 0.0305	−38.712 ± 0.052	22.158 ± 0.048	10.9682 ± 0.0013	−8.01 ± 0.74	…	…	…
	Gaia DR2 1698467185393807872	6.6712 ± 0.0818	−36.373 ± 0.156	28.191 ± 0.137	14.4617 ± 0.0010	…	5.37 ± 0.098	34.04 ± 4.566	810 ± 4
69	**Gaia DR2 1703801775293097472**	20.2010 ± 0.9409	−28.939 ± 1.691	−63.378 ± 1.797	12.7115 ± 0.0014	−3.55 ± 11.63	…	…	…
	Gaia DR2 1703801779587789568	16.7651 ± 0.0512	−24.593 ± 0.120	−56.745 ± 0.094	13.2566 ± 0.0015	…	0.93 ± 0.904	142.97 ± 267.5	46 ± 2
81	**Gaia DR2 1723454381704388992**	18.4582 ± 0.0300	22.243 ± 0.057	−8.491 ± 0.054	13.0280 ± 0.0008	−5.87 ± 1.68	…	…	…
	Gaia DR2 1723454381704389248	18.4850 ± 0.0246	23.474 ± 0.048	−13.04 ± 0.045	13.4170 ± 0.0006	…	2.78 ± 0.030	121.52 ± 12.19	150.9 ± 0.2
91	**Gaia DR2 2253412973338518784**	2.9807 ± 0.0777	−17.761 ± 0.147	−6.453 ± 0.196	10.8272 ± 0.0020	−35.88 ± 8.43	…	…	…
	Gaia DR2 2253412969042676736	2.9785 ± 0.1922	−18.378 ± 0.325	−6.364 ± 0.421	18.5588 ± 0.0031	…	18.40 ± 0.269	304.35 ± 11.71	6174 ± 161
100	**Gaia DR2 2260807635712585600**	7.2575 ± 0.7471	20.703 ± 1.708	55.176 ± 1.547	9.0816 ± 0.0002	−15.97 ± 0.80	…	…	…
	Gaia DR2 2260807635712585472	7.2367 ± 0.0559	21.517 ± 0.124	49.504 ± 0.092	11.2562 ± 0.0006	−17.18 ± 0.37	8.45 ± 0.820	9.85 ± 11.67	1164 ± 120
102	**Gaia DR2 2260953836398942336**	3.9580 ± 0.0213	6.072 ± 0.042	12.173 ± 0.04	12.0336 ± 0.0007	…	…	…	…
	Gaia DR2 2260953836398942464	3.9283 ± 0.0160	5.779 ± 0.031	11.954 ± 0.03	14.0640 ± 0.0028	…	4.10 ± 0.039	39.65 ± 2.97	1036 ± 6
109	**Gaia DR2 2248238121865016576**	2.4886 ± 0.0235	6.109 ± 0.047	10.938 ± 0.053	11.0831 ± 0.0041	…	…	…	…
	Gaia DR2 2248237980127605248	1.3161 ± 0.7362	5.041 ± 1.383	10.004 ± 1.785	20.1520 ± 0.0060	…	73.40 ± 0.777	228.14 ± 5.19	29496 ± 279
119	**Gaia DR2 2187341189325433472**	3.6599 ± 0.0173	7.367 ± 0.033	−7.720 ± 0.035	12.8377 ± 0.0018	…	…	…	…
	Gaia DR2 2187341185028860160	3.7446 ± 0.3248	7.536 ± 0.635	−8.336 ± 0.618	18.9285 ± 0.0033	…	16.67 ± 0.261	108.59 ± 44.52	4555 ± 22
120	**Gaia DR2 2245078881361655424**	5.7303 ± 0.0288	17.652 ± 0.067	−4.347 ± 0.060	9.8023 ± 0.0007	…	…	…	…
	Gaia DR2 2245078881361655296	5.7351 ± 0.0283	16.396 ± 0.065	−2.411 ± 0.069	11.3453 ± 0.0012	−22.06 ± 1.26	3.29 ± 0.050	288.51 ± 49.46	574 ± 3

Table 5. Continued.

#	*Gaia* DR2 name	π [mas]	$\mu_\alpha \cos\delta$ [mas yr^{-1}]	μ_δ [mas yr^{-1}]	Gmag [mag]	RV$_{Gaia}$ [km s^{-1}]	ρ [$''$ ± mas]	θ [$^\circ$ ± $''$]	s [AU]
123	*Gaia* DR2 2170325177440567168	3.4592 ± 0.0458	6.629 ± 0.093	6.635 ± 0.089	7.8058 ± 0.0004	…	…	…	…
	Gaia DR2 2170325181728860416	3.4235 ± 0.0432	8.333 ± 0.089	4.261 ± 0.108	9.2669 ± 0.0002	…	1.89 ± 0.063	264.15 ± 1157.8	545 ± 7
	***Gaia* DR2 2170324941214308992**	3.4269 ± 0.0251	8.190 ± 0.050	5.784 ± 0.050	11.3293 ± 0.0012	−21.86 ± 1.54	94.03 ± 0.063	110.92 ± 1.38	27180 ± 360
124	*Gaia* DR2 2270675683853260672	4.1241 ± 0.0298	9.217 ± 0.049	6.193 ± 0.047	9.4318 ± 0.0003	…	…	…	…
	***Gaia* DR2 2270675683853258880**	4.1805 ± 0.0346	9.568 ± 0.057	6.836 ± 0.057	13.5652 ± 0.0010	−13.47 ± 16.34	23.96 ± 0.030	259.64 ± 16.87	5810 ± 42
125	***Gaia* DR2 2192552221605362048**	3.4229 ± 0.0223	6.410 ± 0.041	6.161 ± 0.042	11.7654 ± 0.0011	−24.71 ± 2.53	…	…	…
	Gaia DR2 2192552221600855168	4.2636 ± 0.2240	5.895 ± 0.407	6.299 ± 0.615	16.0953 ± 0.0080	…	1.39 ± 0.189	75.71 ± 875.0	406 ± 3
	Gaia DR2 2192364548713717632	1.8968 ± 1.2094	6.057 ± 2.366	7.104 ± 3.024	20.7648 ± 0.0136	…	44.55 ± 1.425	129.23 ± 17.82	13016 ± 85
131	***Gaia* DR2 2216911008366802304**	6.7559 ± 0.0739	30.093 ± 0.165	11.946 ± 0.136	11.2458 ± 0.0014	…	…	…	…
	Gaia DR2 2216910630409680000	6.9383 ± 0.0608	33.032 ± 0.146	11.696 ± 0.127	15.1823 ± 0.0009	…	6.74 ± 0.137	224.17 ± 8.08	998 ± 11
135	***Gaia* DR2 2202658309713224064**	2.4955 ± 0.0229	11.907 ± 0.046	26.296 ± 0.049	11.8941 ± 0.0020	−76.97 ± 17.84	…	…	…
	Gaia DR2 2202656763526368896	2.6578 ± 0.1110	11.862 ± 0.215	26.498 ± 0.212	17.7468 ± 0.0012	…	58.26 ± 0.144	191.86 ± 0.32	23350 ± 214
140	***Gaia* DR2 2005807146670436608**	4.6715 ± 0.0166	15.432 ± 0.028	2.258 ± 0.029	13.1907 ± 0.0010	−19.68 ± 1.90	…	…	…
	Gaia DR2 2005807868208768000	4.1101 ± 1.7711	15.398 ± 3.165	11.763 ± 3.721	20.7617 ± 0.0147	…	27.63 ± 1.664	303.56 ± 46.66	5914 ± 21
144	***Gaia* DR2 2225093917495923968**	8.7382 ± 0.0309	−4.442 ± 0.048	−6.498 ± 0.042	10.6755 ± 0.0009	16.78 ± 12.30	…	…	…
	Gaia DR2 2225093780056968448	8.7790 ± 0.1087	−4.265 ± 0.170	−6.110 ± 0.140	16.6411 ± 0.0022	…	87.47 ± 0.095	233.31 ± 0.71	10010 ± 35
146	***Gaia* DR2 2211369980859065344**	20.4651 ± 0.0262	144.623 ± 0.042	−38.632 ± 0.042	12.0832 ± 0.0008	8.56 ± 10.75	…	…	…
	Gaia DR2 2211369882080370304	20.5554 ± 0.0594	144.773 ± 0.091	−38.223 ± 0.090	15.4719 ± 0.0005	…	50.66 ± 0.056	112.39 ± 2.29	2475 ± 3
149	***Gaia* DR2 2014273111312397312**	2.2842 ± 0.0251	5.193 ± 0.048	−0.221 ± 0.041	11.2336 ± 0.0010	−8.75 ± 3.61	…	…	…
	Gaia DR2 2014273111308595072	2.4920 ± 0.0913	4.900 ± 0.172	−1.325 ± 0.113	15.0804 ± 0.0054	…	1.68 ± 0.082	181.91 ± 2.42	734 ± 8
	Gaia DR2 2014278952464130688	2.3238 ± 0.1147	6.028 ± 0.247	−1.345 ± 0.310	16.6528 ± 0.0030	…	95.17 ± 0.067	92.99 ± 137.6	41667 ± 458
	Gaia DR2 2014278982529501696	2.1865 ± 0.4348	5.814 ± 0.778	−1.442 ± 0.654	19.7632 ± 0.0047	…	56.18 ± 0.358	51.68 ± 3.67	24600 ± 270
152	***Gaia* DR2 2282683892719472640**	7.0082 ± 0.0198	22.582 ± 0.037	4.888 ± 0.037	12.2306 ± 0.0030	…	…	…	…
	Gaia DR2 2282683897015937920	7.0380 ± 0.0670	23.568 ± 0.138	6.382 ± 0.129	14.7476 ± 0.0024	…	1.56 ± 0.056	297.25 ± 55.59	222.6 ± 0.6
157	*Gaia* DR2 2232420856825041920	7.7011 ± 0.0639	10.553 ± 0.082	−1.275 ± 0.070	10.2980 ± 0.0007	−11.77 ± 0.71	…	…	…
	***Gaia* DR2 2232420856822289408**	7.8348 ± 0.0488	8.660 ± 0.064	−1.105 ± 0.073	10.6758 ± 0.0007	−11.72 ± 0.49	17.64 ± 0.050	247.11 ± 6.50	2291 ± 19
160	***Gaia* DR2 2279559531646356608**	2.8245 ± 0.0701	6.988 ± 0.123	0.194 ± 0.112	15.0669 ± 0.0059	…	…	…	…
	Gaia DR2 2279559531646356352	2.8066 ± 0.0903	6.948 ± 0.158	0.858 ± 0.140	16.4999 ± 0.0012	…	5.36 ± 0.089	245.82 ± 32.96	1899 ± 47
170	***Gaia* DR2 517737008795018624**	3.8271 ± 0.0294	35.034 ± 0.033	−24.659 ± 0.041	12.0255 ± 0.0018	13.20 ± 8.43	…	…	…
	Gaia DR2 517736940075550336	3.8645 ± 0.0553	34.923 ± 0.061	−24.626 ± 0.073	16.0898 ± 0.0006	…	65.27 ± 0.058	181.03 ± 0.070	17055 ± 131
175	***Gaia* DR2 2274551496699656064**	7.0641 ± 0.0212	13.429 ± 0.040	18.865 ± 0.038	11.7748 ± 0.0022	−18.98 ± 0.63	…	…	…
	Gaia DR2 2274551496699655808	7.1643 ± 0.0866	14.315 ± 0.152	18.704 ± 0.170	16.8503 ± 0.0016	…	6.41 ± 0.075	295.38 ± 19.76	907 ± 3
178	***Gaia* DR2 2197589634127618304**	4.4875 ± 0.2181	22.593 ± 0.471	24.558 ± 0.447	10.2647 ± 0.0005	…	…	…	…
	Gaia DR2 2197589531048403712	3.9381 ± 0.1092	22.499 ± 0.218	24.416 ± 0.220	18.1145 ± 0.0014	…	59.43 ± 0.353	184.23 ± 0.55	13244 ± 644
184	***Gaia* DR2 2206637343514771328**	3.1496 ± 0.0250	10.564 ± 0.042	−3.011 ± 0.042	12.5093 ± 0.0017	−1.55 ± 3.31	…	…	…
	Gaia DR2 2206637343514769152	3.0842 ± 0.0842	10.685 ± 0.144	−3.222 ± 0.138	17.1744 ± 0.0031	…	8.82 ± 0.050	262.85 ± 157.9	2800 ± 22
188	***Gaia* DR2 2281573729572210432**	5.9488 ± 0.0245	20.620 ± 0.045	4.577 ± 0.043	10.8089 ± 0.0028	−8.84 ± 1.36	…	…	…
	Gaia DR2 2281573733870090240	5.5481 ± 0.2645	21.096 ± 0.446	5.664 ± 0.269	14.6213 ± 0.0085	…	1.39 ± 0.205	9.84 ± 15.41	234 ± 1
191	***Gaia* DR2 2231866561228307840**	5.3870 ± 0.3028	16.134 ± 0.533	1.344 ± 0.628	12.1211 ± 0.0014	−11.41 ± 2.83	…	…	…
	Gaia DR2 2231866565525667712	4.9829 ± 0.0316	16.721 ± 0.054	−0.773 ± 0.055	13.9459 ± 0.0038	…	3.80 ± 0.350	210.74 ± 18.68	706 ± 40
192	***Gaia* DR2 2214142433789105920**	3.5560 ± 0.0303	17.308 ± 0.050	1.352 ± 0.040	12.3241 ± 0.0013	−16.46 ± 4.41	…	…	…
	Gaia DR2 2214142884764242432	3.6330 ± 0.0946	16.939 ± 0.157	1.472 ± 0.118	16.9661 ± 0.0009	…	70.52 ± 0.050	277.48 ± 15.93	19830 ± 170
	Gaia DR2 2214143194002143488	3.9328 ± 0.2903	18.200 ± 0.477	2.197 ± 0.403	18.6291 ± 0.0030	…	9.09 ± 0.258	320.64 ± 8.99	2557 ± 22

Table 5. Continued.

#	*Gaia* DR2 name	π [mas]	$\mu_\alpha \cos\delta$ [mas yr^{-1}]	μ_δ [mas yr^{-1}]	Gmag [mag]	RV$_{Gaia}$ [km s^{-1}]	ρ [$''$ ± mas]	θ [$^\circ$ ± $''$]	s [AU]
G1	***Gaia* DR2 5646381504465472 00**	6.3842 ± 0.0331	23.205 ± 0.046	0.753 ± 0.044	10.0725 ± 0.0015	−6.89 ± 1.59	…	…	…
	Gaia DR2 5646381203841534 72	6.3519 ± 0.0500	22.692 ± 0.081	0.081 ± 0.071	15.0214 ± 0.0008	…	20.27 ± 0.023	259.71 ± 20.90	3175 ± 16
G2	***Gaia* DR2 5402160429845248 00**	5.7214 ± 0.0317	22.091 ± 0.053	−1.511 ± 0.055	9.5837 ± 0.0013	−6.68 ± 2.03	…	…	…
	Gaia DR2 5402160429867143 68	5.5658 ± 0.0688	21.230 ± 0.211	−3.130 ± 0.239	11.3110 ± 0.0077	…	1.39 ± 0.110	227.82 ± 38.68	243 ± 1
G3	***Gaia* DR2 5646984517886133 76**	6.7087 ± 0.0416	20.413 ± 0.100	−1.844 ± 0.062	10.2465 ± 0.0019	…	…	…	…
	Gaia DR2 5646984517893591 04	6.7211 ± 0.0320	24.902 ± 0.059	−3.909 ± 0.051	13.0051 ± 0.0033	−17.46 ± 18.82	8.53 ± 0.023	261.12 ± 62.21	1272 ± 8
G4	***Gaia* DR2 5646958791052879 36**	6.7016 ± 0.0218	23.419 ± 0.059	−3.861 ± 0.035	9.4249 ± 0.0009	…	…	…	…
	Gaia DR2 5646958791052893 44	6.6812 ± 0.0656	24.390 ± 0.142	−2.793 ± 0.104	16.0252 ± 0.0008	…	15.32 ± 0.074	195.30 ± 0.513	2286 ± 7
F1	***Gaia* DR2 2270685442018922 112**	4.7892 ± 0.3432	11.015 ± 0.588	10.377 ± 0.665	10.0239 ± 0.0010	−10.35 ± 1.63	…	…	…
	Gaia DR2 2270685442018921 984	5.3159 ± 0.0465	11.187 ± 0.099	8.137 ± 0.086	15.9652 ± 0.0018	…	12.67 ± 0.407	26.44 ± 5.79	2645 ± 190
F3	***Gaia* DR2 2231801002846066 304**	5.2788 ± 0.0307	18.273 ± 0.050	−0.341 ± 0.050	9.8850 ± 0.0019	…	…	…	…
	Gaia DR2 2231801007144857 856	5.2670 ± 0.0665	17.705 ± 0.118	−0.675 ± 0.113	14.2899 ± 0.0007	…	9.25 ± 0.094	155.79 ± 1.537	1751 ± 10
	Gaia DR2 2231794547514058 624	5.1245 ± 0.1204	18.268 ± 0.204	−0.226 ± 0.207	17.6214 ± 0.0022	…	384.01 ± 0.036	89.15 ± 342.3	72746 ± 423